

# Sympathetic cooling of a membrane oscillator in a hybrid mechanical-atomic system

Inauguraldissertation

zur  
Erlangung der Würde eines Doktors der Philosophie  
vorgelegt der  
Philosophisch-Naturwissenschaftlichen Fakultät  
der Universität Basel

von

**Andreas Jöckel**  
aus Deutschland



Basel, 2014

The original document is saved on the university of Basel document server  
<http://edoc.unibas.ch>



This work is licensed under a Creative Commons  
Attribution-NonCommercial-NoDerivatives 4.0 International License.

The complete text may be reviewed here:  
<http://creativecommons.org/licenses/by-nc-nd/4.0/>

Genehmigt von der Philosophisch-Naturwissenschaftlichen Fakultät  
auf Antrag von  
Prof. Dr. Philipp Treutlein  
Prof. Dr. Lukas Novotny

Basel, den 14. Oktober 2014

Prof. Dr. Jörg Schibler  
Dekan



## Creative Commons License Deed

---

Attribution-NonCommercial-NoDerivatives 4.0 International

This is a human-readable summary of (and not a substitute for) the license.

You are free to:



Share — copy and redistribute the material in any medium or format

The licensor cannot revoke these freedoms as long as you follow the license terms.

Under the following terms:



Attribution — You must give appropriate credit, provide a link to the license, and indicate if changes were made. You may do so in any reasonable manner, but not in any way that suggests the licensor endorses you or your use.



NonCommercial — You may not use the material for commercial purposes.



NoDerivatives — If you remix, transform, or build upon the material, you may not distribute the modified material.

No additional restrictions — You may not apply legal terms or technological measures that legally restrict others from doing anything the license permits.

Notices:

You do not have to comply with the license for elements of the material in the public domain or where your use is permitted by an applicable exception or limitation.

No warranties are given. The license may not give you all of the permissions necessary for your intended use. For example, other rights such as publicity, privacy, or moral rights may limit how you use the material.



# Abstract

The quantum behaviour of macroscopic mechanical oscillators is currently being investigated using a variety of mechanical systems and techniques such as optomechanical cooling and cold damping. As mechanical systems are also very versatile transducers between different physical systems, it is possible to build hybrid systems that combine the advantages of their constituents. This opens up new possibilities for fundamental studies of quantum physics, precision sensing and quantum information processing. Ultra-cold atoms represent one of the best-controlled systems available, thus making a well-developed toolbox for quantum manipulation available to mechanical oscillators in a hybrid system.

In this thesis, I report on the realization of a hybrid mechanical-atomic system consisting of a  $\text{Si}_3\text{N}_4$  membrane inside an optical cavity coupled to an ensemble of atoms. The coupling is mediated by a light field that couples the atomic motion to the membrane motion over a large distance. By laser cooling the atomic motion, the membrane is sympathetically cooled via its interaction with the atoms to a temperature of 0.7 K starting from room temperature, despite the enormous mass ratio of  $10^{10}$  between the membrane and the atomic ensemble. Up to now, sympathetic cooling had only been used to cool microscopic particles with much lower masses. The system reported in this thesis is the first hybrid system where the back-action of the atoms onto the mechanical oscillator is sufficiently large for practical applications. It represents a significant improvement over a previous experiment in our laboratory, where the atom's influence onto the mechanical oscillator was barely detectable. An atom-membrane cooperativity  $C > 1$  is achieved, thus enabling the study of effects such as a mechanical analog of electromagnetically induced transparency in the system, which will be investigated in the future. The quantitative analysis of the coupling mechanism also allows to predict experimental requirements for future ground state cooling of the mechanical oscillator, which are within reach. Interestingly, hybrid systems such as ours can provide ground-state cooling of low-frequency mechanical oscillators in a regime, where neither cavity optomechanical cooling nor cold damping can reach the ground state.

---

# Contents

<b>Abstract</b>	<b>i</b>
<b>Introduction</b>	<b>1</b>
<b>1 Theory of the mechanical-atomic hybrid quantum system</b>	<b>5</b>
1.1 Driven harmonic oscillator . . . . .	6
1.1.1 Steady state spectral analysis . . . . .	7
1.1.2 Time domain evolution . . . . .	8
1.2 Optomechanical system: membrane inside a cavity . . . . .	11
1.2.1 Cavity field . . . . .	12
1.2.2 Cavity finesse . . . . .	14
1.2.3 Optomechanical damping and optical spring effect . . . . .	16
1.2.4 Impact of laser noise . . . . .	18
1.2.5 Quantum limits . . . . .	19
1.2.6 Membrane motion readout . . . . .	20
1.3 Trapping ultracold atoms . . . . .	20
1.3.1 Dipole force: Dipole trap . . . . .	21
1.3.2 Scattering force: Magneto-optical trapping . . . . .	22
1.4 Atom-membrane coupling mechanism . . . . .	23
1.4.1 Classical description . . . . .	24
1.4.2 Ensemble-integrated sympathetic cooling rate . . . . .	26
1.4.3 Modifications in fully quantized calculation and coherent dynamics . . . . .	27
<b>2 SiN Membrane oscillators</b>	<b>31</b>
2.1 Basic properties . . . . .	31
2.2 Quality factor analysis . . . . .	34
2.2.1 Frequency tuning . . . . .	34
2.2.2 Mechanical dissipation mechanisms . . . . .	37
2.2.3 Further Q factor dependencies . . . . .	38
2.3 High-stress membranes . . . . .	41
2.4 Improving membrane properties . . . . .	42
2.4.1 Conclusions for mounting . . . . .	42

2.4.2	Structuring membranes . . . . .	42
<b>3</b>	<b>Ultra-cold atom apparatus</b>	<b>47</b>
3.1	Design considerations . . . . .	47
3.2	Vacuum system . . . . .	49
3.2.1	3D-MOT chamber . . . . .	49
3.2.2	2D-MOT . . . . .	53
3.2.3	Assembly and baking . . . . .	55
3.3	Magnetic fields . . . . .	56
3.3.1	Coil parameters . . . . .	56
3.3.2	3D-MOT coil . . . . .	57
3.3.3	2D-MOT coil . . . . .	58
3.3.4	Compensation fields . . . . .	59
3.4	Laser system . . . . .	60
3.5	Imaging system . . . . .	63
3.6	Experiment control . . . . .	65
3.7	System performance . . . . .	66
3.7.1	2D-MOT performance . . . . .	66
3.7.2	3D-MOT performance . . . . .	67
3.7.3	Optical molasses . . . . .	71
3.7.4	Optical lattice . . . . .	73
3.7.5	Conclusion . . . . .	76
<b>4</b>	<b>Optomechanical system: Membrane in a Cavity</b>	<b>79</b>
4.1	Design of the cavity system . . . . .	79
4.1.1	Cavity parameters . . . . .	80
4.1.2	Mounting and alignment . . . . .	80
4.2	System characterisation . . . . .	82
4.2.1	Optical readout . . . . .	82
4.2.2	Optical properties . . . . .	84
4.2.3	Cavity stabilization . . . . .	86
4.2.4	Laser noise . . . . .	87
4.3	Optomechanical measurements . . . . .	93
4.3.1	Membrane Q . . . . .	93
4.3.2	Cavity cooling . . . . .	95
4.3.3	Effective membrane mass . . . . .	96
4.3.4	Optomechanical spring . . . . .	96
<b>5</b>	<b>Coupled atom-membrane system</b>	<b>99</b>
5.1	System preparation . . . . .	99
5.2	Cooling in the time domain . . . . .	100
5.3	Cooling in the frequency domain . . . . .	104
5.3.1	Membrane absorption estimate . . . . .	106
5.4	Ringdown measurements: Atom detuning dependency . . . . .	107

5.5	Conclusions . . . . .	109
<b>6</b>	<b>Conclusions and outlook</b>	<b>111</b>
6.1	Improved optomechanical cavity . . . . .	112
6.2	Transverse lattice . . . . .	113
6.3	Groundstate cooling estimate . . . . .	115
6.4	Coupling to internal states . . . . .	116
6.5	Opto-mechanically induced transparency . . . . .	116
<b>A</b>	<b>Experiment photographs</b>	<b>117</b>
<b>B</b>	<b>Acronyms</b>	<b>121</b>
<b>C</b>	<b>Variable definitions</b>	<b>123</b>
	<b>List of Figures</b>	<b>127</b>
	<b>List of Tables</b>	<b>129</b>
	<b>Bibliography</b>	<b>131</b>



# Introduction

Quantum mechanics is one of the best tested theories of the past century and has led to an enormous progress in metrology and fundamental physics, leading to complete control over the quantum state of microscopic objects. An open question is the transition from the microscopic quantum to macroscopic classical world. There is a lot of theoretical research connected to this question [1, 2] that predicts mechanisms of gravitational collapse of wavefunctions and other fundamental decoherence mechanisms that have not yet been observed. Since the first experiments on radiation pressure inside optical cavities [3] people have tried cooling single motional modes of mesoscopic and macroscopic objects into the quantum ground state using radiation pressure forces to explore quantum phenomena in these systems. In the past years, a research community has developed around the field of quantum mechanics of mechanical objects [4], which involves a variety of different objects including cantilevers with mirrors [5], levitated particles [6, 7, 8], toroidal resonators [9], membranes inside cavities [10, 11, 12], photonic crystal nano beams [13], clouds of cold atoms [14, 15, 16], piezoelectric mechanical oscillators [17] and nano beams [18]. The masses range from zg to kg in gravitational wave detectors [19], and techniques of optomechanical cooling, cold damping and cryogenic cooling are utilized. First experiments have reached the quantum groundstate [17, 20, 13, 9] and could even show state swapping [17, 21, 9]. These system all use oscillators with frequencies of 10 MHz to GHz. The cooling of larger oscillators with lower frequency into the ground state has not yet been achieved.

Another aspect of mechanical systems is their ability to act as universal transducers between different physical systems. The ability to connect different types of quantum systems has brought up the field of hybrid quantum systems [22, 23], in which one tries to combine the advantages of different systems, mostly in the context of quantum information processing. Examples of such systems are the coupling of mechanical oscillators to solid state spin systems [24, 25, 26, 27], semiconductor quantum dots [28, 29], superconducting devices [17, 30] and atoms [14, 15] A practical application is the transformation of microwaves into optical light using a mechanical oscillator, which has been achieved recently [31, 32].

In this thesis a hybrid system has been built, where the motion of ultracold atoms is coupled to the motion of a micromechanical membrane inside a cavity. Atomic systems represent, together with trapped ions, on of the best controlled quantum system available today, with full control over all external and internal degrees of

---

freedom [33]. Such a hybrid atom-mechanical system allows to use this toolbox of quantum mechanics in the mechanical system. For these reasons a number of proposals have been published in the past years, which all present different ways to couple these two systems [34, 35, 36, 37, 38, 39, 40, 41, 42, 43, 44, 45, 46, 47, 48, 49].

In first experiments conducted by our group, the interaction of a cantilever with a Bose-Einstein condensate of rubidium atoms had been measured [14], but the back-action of the atoms onto the cantilever could not be observed. In a succeeding experiment this back-action onto silicon nitride membrane oscillator could be detected [15, 46]. There, the systems were coupled over a large distance using a light field, that is reflected of the membrane, thus creating a standing wave potential, in which the atoms were oscillating. The coupling is mediated by the influence of the membrane and atomic system onto the light field, allowing for an energy exchange between the systems. The atomic system can therefore be used to extract energy from the membrane by applying a damping force onto the atoms, which could be detected. This was possible, as the SiN membranes have exceptional mechanical properties with quality factors up to  $10^7$ , which makes them a popular choice for optomechanical systems [10, 11]. Using the coupling, we were able to increase the energy decay rate of the oscillator on the percent level, but not large enough for any practical application.

In the experiment presented in this thesis, the coupling is enhanced by the integration of the membrane into an optical cavity, thereby increasing the coupling by orders of magnitude. In addition, a new experimental apparatus for trapping ultracold rubidium atoms has been built to overcome previous limitations. The new setup and coupling scheme is thus enabling us to cool the membrane sympathetically along the atoms from room temperature to a few hundred mK. In the context of sympathetic cooling, this system does not rely on short range collisional interaction, but the collectively enhanced distant interaction of the two systems. This way, sympathetic cooling is possible despite the large mass ratio of  $10^{10}$  between the membrane and atomic ensemble. Sympathetic cooling has so far only been used to cool trapped ultracold atoms [50], ions [51] and molecules up to a mass ratio of 90 [52] to ultralow temperatures, where direct cooling was not available.

In this hybrid atom-membrane system, the cavity enhanced coupling scheme can be used to cool the mechanical oscillator into the ground state, as shown in theoretical analysis [45]. This scheme is especially useful for low frequency oscillators. It does not require the experimentally challenging resolved sideband condition  $\Omega_m \ll \kappa$  like optomechanical cooling, or a large optomechanical cooperativity like cold damping to reach the ground state [47].

Once there, the atomic system will allow to switch-off the damping, such that a coherent evolution of the system allows to transfer non-classical quantum states. These can be created in the atomic system and transferred to the mechanical system, thus enabling fundamental studies of decoherence or tasks of information processing.

A practical aspect of the system is its modularity, which allows a relatively easy exchange of parts of the system. In addition, as the system works in a regime of large atom-membrane cooperativity [47], but small optomechanical cooperativity,

losses of light are not crucial for reaching the groundstate.

### **This thesis**

This thesis is structured as follows: The **first chapter** will present the theoretical background of the hybrid system and its constituent parts. This contains on the optomechanical part the analysis of thermally driven harmonic oscillators, the field of the optical cavity and its interaction with the membrane motion, as well as the resulting optomechanical effects. On the atomic system part, the atom-light interaction that is used to trap and cool ultracold atoms will be presented. Finally, the coupling mechanism of the hybrid system will be derived in a classical description and the extensions of a fully quantized model will be discussed.

The **second chapter** focuses on the experimental analysis of the properties of silicon nitride (SiN) membranes, in particular their quality factor  $Q$  and its dependence on frequency and geometry, as well as optical absorption at the experiment wavelength.

The **third chapter** shows the design, construction and analysis of a new ultracold atom machine that is capable of producing large clouds of trapped rubidium atoms and flexible enough to be adaptable to other experiments. In this context, the trapping of atoms inside the lattice that couples the atom-membrane system will be discussed.

In **chapter four** the developed optomechanical system will be used to demonstrate cavity cooling of the membrane in order to characterize its properties. The cooling limitations due to laser noise will be shown and the conclusions for stabilization and control of the system will be discussed.

In the final **fifth chapter** the hybrid system is used to cool the motion of the membrane below 1 K starting from room temperature. The coupling will be analysed in time and frequency domain measurements. The cooling will be quantitatively analysed in dependence of atomic oscillation frequency and detuning to confirm the theoretical description of the system.

The **outlook** gives a perspective on improvements that are currently integrated and introduces possible future experiments that can be performed using the presented system. An estimate on the requirements for groundstate cooling is given.

---

## Contributions to publications

1. A. Jöckel, A. Faber, T. Kampschulte, M. Korppi, M. T. Rakher, and P. Treutlein. *Sympathetic cooling of a membrane oscillator in a hybrid mechanical-atomic system*. ArXiv:1407.6820, July 2014.
2. M. Korppi, A. Jöckel, M. T. Rakher, S. Camerer, D. Hunger, T. W. Hänsch, and P. Treutlein. *Hybrid atom-membrane optomechanics*. In European Physical Journal Web of Conferences, volume 57 of European Physical Journal Web of Conferences, page 3006, August 2013.
3. B. Vogell, K. Stannigel, P. Zoller, K. Hammerer, M. T. Rakher, M. Korppi, A. Jöckel, and P. Treutlein. *Cavity-enhanced long-distance coupling of an atomic ensemble to a micromechanical membrane*. Phys. Rev. A, 87(2):023816, February 2013.
4. S. Camerer, M. Korppi, A. Jöckel, D. Hunger, T. W. Hänsch, and P. Treutlein. *Realization of an Optomechanical Interface Between Ultracold Atoms and a Membrane*. Phys. Rev. Lett., 107(22):223001, November 2011.
5. A. Jöckel, M. T. Rakher, M. Korppi, S. Camerer, D. Hunger, M. Mader, and P. Treutlein. *Spectroscopy of mechanical dissipation in micro-mechanical membranes*. Applied Physics Letters, 99(14):143109, October 2011.
6. David Hunger, Stephan Camerer, Maria Korppi, Andreas Jöckel, Theodor W. Hänsch, and Philipp Treutlein. *Coupling ultracold atoms to mechanical oscillators*. C. R. Phys., 12:871, August 2011.

# Chapter 1

## Theory of the mechanical-atomic hybrid quantum system

The hybrid mechanical-atomic system described in this thesis consists of a membrane in a single-sided optical cavity, such that incident light is reflected on resonance and forms a standing wave in front of the cavity, in which ultracold atoms can be trapped. It is shown in figure 1.1. The two systems - membrane and atoms - couple via their influence on the light field. The membrane oscillation inside the cavity shifts the cavity resonance frequency, resulting in a phase shift of the reflected light. This periodically moves the standing wave pattern and therefore couples to the atomic motion. The other way around, the atomic oscillation requires a periodic redistribution of laser power from the incoming to outgoing laser beam and vice versa to provide the restoring force, thus modulating the radiation pressure onto the membrane. The light couples atomic and mechanical motion with the coupling constant

$$g_N = |r_m| \Omega_a \sqrt{\frac{Nm\Omega_a}{M\Omega_m} \frac{2\mathcal{F}}{\pi}} \quad (1.1)$$

with membrane amplitude reflectivity  $|r_m|$ , atomic oscillation frequency  $\Omega_a$ , membrane frequency  $\Omega_m$ , atomic mass  $m$ , atom number  $N$ , effective membrane mass  $M$  and cavity finesse  $\mathcal{F}$ . In this coupled system, a damping rate  $\Gamma_a$  applied to the atoms can sympathetically damp the membrane along with rate

$$\Gamma_{\text{sym}}[N, \Omega_a] = \frac{g_N^2 \eta^2 t^2 \Gamma_a}{(\Omega_a - \Omega_m)^2 + (\Gamma_a/2)^2} \quad (1.2)$$

under the assumption of  $\Gamma_a \gg g_N$ . Here, efficiency factors for cavity amplitude incoupling efficiency  $\eta$  and optical amplitude transmission between the systems  $t$  are introduced. This additional damping of the membrane will reduce the temperature of the mechanical mode to

$$T = T_{\text{bath}} \frac{\Gamma_m}{\Gamma_m + \Gamma_{\text{sym}}} \quad (1.3)$$

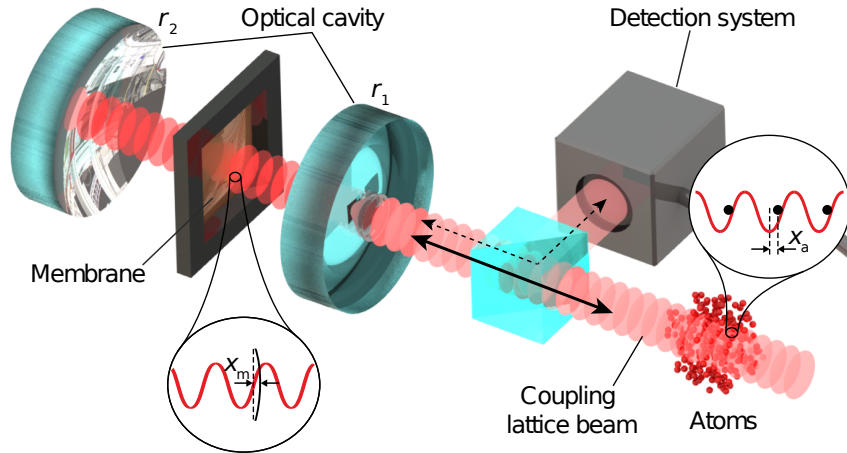


Figure 1.1: Sketch of experiment system: The motion of a membrane inside a cavity with amplitude reflectivities  $r_1$  and  $r_2 > r_1$  is coupled via a light field to the motion of an atomic ensemble, which oscillates inside the optical lattice, which is created by the coupling beam. Another light beam is used to detect the membrane motion. Drawing: Tobias Kampschulte

in a simple classical picture where  $T \gg \hbar\Omega_m/k_B$  and the quantum limits of the cooling are irrelevant. A fully quantized theory shows that the light mediated long-range interaction has the ability to cool the motional mode into the ground state, which then also enables coherent quantum dynamics between the two systems [45].

In the following, a theoretical description of the elementary parts of the system and the coupling will be given including additional effects that are present in the system. First, the behaviour of a thermally driven classical harmonic oscillator will be analysed, then follows a description of the optical cavity and the optomechanical interaction with a membrane placed inside the cavity. After that, the basics of trapping atoms will be given and finally the coupled hybrid system will be discussed in detail. At the end, the results of a fully quantum mechanical theory of the system will be discussed.

## 1.1 Driven harmonic oscillator

The optomechanics of a membrane inside a cavity is described in great detail in [53], here I will give a summary. The membrane mode of interest is treated as a driven damped harmonic oscillator with effective mass  $M$ , resonance frequency  $\Omega_m$  and intrinsic energy damping rate  $\Gamma_m$  related to the quality factor  $Q = \Omega_m/\Gamma_m$ :

$$M\ddot{x}_m(t) + M\Gamma_m\dot{x}_m(t) + M\Omega_m^2x_m(t) = F(t) \quad (1.4)$$

where  $x_m$  is the measured oscillator displacement out of equilibrium and  $F$  a force acting on the oscillator. The effective mass is calculated such that the potential en-

ergy of the oscillator is  $U(t) = M\Omega_m^2 x_m^2(t)/2$ . For an extended membrane with amplitude  $x(t, y, z) = x'_m \phi(y, z) \cos(\Omega_m t)$  (see equation 2.1 for mode function  $\phi(y, z)$ ), physical mass  $M_{\text{phys}}$  and probe intensity profile  $I(y, z)$  the oscillator's potential energy is

$$U(t) = \frac{M_{\text{phys}}\Omega_m^2}{2A} \int_A x(t, y, z)^2 dydz \equiv \frac{M\Omega_m^2 x_m^2(t)}{2} \quad (1.5)$$

$$\text{with } x_m(t) = \frac{\int_A x(t, y, z) I(y, z) dydz}{\int_A I(y, z) dydz} \quad (1.6)$$

being the mean mode displacement seen by the probe with integral over the membrane area  $A$ . The effective mass  $M$  then comes to

$$M = \int_A \frac{\phi(y, z)^2}{A} dydz \left( \frac{\int_A I(y, z) dydz}{\int_A \phi(y, z) I(y, z) dydz} \right)^2 M_{\text{phys}}. \quad (1.7)$$

For a point-like probe at the point of maximum amplitude the effective mass is  $M = M_{\text{phys}}/4$  for a square membrane and is increased when probing at points with lower amplitude.

### 1.1.1 Steady state spectral analysis

The oscillator's equation of motion 1.4 can be analysed by switching to frequency space using the Fourier transform  $x(\Omega) = \int_{-\infty}^{\infty} x(t) e^{-i\Omega t} dt$ , resulting in

$$-M\Omega^2 x_m(\Omega) + iM\Omega\Gamma_m x_m(\Omega) + M\Omega_m^2 x_m(\Omega) = F(\Omega) \quad (1.8)$$

where one can define the mechanical susceptibility

$$\chi(\Omega) \equiv \frac{x_m(\Omega)}{F(\Omega)} = \frac{1}{M(\Omega_m^2 - \Omega^2 + i\Omega\Gamma_m)}. \quad (1.9)$$

To describe the oscillator coupled to a thermal bath of temperature  $T_{\text{bath}}$ , the thermal force onto the oscillator can be described using the single-sided force power spectral density (PSD) given by the Fluctuation-Dissipation Theorem

$$S_{F,\text{th}} = \frac{4k_B T_{\text{bath}}}{\Omega} \text{Im} \left[ \frac{1}{\chi(\Omega)} \right] = 4k_B T_{\text{bath}} \Gamma_m M. \quad (1.10)$$

The resulting displacement PSD is obtained using the transfer function  $|\chi(\Omega)|^2$

$$S_x(\Omega) = |\chi(\Omega)|^2 S_{F,\text{th}} = \frac{4k_B T_{\text{bath}} \Gamma_m}{M} \frac{1}{(\Omega_m^2 - \Omega^2)^2 + \Omega^2 \Gamma_m^2} \quad (1.11)$$

with  $\langle x_m^2 \rangle = \int_0^\infty S_x d\Omega / 2\pi$ . It can be simplified for  $\Gamma_m \ll \Omega_m$  using  $\Omega \approx \Omega_m$  to a Lorentzian

$$S_x(\Omega) \approx \frac{k_B T_{\text{bath}}}{M\Omega_m^2} \frac{\Gamma_m}{(\Omega_m - \Omega)^2 + \frac{\Gamma_m^2}{4}} \quad (1.12)$$

such that the oscillator's mean potential energy is

$$\langle U \rangle = \frac{M}{2} \int_0^\infty \Omega^2 S_x(\omega) \frac{d\Omega}{2\pi} = \frac{k_B T_{\text{bath}}}{2} \quad (1.13)$$

as expected. The susceptibility can be modified by additional damping and frequency shifts due to optomechanical coupling or coupling to the atomic ensemble while the thermal force remains constant, which will be discussed in the corresponding sections below. The bath temperature is usually the environment temperature, but can be increased by additional noise terms as well, thus creating an effective bath temperature. These modifications influence the displacement spectrum  $S_x(\Omega)$ , such that the temperature corresponding to the mean potential energy is changed to

$$T = T_{\text{bath}} \frac{\Gamma_m}{\Gamma_{\text{tot}}} \quad (1.14)$$

with total energy damping rate  $\Gamma_{\text{tot}}$ . This formula is valid as long as the quantum limits of the cooling are negligible.

### 1.1.2 Time domain evolution

The time evolution of a thermal state of a membrane oscillator is of particular interest, as a temperature measurement relies on measuring the oscillator mode's fluctuating energy over time. Analysing this evolution theoretically can help verifying measurement results and allows to quantify principle limitations in the temperature measurement. The results will be used to determine the uncertainty of temperature measurements.

Well above thermal equilibrium the oscillator's amplitude can be described by equation 1.4 with  $F(t) = 0$  and initial amplitude  $a_0$ . The amplitude decays as  $a(t) = a_0 e^{-\Gamma_m t/2}$  with energy decay rate  $\Gamma_m$  and the full motion is described as  $x_m(t) = a(t) \cos(\Omega_m t)$  (in the limit of a weakly damped oscillator). As the amplitude approaches the thermal amplitude  $\langle x_m^2 \rangle = k_B T / M \Omega_m^2$  its behaviour gets influenced by a random thermal force driving the membrane [54]

$$F(t) = \sqrt{2k_B T_{\text{bath}} M \Gamma_m} W(t) \quad (1.15)$$

with white noise term  $W(t)$ . This is a non-deterministic process, so no analytical solution for the time evolution exists. However, the time evolution can be simulated using a finite difference algorithm with discretised time. For a full simulation of the membrane motion using equation 1.4 the intrinsic damping  $\Gamma_m$  is replaced by a total damping  $\Gamma_m \rightarrow \Gamma_{\text{tot}}$  to account for additional damping as described in the next sections. In order to discretise time the terms in equation 1.4 are replaced by

[54]

$$\begin{aligned}
 \ddot{x}_m(t) &\rightarrow \frac{(x_i - x_{i-1})/\Delta t - (x_{i-1} - x_{i-2})/\Delta t}{\Delta t} = \frac{x_i - 2x_{i-1} + x_{i-2}}{\Delta t^2} \\
 \dot{x}_m(t) &\rightarrow \frac{x_i - x_{i-1}}{\Delta t} \\
 x_m(t) &\rightarrow x_i \\
 W(t) &\rightarrow w_i/\sqrt{\Delta t}
 \end{aligned} \tag{1.16}$$

with random Gaussian numbers  $w_i$  of zero mean and unit variance. When simulating a weakly damped harmonic oscillator resolving the motion requires very small time steps  $\Delta t \ll 1/\Omega_m$ . To circumvent this, one can switch to a rotating frame  $\tilde{x}_m = x_m e^{i\Omega_d t}$  with damped harmonic oscillator frequency  $\Omega_d = \sqrt{\Omega_m^2 - \Gamma_{\text{tot}}^2/4}$  and solution ansatz  $x_m(t) = a \cos(\Omega_d t + \phi) = (a' e^{-i\Omega_d t} + a'' e^{i\Omega_d t})/2$  with compared to  $\Omega_m$  slowly varying complex amplitudes  $a' = a e^{-i\phi}$  and  $a'' = a e^{i\phi}$ . Then the fast rotating term  $a''$  in  $\tilde{x}_m = 1/2(a' + a'' e^{+2i\Omega_d t})$  can be dropped in the rotating wave approximation and the differential equation 1.4 becomes

$$\frac{\dot{a}'}{2} + \frac{\dot{a}'}{2} (\Gamma_{\text{tot}} - 2i\Omega_d) + \frac{a'}{2} \left( \frac{\Gamma_{\text{tot}}^2}{4} - i\Omega_d \Gamma_{\text{tot}} \right) = \sqrt{\frac{2k_B T_{\text{bath}} \Gamma_m}{M}} W(t) e^{i\Omega_d t}. \tag{1.17}$$

For  $\Gamma_{\text{tot}} \ll \Omega_m$  and  $\dot{a}' \approx 0$  for a slowly varying amplitude the equation simplifies to

$$\dot{a}' + a' \frac{\Gamma_{\text{tot}}}{2} = \sqrt{\frac{2k_B T_{\text{Bath}} \Gamma_m}{M \Omega_m^2}} i W(t) e^{i\Omega_m t}. \tag{1.18}$$

Using replacement equations 1.16 (for  $a'$  instead of  $x_m$ ) and  $iW(t)e^{i\Omega_m t} \rightarrow w_i/\sqrt{\Delta t}$  with complex  $w_i$  one gets the iteration rule for complex amplitude  $a'_i$  with quadratures  $X_1 = (a'_i + a_i'^*)/2$  and  $X_2 = i(a'_i - a_i'^*)/2$  and displacement  $\langle x_m^2 \rangle = |a'_i|^2/2$  that is referred to the instantaneous temperature as  $T_i = M \Omega_m^2 |a'_i|^2 / 2k_B$ . The result of a simulation is shown in figure 1.2.

One can see in plot 1.2a the strong variations of instantaneous temperature  $T_i$  as it would be measured by a spectrum analyser in zero span mode, the corresponding quadrature evolution for the first half of the plot is shown in plot 1.2b. For much longer time scales a histogram of temperatures  $T_i$  shows the expected partition function  $p(T_i) = \exp(-T_i/T_{\text{bath}})$  for  $\Gamma_{\text{tot}} = \Gamma_m$  as shown in plot 1.2c, and the quadratures show a Gaussian distribution in plot 1.2d.

The fluctuations of  $T_i$  are  $\sigma(T_i) = T$ . In order to determine  $T$  precisely a sufficiently long measurement time  $\tau$  and averaging over  $N$  traces with sufficient time separation  $\gg 1/\Gamma_{\text{tot}}$  can be applied. The measurement uncertainty  $\Delta T$  is

$$\Delta T = \frac{T}{\sqrt{N(1 + \tau \Gamma_{\text{tot}}/2)}} \tag{1.19}$$

as determined using the simulation. For  $\tau \rightarrow 0$  and  $N = 1$  the error approaches  $T$  which is again the fluctuation of the thermal state. Additional measurement noise

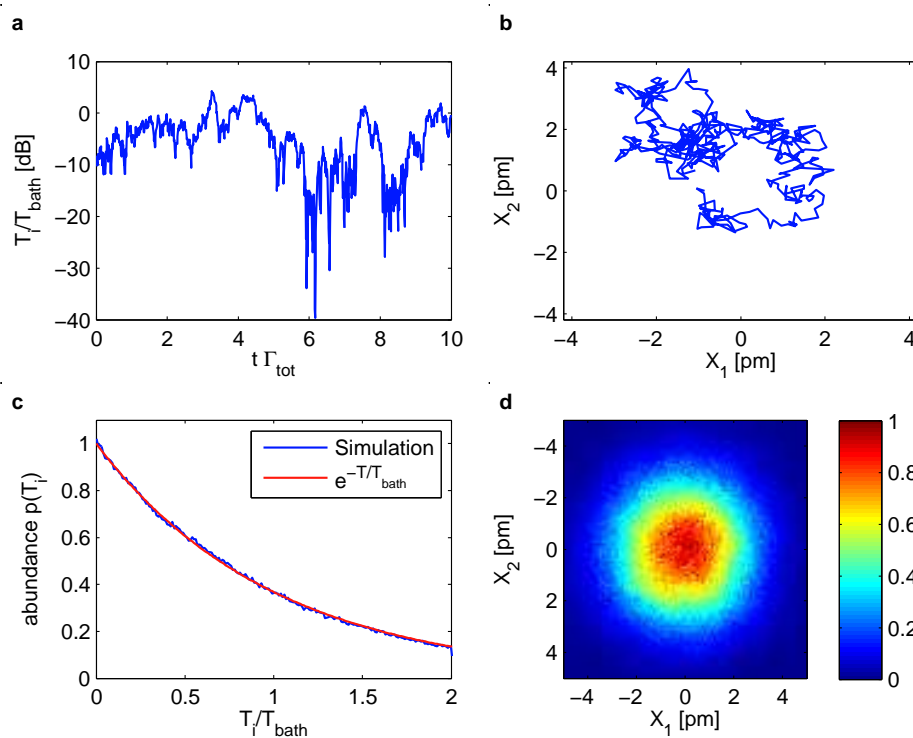


Figure 1.2: Simulated thermal motion of a membrane with  $\Omega_m/2\pi = 300$  kHz,  $Q = 3 \times 10^6$ ,  $T_{\text{bath}} = 100$  K,  $M = 100$  ng,  $\Gamma_m = \Gamma_{\text{tot}}$  and stepsize  $\Delta t = 1/100\Gamma_{\text{tot}}$ . **a:** time dependent instantaneous temperature  $T_i$  **b:** evolution of quadratures up to  $t = 5/\Gamma_{\text{tot}}$  **c:** normalized temperature abundance within a time window of  $10^4/\Gamma_{\text{tot}}$  and **d:** corresponding normalized phase-space histogram.

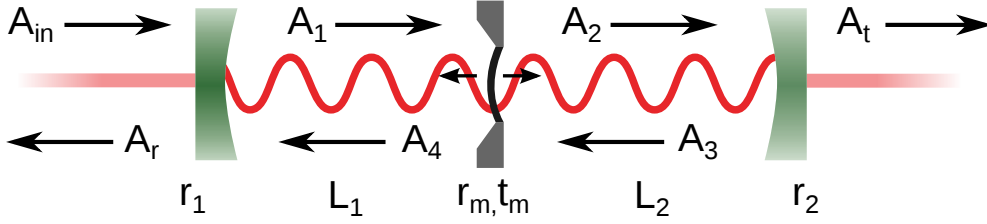


Figure 1.3: Schematics of the cavity-membrane system. An incoming beam with amplitude  $A_{in}$  is coupled into the cavity and is reflected with amplitude  $A_r$  or transmitted with amplitude  $A_t$ . The amplitudes inside the cavity are enumerated. The individual amplitude reflectivity  $r$  and transmittance  $t$  are indexed by the element mirror 1 and 2 and membrane  $m$ . The length of the partial cavities is  $L_1$  and  $L_2$ .

is not included, so this represents a lower intrinsic limit. In principle, the errorbar is slightly asymmetric because an actual temperature lower than the measured one would have lower  $\Gamma_{tot}$  and therefore lower  $\Delta T$ . For sufficiently small errors  $\Delta T \ll T$  this can be neglected.

## 1.2 Optomechanical system: membrane inside a cavity

Cavity-optomechanical systems represent a way of cooling mechanical oscillator modes. The technique relies on the change of an optical cavity's resonance frequency with the oscillator's position. The system has been implemented using different oscillators [4] like cantilevers with mirrors [5], integrated systems such as toroids [9], with microwave photons [20] or using a dielectric membrane inside a cavity [10, 11]. The membrane system has the advantage of disentangling the mechanical from the optical system. This way, the very high Q factor of the only tens of nm thin membrane with moderate reflectivity can be combined with a high finesse cavity, thus optimizing the cooling performance. This so called membrane in the middle system is used in this thesis with the modification of using a single sided cavity. It will therefore be analysed in the following in detail.

In the optomechanical system the membrane oscillator is situated inside a single sided optical cavity, which means that the cavity input mirror has much lower reflectivity than the output mirror  $r_1^2 < r_2^2 \approx 1$ , such that almost all the light is reflected on resonance. The system is sketched in figure 1.3, where a beam of amplitude  $A_{in}$  is coupled into the cavity and is reflected with amplitude  $A_r$  or transmitted with amplitude  $A_t$ . The system can be described as two cascaded cavities in one dimension, where the right cavity acts as a mirror with variable complex reflectivity  $r_r$  for the left cavity, which then only consists of two mirrors  $r_1$  and  $r_r$ . The membrane motion can be included as a length change of the subcavities  $L_1 + x_m$  and  $L_2 - x_m$ .

### 1.2.1 Cavity field

The steady state field amplitudes for incoupled light at frequency  $\omega_L$  with wave vector  $k_L = 2\pi/\omega_L$  can be calculated by separating the system into two subcavities. The right cavity has intra cavity field  $A_2$  and reflected field  $A_4$  with [55]

$$A_2 = \frac{t_m A_1}{1 - r_2 r_m e^{i2k_L L_2}} \quad (1.20)$$

$$A_4 = A_1 r_m - A_2 r_2 t_m e^{i2k_L L_2}. \quad (1.21)$$

This subcavity can be treated as a back mirror of the first cavity with complex reflectivity

$$\frac{A_4}{A_1} = \left( r_m - \frac{r_2 t_m^2 e^{i2k_L L_2}}{1 - r_2 r_m e^{i2k_L L_2}} \right) = r_r, \quad (1.22)$$

such that the left cavity field is

$$A_1 = \frac{t_1 A_{\text{in}}}{1 - r_1 r_r e^{i2k_L L_1}}. \quad (1.23)$$

The transmission and reflection of the whole cavity comes to

$$A_r = A_{\text{in}} \left( r_1 - \frac{t_1^2 r_r e^{i2k_L L_1}}{1 - r_1 r_r e^{i2k_L L_1}} \right) \quad (1.24)$$

$$A_t = \frac{t_1 A_{\text{in}}}{1 - r_1 r_r e^{i2k_L L_1}} \frac{t_m}{1 - r_2 r_m e^{i2k_L L_2}} t_2 e^{ik_L L_2}. \quad (1.25)$$

The light intensities are calculated as  $I_i = A_i A_i^*$ . The resonance condition can be analysed analytically as a function of membrane position  $x_m$  in the limit  $r_1 = r_2 \rightarrow 1$  for a membrane in the middle of the cavity with  $L_1 = L/2 + x_m$ ,  $L_2 = L/2 - x_m$  by solving for the extrema of intensity inside the cavity. For  $dI_t/d\omega_L(\omega_L = \omega_c) = 0$  a condition

$$\left[ L \sin\left(\frac{L\omega_c}{c}\right) - 2r_m x_m \sin\left(\frac{2x_m\omega_c}{c}\right) \right] \left[ r_m \cos\left(\frac{2x_m\omega_c}{c}\right) - \cos\left(\frac{L\omega_c}{c}\right) \right] = 0 \quad (1.26)$$

arises. The first term expresses the intensity minima, the second one the maxima. For  $x_m \ll L$  one can approximate  $2x_m\omega_c/c = 2k_L x_m$  to be constant compared to  $2L\omega_c/c$  under variation of  $\omega_c$ . This leads to solutions

$$\omega_c(x_m) = \frac{\omega_{\text{FSR}}}{\pi} \left( \pi \left( q + \frac{1}{2} (1 - (-1)^q) \right) + (-1)^q \arccos[|r_m| \cos(2k_L x_m)] \right) + \omega_0, \quad (1.27)$$

Here  $\omega_{\text{FSR}} = \pi c/L$  is the free spectral range (FSR) of the cavity,  $L = L_1 + L_2$  the total cavity length and  $q \in \mathbb{N}_0$  is the longitudinal mode number.  $\omega_0$  represents a global offset that includes phase shifts on reflection and transmission of the optical elements, that are otherwise not included in the formula due to  $|r_m|$ . Therefore, the refractive index of the membrane itself has no impact on the resonance frequencies

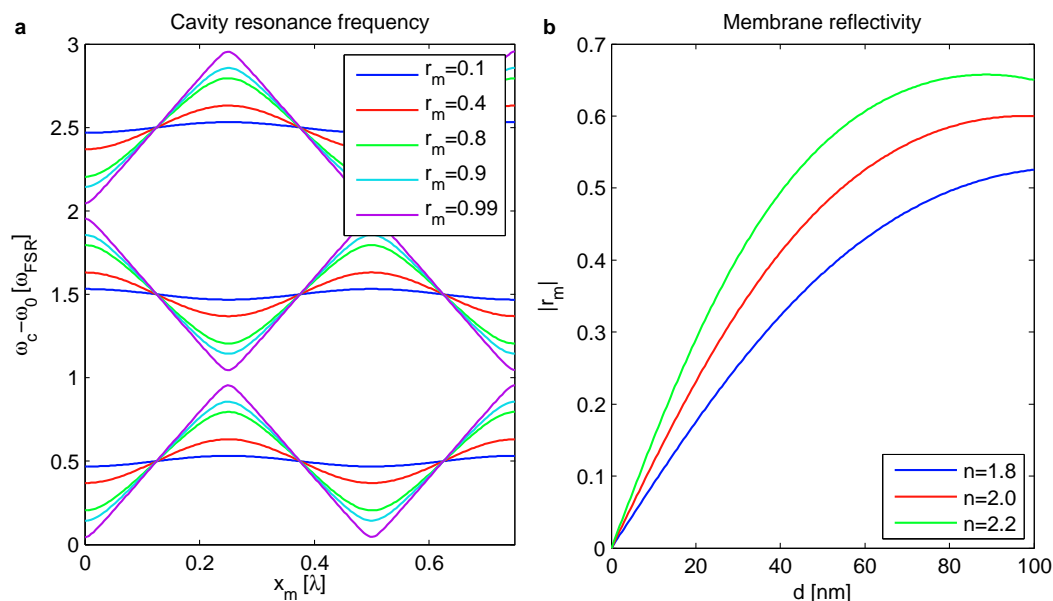


Figure 1.4: **a:** Cavity resonances  $\omega_c$  as a function of membrane position  $x_m$  for different membrane reflectivities  $r_m$ . **b:** membrane reflectivity as a function of membrane thickness  $d$  and refractive index  $n$ .

here. The formula approximately holds for  $r_1 \neq r_2 < 1$ . The cavity resonance frequency as a function of membrane reflectivity and position is shown in figure 1.4a using formula 1.27 for three longitudinal modes.

The amplitude reflection  $r_m$  and transmission  $t_m$  of the membrane are calculated for a thin plate of thickness  $d$  with complex refractive index  $n$  that also includes absorption losses inside the membrane[56]:

$$r_m = \frac{(n^2 - 1) \sin(k_L n d)}{2 i n \cos(k_L n d) + (n^2 + 1) \sin(k_L n d)} \quad (1.28)$$

$$t_m = \frac{2n}{2 i n \cos(k_L n d) + (n^2 + 1) \sin(k_L n d)}. \quad (1.29)$$

The absorption due to the imaginary part of the refractive index is  $a_m^2 = 1 - r_m^2 - t_m^2$ . The membrane reflectivity is shown in figure 1.4b as a function of thickness for different refractive index values.

The interaction of the membrane with the cavity field is characterized by the coupling strength  $G = -d\omega_c/dx_m$ , which corresponds to a cavity frequency change per displacement. The oscillation of the membrane periodically changes the resonance frequency, which gives rise to the optomechanical damping and optical spring effect, which are discussed below.

The optomechanical coupling strength  $G$  can be calculated using equation 1.27

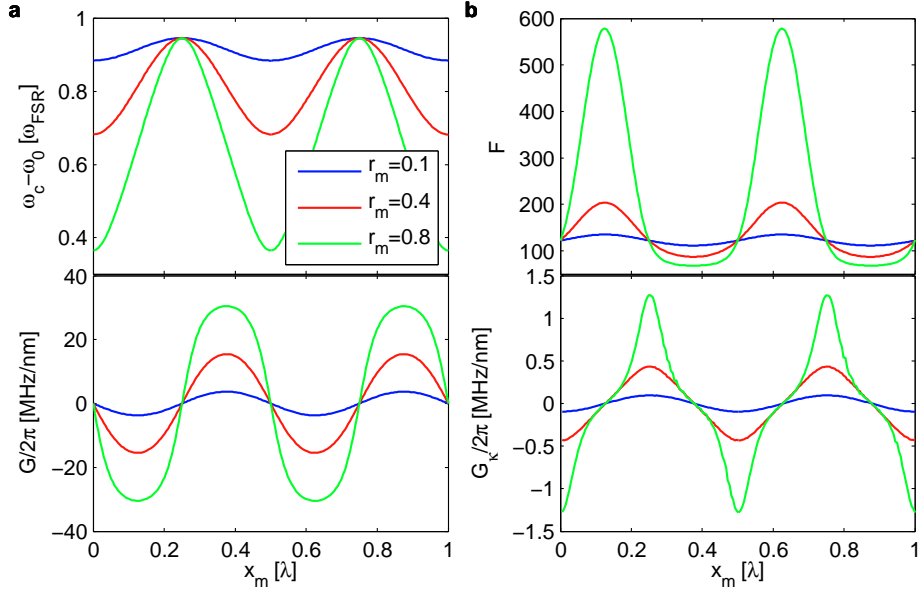


Figure 1.5: Numerically evaluated shift in **a**: resonance frequency  $\omega_c$  and **b** finesse  $\mathcal{F}$  as a function of membrane position  $x_m$  and corresponding dispersive  $G$  and dissipative  $G_\kappa$  coupling constant. The parameters are:  $r_1^2 = 0.95$ ,  $r_2^2 = 0.9999$ ,  $L_1 = L_2 = 0.01$  m. The numerical results of  $\omega_c - \omega_0$  are shifted compared to figure 1.4, because of the absolute value  $|r_m|$  used in the formula.

to be

$$G = -\frac{d\omega_c}{dx_m} = (-1)^q \frac{2\omega_L |r_m| \sin(2kx_m)}{L\sqrt{1 - |r_m|^2 \cos^2(2k_L x_m)}} \quad (1.30)$$

which can be approximated for  $|r_m|^2 \ll 1$  to

$$G = (-1)^q \frac{2\omega_L |r_m|}{L} \sin(2kx_m). \quad (1.31)$$

The membrane position dependent coupling strength is shown in figure 1.5a together with the numerically evaluated resonance frequencies calculated using the full equations 1.20 to 1.25 and an unphysically thin membrane with very large refractive index for illustrative purposes (otherwise the curves would not converge to the same frequency for  $\lambda/4$  and  $3\lambda/4$ ).

### 1.2.2 Cavity finesse

Besides the resonance frequency the Finesse  $\mathcal{F}$  is the defining parameter of a cavity. It is defined as

$$\mathcal{F} = \frac{\omega_{\text{FSR}}}{\kappa} \quad (1.32)$$

with  $\kappa$  being the full width at half maximum (FWHM) of a cavity resonance which is equivalent to the intensity decay rate. It corresponds to the average number of roundtrips a photon performs inside the cavity before it is lost. Figure 1.5b shows the numerically evaluated Finesse as a function of membrane position for different membrane reflectivities. The Finesse shows large variations, which is a result of the asymmetry of the cavity mirror reflectivities. The change in finesse equals a change in  $\kappa$ , which can be used to define a dissipative coupling strength  $G_\kappa \equiv d\kappa/dx_m$ . This dissipative coupling can in principle be exploited for optomechanical ground state cooling in the unresolved sideband limit [57, 58], but is not further discussed here, because the effect is weak in the experimental system. For membranes with enhanced reflectivity [59, 60] the dissipative coupling can become significant.

For  $\mathcal{F} \gg 1$  the resonance shape can be approximated as a Lorentzian

$$I(\Delta) = I_1 \frac{\frac{\kappa^2}{4}}{\frac{\kappa^2}{4} + \Delta^2} \quad (1.33)$$

with laser detuning  $\Delta = \omega_L - \omega_c$ .  $\kappa$  can be calculated for  $r_2 = 1$  at positions of maximum coupling  $\pm G_{\max}$ , resulting in two values

$$\kappa_{\max} = \frac{\omega_{\text{FSR}}(1-r_1)(1+r_m)}{\pi\sqrt{r_1}} \quad (1.34)$$

$$\kappa_{\min} = \frac{\omega_{\text{FSR}}(1-r_1)(1-r_m)}{\pi\sqrt{r_1}}. \quad (1.35)$$

Using this, the finesse comes to

$$\mathcal{F}_{\min} = \frac{\pi\sqrt{r_1}}{(1-r_1)(1+r_m)} \quad (1.36)$$

$$\mathcal{F}_{\max} = \frac{\pi\sqrt{r_1}}{(1-r_1)(1-r_m)}. \quad (1.37)$$

In the limit of vanishing membrane reflectivity the expected value for a simple single sided cavity  $\mathcal{F} = \pi\sqrt{r_1}/(1-r_1)$  is retrieved, which is also the value for membrane positions with  $G = 0$ . The finesse can be modelled using these results as

$$\mathcal{F}(x_m) = \frac{\pi\sqrt{r_1}}{(1-r_1)\left(1+r_m\frac{G(x_m)}{G_{\max}}\right)} \quad (1.38)$$

which approximately reproduces the numerical result. The field enhancement on resonance at the positions of highest and lowest finesse in the left partial cavity in the limit  $r_2 = 1$  can be calculated and is

$$I_1/I_{\text{in}} = \frac{1+r_1}{1-r_1} \approx \frac{2\mathcal{F}_{\min}}{\pi}(1+r_m) = \frac{2\mathcal{F}_{\max}}{\pi}(1-r_m) \quad (1.39)$$

for both configurations and for the right partial cavity

$$\begin{aligned} \left. \frac{I_2}{I_{\text{in}}} \right|_{\text{min}} &= \frac{1+r_1}{1-r_1} \frac{1-r_m}{1+r_m} \approx \frac{2\mathcal{F}_{\text{min}}}{\pi} (1-r_m) \\ \left. \frac{I_2}{I_{\text{in}}} \right|_{\text{max}} &= \frac{1+r_1}{1-r_1} \frac{1+r_m}{1-r_m} \approx \frac{2\mathcal{F}_{\text{max}}}{\pi} (1+r_m). \end{aligned} \quad (1.40)$$

At configurations with high finesse the cavity field is strongest in the right cavity, where it cannot leak out, whereas in the low finesse case the field is mostly in the left cavity, which can leak out via the front mirror.

The mean photon number inside the cavity  $\bar{n}_c$  can be calculated using the input-output formalism for a cavity [4] assuming the input mirror loss  $\kappa_{ex}$  is the only loss channel  $\kappa_{ex} = \kappa$ :

$$\bar{n}_c = \frac{\kappa}{\Delta^2 + (\kappa/2)^2} \frac{P_{\text{in}} \eta^2}{\hbar \omega_L}, \quad (1.41)$$

where  $\eta$  is the field incoupling efficiency into the cavity mode. Taking into account the Lorentzian resonance shape, the same result can be retrieved from calculating the stored energy on resonance as  $\bar{n}_c = P\tau/\hbar\omega_L$  with average circulating power  $P \propto I \rightarrow P = 2\mathcal{F}P_{\text{in}}\eta^2/\pi$  (equation 1.39 and 1.40 including  $\eta$ ) inside the cavity, round trip time  $\tau = 2L/c$  and photon energy  $\hbar\omega_L$  for both  $\mathcal{F}_{\text{min}}$  and  $\mathcal{F}_{\text{max}}$ .

### 1.2.3 Optomechanical damping and optical spring effect

A general introduction to optomechanics that includes also the complete theoretical description of the systems can be found in [4], a closer description of a membrane inside a cavity in [53]. I will only summarize the results in the following.

An optomechanical system consists of an optical cavity with energy decay rate  $\kappa$ , resonance frequency  $\omega_c$  and a mechanical oscillator with resonance frequency  $\Omega_m$  and energy damping rate  $\Gamma_m$ . The two systems couple as the motion of the mechanical oscillator changes the cavities resonance frequency and the resulting change in intracavity photon number changes the radiation pressure on the mechanical oscillator. The coupling is described by the cavity frequency pull per displacement  $G = d\omega_c/dx_m$ . The mechanical oscillator is typically a moving cavity end mirror[61, 5] or in our case a membrane inside a fixed cavity[10, 11], that changes the effective cavity length via its refractive index when moving from node to anti-node of the cavity field. The basic resulting dynamics can be described by a Hamiltonian

$$H = \hbar\omega_c(x_m)\hat{a}^\dagger\hat{a} + \hbar\Omega_m\hat{b}^\dagger\hat{b} = \hbar\omega_c\hat{a}^\dagger\hat{a} + \hbar\Omega_m\hat{b}^\dagger\hat{b} - \hbar g_0\hat{a}^\dagger\hat{a}(\hat{b} + \hat{b}^\dagger) \quad (1.42)$$

using  $\omega_c(x_m) \simeq \omega_c - G\hat{x}$  with creation/annihilation operators for the optical field  $\hat{a}^\dagger, \hat{a}$  and mechanics  $\hat{b}^\dagger, \hat{b}$  with  $\hat{x} = (\hat{b} + \hat{b}^\dagger)x_{\text{ZPF}}$  and oscillator zero point fluctuation  $x_{\text{ZPF}} = \sqrt{\hbar/2M\Omega_m}$  and single photon optomechanical coupling strength  $g_0 = Gx_{\text{ZPF}}$ . Using this, one can derive the full dynamics when adding damping terms, quantum noise and laser drive. However, for the experiments presented here the system is still in a

classical regime, such that it can be described as a classical harmonic oscillator that experiences a position dependent radiation pressure with delayed response.

The static membrane displacement due to the mean radiation pressure force

$$F_{\text{rad}} = \hbar G \bar{n}_c \quad (1.43)$$

is  $\delta x_m = 2g_0 \bar{n}_c x_{\text{ZPF}} / \Omega_m$  for small displacements  $\delta x_m$  such that  $G(x_m + \delta x_m) \approx G(x_m)$ . One can evaluate equation 1.4 with radiation pressure force  $F_{\text{rad}}$  and the time dependent cavity field amplitude  $|\alpha| = |\alpha_0 + \delta\alpha| = \sqrt{\bar{n}_c}$  around their time average values  $x_0$  and  $\alpha_0$  resulting in two coupled equations [62]

$$\begin{aligned} M\ddot{\delta x}_m + M\Gamma_m \dot{\delta x}_m + M\Omega_m^2 \delta x_m &= \hbar G \alpha_0 (\delta\alpha + \delta\alpha^*) \\ \dot{\delta\alpha} &= (i\Delta - \kappa/2)\delta\alpha + iG\alpha_0 \delta x_m \end{aligned} \quad (1.44)$$

with mean intracavity field amplitude  $\alpha_0$  with  $|\alpha_0|^2 = \bar{n}_c$  and change in amplitude  $\delta\alpha$ . Solving these equations in Fourier space leads to

$$\delta F_{\text{rad}} = \hbar G \alpha_0 (\delta\alpha + \delta\alpha^*) = -\frac{G^2 \hbar \bar{n}_c}{\omega_c} [A_+(\Omega) - A_-(\Omega)] \delta x_m \quad (1.45)$$

where  $A_{\pm}(\Omega)$  is defined as

$$A_{\pm}(\Omega) = \frac{i}{\kappa/2 \pm i(\Delta \pm \Omega)}. \quad (1.46)$$

The changed radiation pressure leads to a modified effective mechanical oscillators susceptibility

$$\chi_{\text{eff}}(\Omega)^{-1} = \chi(\Omega)^{-1} + G^2 \hbar \bar{n}_c [A_+(\Omega_m) - A_-(\Omega_m)]. \quad (1.47)$$

One can identify a change in oscillation frequency  $\delta\Omega_m$  and damping  $\Gamma_{\text{opt}}$  as optomechanical damping

$$\Gamma_{\text{opt}} = \frac{G^2 \hbar \bar{n}_c}{M\Omega_m} \text{Im} [(A_+(\Omega_m) - A_-(\Omega_m))] \quad (1.48)$$

$$= g_0^2 \bar{n}_c \left( \frac{\kappa}{\frac{\kappa^2}{4} + (\Delta + \Omega_m)^2} - \frac{\kappa}{\frac{\kappa^2}{4} + (\Delta - \Omega_m)^2} \right) \quad (1.49)$$

and optical spring effect

$$\delta\Omega_m = \frac{G^2 \hbar \bar{n}_c}{2M\Omega_m} \text{Re} [(A_+(\Omega_m) - A_-(\Omega_m))] \quad (1.50)$$

$$= g_0^2 \bar{n}_c \left( \frac{(\Delta + \Omega_m)}{\frac{\kappa^2}{4} + (\Delta + \Omega_m)^2} + \frac{(\Delta - \Omega_m)}{\frac{\kappa^2}{4} + (\Delta - \Omega_m)^2} \right). \quad (1.51)$$

In our system we operate in the unresolved sideband limit  $\kappa \gg \Omega_m$ , such that the equations simplify to

$$\begin{aligned}\Gamma_{\text{opt}} &\approx g_0^2 \bar{n}_c \frac{-4\Delta\kappa\Omega_m}{\left(\frac{\kappa^2}{4} + \Delta^2\right)^2} \\ \delta\Omega_m &\approx g_0^2 \bar{n}_c \frac{2\Delta}{\Delta^2 + \frac{\kappa^2}{4}}.\end{aligned}\tag{1.52}$$

For small detunings  $|\Delta| \ll \kappa$  as used in our system the equations simplify further to

$$\begin{aligned}\Gamma_{\text{opt}} &\approx g_0^2 \bar{n}_c \frac{-64\Delta\Omega_m}{\kappa^3} \\ \delta\Omega_m &\approx g_0^2 \bar{n}_c \frac{8\Delta}{\kappa^2}.\end{aligned}\tag{1.53}$$

This gives a ratio

$$\frac{\Gamma_{\text{opt}}}{\delta\Omega_m} = \frac{-8\Omega_m}{\kappa}.\tag{1.54}$$

For a red-detuned laser drive  $\Delta < 0$  the frequency shift to  $\Omega_m$  is negative  $\delta\Omega_m < 0$ , while the membrane damping is increased by  $\Gamma_{\text{opt}}$ . This leads to a reduced temperature of the mechanical oscillator:

$$T_{\text{opt}} = T_{\text{bath}} \frac{\Gamma_m}{\Gamma_m + \Gamma_{\text{opt}}}\tag{1.55}$$

with effective bath temperature  $T_{\text{bath}}$ . The phonon number associated with the oscillators temperature is

$$\bar{n} = \frac{k_B T}{\hbar\Omega_m}\tag{1.56}$$

in the limit  $k_B T \gg \hbar\Omega_m$ .

The mechanical oscillator can become unstable for two different regimes. First, in the case of positive detuning  $\Delta > 0$  the damping of the oscillator can become negative  $\Gamma_m + \Gamma_{\text{opt}} < 0$  as  $\Gamma_{\text{opt}}(\Delta > 0) < 0$ , which leads to a parametric instability and mechanical lasing [63, 4]. Second, for very large optical springs  $\delta\Omega_m \gtrsim -\Omega_m$  a bistability arises with two potential minima, where one lies at the radiation pressure minimum and the membrane is pushed towards it.

### 1.2.4 Impact of laser noise

Laser noise leads to a fluctuating laser power inside the optomechanical system and therefore exerts a force onto the mechanical oscillator via the fluctuating radiation pressure. This noise force acts as another thermal bath of temperature  $T_L$  that the oscillator is coupled to, such that an effective bath temperature  $T_{\text{bath}} = T_0 + T_L$  is created, with  $T_0$  being the bulk material temperature. This way, laser noise counteracts optomechanical damping and can thus limit the minimum achievable

mechanical oscillator temperature [64, 65]. Laser intensity noise directly acts on the membrane, while frequency noise is converted by the cavity into additional intensity noise. The laser temperature

$$T_L = T_0 \frac{S_{F,\text{int}}(\Omega_m) + S_{F,\text{freq}}(\Omega_m)}{S_{F,\text{th}}} \quad (1.57)$$

is calculated as the laser force noise relative to the thermal noise force  $S_{F,\text{th}} = 4M\Gamma_m k_B T_0$ . The noise terms are laser intensity force noise  $S_{F,\text{int}}$  and frequency force noise  $S_{F,\text{freq}}$  power spectral densities (PSD), which are evaluated at  $\Omega_m$ . For  $\Omega_m < |\Delta| \ll \kappa$  these terms are

$$S_{F,\text{int}}(\Omega_m) = (\hbar G \bar{n}_c)^2 S_I(\Omega_m) \quad \text{and} \quad (1.58)$$

$$S_{F,\text{freq}}(\Omega_m) = (\hbar G \bar{n}_c)^2 \left( \frac{8\Delta}{\kappa^2} \right)^2 S_\omega(\Omega_m), \quad (1.59)$$

with  $\hbar G \bar{n}_c$  the mean radiation pressure force experienced by the membrane and  $S_I(\Omega_m)$  the relative laser intensity noise PSD. The frequency noise  $S_\omega(\Omega_m)$  is converted to relative intensity noise by the prefactor  $(8\Delta/\kappa^2)^2$ . The noise temperature is dependent on laser power and increases it as  $T_L \propto \bar{n}_c^2 \propto P_{\text{in}}^2$ , which means it will overcome the cooling rate  $\Gamma_{\text{opt}} \propto \bar{n}_c$  with increasing input power and thus limit the minimal reachable temperature in the optomechanical cooling scheme. The minimum temperature can be calculated by minimizing equation 1.55 with respect to  $\bar{n}_c$ . It is

$$T_{\text{min}} = \frac{\kappa}{4G} \sqrt{\frac{\Gamma_m M T_0}{k_B}} \sqrt{\left( \frac{\kappa^2}{8\Delta} \right)^2 S_I(\Omega_m) + S_\omega(\Omega_m)} \quad (1.60)$$

and saturates with rising detuning if frequency noise is the dominating noise.

### 1.2.5 Quantum limits

On a fundamental level, the emission probability asymmetry for stokes and anti-stokes photons in the quantum mechanical theory sets a limit on the minimum achievable phonon number[4]. In the resolved sideband regime  $\Omega_m \gg \kappa$  this leads to a minimum possible final phonon occupation at optimal detuning  $\Delta = -\Omega_m$  of

$$\bar{n}_{\text{min}} = \left( \frac{\kappa}{4\Omega_m} \right)^2 < 1 \quad (1.61)$$

which enables groundstate cooling of the mechanical oscillator. In the case of our system with  $\kappa \gg \Omega_m$  the minimum possible occupation is

$$\bar{n}_{\text{min}} = \left( \frac{\kappa}{4\Omega_m} \right) \gg 1 \quad (1.62)$$

which means we wont be able to cool the oscillator to the groundstate using only optomechanical cavity cooling. As shown below, sympathetic cooling with atoms can give access to the ground state even for  $\kappa \gg \Omega_m$ .

### 1.2.6 Membrane motion readout

The oscillator's displacement PSD  $S_x(\Omega)$  is related to its temperature via the equipartition theorem as  $k_B T = M \Omega_m^2 \langle x^2 \rangle$  with displacement variance  $\langle x^2 \rangle = \int_0^\infty S_x(\Omega) d\Omega / 2\pi$ . The oscillation of the membrane inside the optical cavity can be read out via its influence on the cavity resonance frequency through  $G$ . For a single-sided cavity the phase shift of the beam reflected from the cavity with respect to the incoming beam is [4]

$$\phi = \arctan \left[ \frac{\kappa \Delta}{(\kappa/2)^2 - \Delta^2} \right], \quad (1.63)$$

and the derivative with respect to the detuning is

$$\frac{d\phi}{d\Delta} = \frac{\kappa}{(\kappa/2)^2 + \Delta^2}. \quad (1.64)$$

For  $|\Delta| \ll \kappa$  the derivative simplifies to  $d\phi/d\Delta \simeq 4/\kappa$ . A small membrane displacement  $x_m$  shifts the cavity frequency by  $\delta\omega_c = -Gx_m$  and thus the phase of the reflected beam by  $\delta\phi = -(d\phi/d\Delta)\delta\omega_c = (4/\kappa)Gx_m$ . This phase shift can be detected using a homodyne, heterodyne or Pound-Drever-Hall (PDH) technique [66, 67]. The achievable sensitivity  $S_x^{\text{imp}}(\Omega)$  is dependent on the number of photons interacting with the oscillator inside the cavity [4]

$$S_x^{\text{imp}}(\Omega) = \frac{\kappa}{16\bar{n}_c G^2} \left( 1 + 4 \frac{\Omega^2}{\kappa^2} \right) \quad (1.65)$$

The measurement also leads to a back action noise force onto the oscillator

$$S_F(\Omega) = \bar{n}_c \frac{4\hbar^2 G^2}{\kappa} \left( 1 + 4 \frac{\Omega^2}{\kappa^2} \right)^{-1} \quad (1.66)$$

such that an uncertainty relation  $S_F(\Omega) S_x^{\text{imp}}(\Omega) \geq \hbar^2/4$  holds. This minimum uncertainty represents the standard quantum limit [68]. The total measured signal is

$$S_x(\omega) = S_x(\Omega) + S_x^{\text{imp}}(\Omega) + S_F(\Omega) |\chi(\Omega)|^2. \quad (1.67)$$

in the optimal case with no excess readout noise and photon loss.

## 1.3 Trapping ultracold atoms

Trapping atoms in lattices and magneto-optical traps relies on light-matter interaction, which will be briefly reviewed in the following section. A rigorous description can be found in various books and reviews [69, 70, 71], which are the basis for the following. The theoretical description is based on the interaction of a two level atom with energy splitting  $\hbar\omega_{\text{eg}}$  and dipole moment  $\mu_{\text{eg}}$  with a fast oscillating electric field  $E = E_0 \cos(k_L z - \omega_L t)$  which represents a laser beam. The interaction term is  $\mathcal{H}_I = -\mu_{\text{eg}} E$ . This results in a coherent description of the system leading among

other things to a dipole force, which can be used to trap atoms in laser intensity maxima or minima. Taking into account the spontaneous decay of the upper state with rate  $\Gamma$  leads to the possibility of cooling atomic motion via the scattering force. The two cases will be discussed in the following.

### 1.3.1 Dipole force: Dipole trap

The energy shift of the groundstate of a two level system due to the interaction with a far off-resonant laser field is

$$V_0 = \frac{\hbar|\Omega_R|^2}{4\Delta_{LA}} \quad (1.68)$$

derived from dressed states of a driven two level system for large detuning  $|\Delta_{LA}| = |\omega_L - \omega_{eg}| \gg |\Omega_R|$  and Rabi frequency  $\Omega_R$ . For linearly polarized light with a detuning much larger than the excited state hyperfine splitting of the  $^{87}\text{Rb}$  D<sub>2</sub> line the Rabi frequency is  $|\Omega_R|^2 = \Gamma^2 I/2I_s$  with excited state lifetime  $\Gamma = 2\pi \times 6.06$  MHz [72] and saturation intensity  $I_s = \hbar\omega_{eg}^3\Gamma/12\pi c^2$  [72]. This leads to a potential

$$V_0 = \frac{\hbar\Gamma^2}{12\Delta_{LA}} \cdot \frac{I_0}{I_s}. \quad (1.69)$$

The intensity of an incident Gaussian beam with width  $w$  and power  $P_0$  with negligible divergence is [55]

$$I(r) = I_0 e^{-\frac{2r^2}{w^2}}, \quad I_0 = \frac{2P_0}{\pi w^2} \quad (1.70)$$

For a retro-reflected beam of same size with field amplitude reduced to a fraction  $\alpha$  the interference leads to an intensity distribution

$$I(r, z) = I_0 e^{-\frac{2r^2}{w^2}} \left| e^{ik_L z} + \alpha e^{-i(k_L z + \phi)} \right|^2 \quad (1.71)$$

for a laser wave vector  $k_L = 2\pi/\lambda$ . This can be simplified to

$$I(r, z) = I_0 e^{-\frac{2r^2}{w^2}} [1 - 2\alpha + \alpha^2 + 4\alpha \cos^2(k_L z + \phi/2)]. \quad (1.72)$$

The total potential then is

$$V_{\text{dip}}(r, z) = e^{-2r^2/w^2} [V_d - V_m \sin^2(k_L z + \phi/2)], \quad (1.73)$$

with maximum potential depth  $V_d = V_0(1 + \alpha)^2$  and modulation depth  $V_m = 4\alpha V_0$ . The photon scattering rate is closely related via

$$\Gamma_{sc} = V_{\text{dip}} \frac{\Gamma}{\hbar\Delta_{LA}}. \quad (1.74)$$

### 1.3. Trapping ultracold atoms

---

The axial and radial oscillation frequencies arising from the potential curvature in harmonic approximation are

$$\Omega_a(r) = \sqrt{\frac{2|V_m|k_L^2}{m}} e^{-r^2/w^2} \quad (1.75)$$

$$\Omega_r = \sqrt{\frac{-4V_d}{mw^2}} \quad (1.76)$$

for the axial ( $\Omega_a$ ) and radial ( $\Omega_r$ ) oscillation with atomic mass  $m$ . The axial oscillation is developed here as a function of radial coordinate, while the radial frequency is only given for the trap center. The ratio at the trap center is  $\Omega_a(0)/\Omega_r = 2k_L^2 w^2 \alpha / (1 + \alpha)^2 \gg 1$ . Note that the radial oscillation is only possible inside attractive potentials for  $\Delta_{\text{LA}} < 0$ . For repulsive potentials the axial oscillation is metastable for  $r = 0$ , so that additional radial trapping is required. The axial trap frequency scales as

$$\Omega_a(0) = \zeta \sqrt{P_0/|\Delta_{\text{LA}}|}, \quad \zeta = \sqrt{\frac{4\alpha k_L^2 \hbar \Gamma^2}{3\pi m w^2 I_s}}. \quad (1.77)$$

The center trap frequency  $\Omega_a(0)$  represents a maximum, while for large radial positions the frequency approaches 0. The potential depth can be expressed in terms of center trap frequency as

$$V_{\text{dip}}(\Omega_a) = \frac{(1 + \alpha)^2 m \Omega_a^2}{8\alpha k_L^2}. \quad (1.78)$$

The maximum potential depth  $V_d$  limits the allowed temperature in the trap. In addition, gravity introduces an additional potential  $V_g = -mgr$  that reduces this temperature. The gradient is  $2gm/k_B = 0.2 \text{ K/m}$  for rubidium. For a potential depth roughly smaller than the gravitational potential change over the width  $w$  the atoms are not trapped.

#### 1.3.2 Scattering force: Magneto-optical trapping

The absorption of photons and spontaneous decay open up the possibility of cooling atomic motion, as the absorption leads to a directed momentum transfer, while the spontaneous decay momentum transfer is isotropic and averages out to zero. The scattering rate of a two level atom is

$$R = \frac{\Gamma}{2} \frac{I/I_s}{1 + 4(\Delta_{\text{LA}}/\Gamma)^2 + I/I_s}, \quad (1.79)$$

which is accurate for a  $^{87}\text{Rb}$  atom driven on the cycling transition  $F = 2, m_F = 2 \leftrightarrow F = 3, m_F = 3$  of the  $D_2$  line where the two level approximation holds. For an atom moving towards a laser beam with detuning  $\Delta_{\text{LA}} < 0$  the Doppler shift of the laser light seen by the atom leads to a reduced detuning  $\Delta_{\text{LA}} - kv$  and

therefore increased scattering. For two counterpropagating laser beams the forces add up to a friction force that cools atomic motion but does not confine them in space. Adding a magnetic field gradient  $B(z) = Az$  creates a position dependent detuning due to the Zeeman effect  $\Delta_{\text{LA}} + \mu'B(x)/\hbar$  with a differential magnetic moment  $\mu' = (g_e M_e - g_g M_g)\mu_B$  and Bohr magneton  $\mu_B$ . The resulting force in the magneto-optical-trap (MOT) along one dimension is

$$\vec{F} = \beta\vec{v} - K\vec{r}, \quad K = \frac{\mu'A}{\hbar k}\beta, \quad \beta = -\hbar k^2 \frac{8I/I_s(\Delta_{\text{LA}}/\Gamma)}{\left[1 + I/I_s + \left(\frac{2\Delta_{\text{LA}}}{\Gamma}\right)^2\right]^2}. \quad (1.80)$$

for the approximation of a two level system. Adding two more beam pairs along the remaining dimensions gives a full three dimensional trapping and cooling. A MOT is typically operated around  $\Delta_{\text{LA}} \approx 2\Gamma$ , gradients of  $A = 10 \text{ G/cm}$  and  $I > I_s$ . The temperature limit of the two level approximation is given by the Doppler temperature  $T_d = \hbar\Gamma/2k_B = 146 \mu\text{K}$ . In a real MOT with multi-level rubidium atoms lower temperatures are achieved using sub-Doppler cooling methods like polarization gradient cooling, which is used in an optical molasses, but is also present in a MOT. Here a multi-level atom is moving in zero magnetic field along a polarization gradient created by counter propagating beams (same as in MOT), which creates a position and state dependent light shift and optical pumping between groundstate sublevels. It combines to an energy loss from optical pumping by the light shift splitting energy. The cooling is only efficient for sufficiently cold atoms and larger detuning  $|\Delta_{\text{LA}}| \gg \Gamma$ . Its fundamental temperature limit is the recoil temperature  $T_r = \hbar^2 k^2 / k_b m = 360 \text{ nK}$  and the momentum damping rate for the used  $\sigma^+\sigma^-$  configuration is

$$\Gamma_a \approx \frac{30}{17} \frac{\Gamma \hbar k_L^2}{\Delta_{\text{LA}} m} \quad (1.81)$$

for  $\Delta_{\text{LA}} \ll \Gamma$  [73].

## 1.4 Atom-membrane coupling mechanism

A fully quantized theory of the membrane-light-atom interaction has recently been published. It has been shown that the atom-membrane coupling is described by the Hamiltonian [45]

$$H_I = \hbar g_N \left( \hat{b}_m^\dagger \hat{b}_a + \hat{b}_a^\dagger \hat{b}_m \right), \quad (1.82)$$

with the coupling constant  $g_N$  given in equation 1.1 and creation/annihilation operators for atom  $b_a$  and membrane excitation  $b_m$ . In addition, the theory provides expressions for the relevant dissipation mechanisms, the quantum limits of sympathetic cooling, and the conditions for strong coupling.

The Hamiltonian describes the coupling in a lossless system. In our experiment, the cavity incoupling efficiency  $\eta < 1$  and the optical transmittance between atoms and cavity  $t < 1$  lead to photon loss. The main consequence for sympathetic cooling

is the appearance of a factor  $\eta^2 t^2$  in the cooling rate equation 1.2. More generally, the losses lead to an asymmetry in the coupling, and the theory of cascaded quantum systems is required to describe the dynamics. This has been analyzed in detail for a system where atoms in a lattice are coupled to a membrane without an optical cavity [46, 15]. The losses in the present system can be treated along similar lines.

### 1.4.1 Classical description

In the following the atom-membrane coupling strength is derived including the effect of photon loss, treating the light field classically. This is justified for our parameters where the light acts essentially as a “spring” between atoms and membrane and effects of retardation are negligible. For a single-sided cavity with intensity decay rate  $\kappa$  driven by a laser beam with detuning  $\Delta = \omega_L - \omega_c$  from cavity resonance, the phase shift of the beam reflected from the cavity with respect to the incoming beam is [4]

$$\phi = \arctan \left[ \frac{\kappa \Delta}{(\kappa/2)^2 - \Delta^2} \right], \quad (1.83)$$

whose derivative with respect to the detuning is

$$\frac{d\phi}{d\Delta} = \frac{\kappa}{(\kappa/2)^2 + \Delta^2}. \quad (1.84)$$

For a small detuning  $|\Delta| \ll \kappa$  one obtains  $\phi \simeq 0$  and  $d\phi/d\Delta \simeq 4/\kappa$ . A small membrane displacement  $x_m$  shifts the cavity frequency by  $\delta\omega_c = -Gx_m$  and thus the phase of the reflected beam by  $\delta\phi = -(d\phi/d\Delta)\delta\omega_c = (4/\kappa)Gx_m$ . This leads to a displacement of the minima of the optical lattice potential by

$$\delta x = \frac{-\delta\phi}{2k_L} = \frac{-2Gx_m}{\kappa k_L}, \quad (1.85)$$

see equation 1.73. In a harmonic approximation to the bottom of the lattice potential wells, the resulting force on each atom is  $F_a = m\Omega_a^2 \delta x = -(2G/k_L\kappa)m\Omega_a^2 x_m$ . The force on the center-of-mass of an ensemble of  $N$  atoms is  $F_{\text{cm}} = NF_a$ . For a membrane equilibrium position  $x_0$  from a cavity field node this results in

$$F_{\text{cm}} = -2|r_m| \frac{2\mathcal{F}}{\pi} \sin(2k_L x_0) N m \Omega_a^2 x_m = -K x_m, \quad (1.86)$$

where  $K$  is the coupling spring constant which couples the membrane displacement to the center-of-mass motion of the atoms in the lattice [15, 45, 47]. It is directly connected to the single-phonon coupling constant

$$g_N = K x_{m,0} x_{a,0} / \hbar, \quad (1.87)$$

where  $x_{m,0} = \sqrt{\hbar/2M\Omega_m}$  and  $x_{a,0} = \sqrt{\hbar/2Nm\Omega_a}$  are the quantum mechanical zero-point amplitudes of the membrane and atomic center-of-mass motion, respectively.

Conversely, an atom displaced by  $x_a$  from the bottom of the potential well experiences a restoring optical dipole force  $F_d = -m\Omega_a^2 x_a$ . On a microscopic level, this force is due to absorption and stimulated emission, leading to a redistribution of photons between the incoming and reflected laser beams which form the lattice potential [74]. Each absorption-emission event between the counterpropagating beams imparts a momentum kick of  $\pm 2\hbar k_L$  to the atom. For  $N$  atoms in the lattice, the corresponding photon redistribution rate is  $\dot{n}_p = NF_d/(2\hbar k_L)$ , which leads to a power modulation of the laser beam after it has passed through the atomic ensemble of

$$\delta P_0 = \dot{n}_p \hbar \omega_L = \frac{c}{2} N F_d, \quad (1.88)$$

where  $c$  is the speed of light. The power modulation of the coupling beam leads to a modulation of the mean photon number  $\bar{n}_c$  inside the cavity (equation 1.41). With cavity input power  $P_{\text{in}} = \eta^2 t^2 P_0$  and  $|\Delta| \ll \kappa$  a modulation  $\delta \bar{n}_c \simeq (4/\kappa) \eta^2 t^2 (\delta P_0 / \hbar \omega_c)$  is obtained. The mean radiation-pressure force experienced by the mechanical element on an optomechanical system is  $F_{\text{rad}} = \hbar G \bar{n}_c$ . The motion of the atoms in the lattice thus leads to a modulation of the radiation pressure force on the membrane of

$$\delta F_{\text{rad}} = \hbar G \delta \bar{n}_c = -\eta^2 t^2 (2G/k_L \kappa) N m \Omega_a^2 x_a \quad (1.89)$$

which results in

$$\delta F_{\text{rad}} = -\eta^2 t^2 2|r_m| \frac{2\mathcal{F}}{\pi} \sin(2k_L x_0) N m \Omega_a^2 x_a = -\eta^2 t^2 K x_a. \quad (1.90)$$

For a comparable displacement, the force on the membrane is thus smaller by a factor  $\eta^2 t^2$  than the corresponding force on the atoms[15].

The membrane vibrations and the atomic center-of-mass motion can be described as harmonic oscillators coupled through  $F_{\text{cm}}$  and  $\delta F_{\text{rad}}$ , with equations of motion [15, 47]

$$\begin{aligned} N m \ddot{x}_a &= -\Gamma_a N m \dot{x}_a - N m \Omega_a^2 x_a - K x_m, \\ M \ddot{x}_m &= -\Gamma_m M \dot{x}_m - M \Omega_m^2 x_m - \eta^2 t^2 K x_a + F_{\text{th}}, \end{aligned} \quad (1.91)$$

where  $F_{\text{th}}$  describes the fluctuating thermal force due to the coupling of the membrane to the environment at temperature  $T_{\text{bath}}$ . Since the atomic temperature is negligibly small in the experiment, the corresponding term is suppressed. Fourier transforming the equations of motion results in

$$\begin{aligned} \tilde{x}_a(\Omega) &= \chi_a(\Omega) [-K \tilde{x}_m(\Omega)] \quad \text{and} \\ \tilde{x}_m(\Omega) &= \chi_m(\Omega) [\tilde{F}_{\text{th}} - \eta^2 t^2 K \tilde{x}_a(\Omega)], \end{aligned} \quad (1.92)$$

with the mechanical susceptibilities

$$\begin{aligned} \chi_a(\Omega) &\simeq [2N m \Omega_a (\Omega_a - \Omega - i\Gamma_a/2)]^{-1} \quad \text{and} \\ \chi_m(\Omega) &\simeq [2M \Omega_m (\Omega_m - \Omega - i\Gamma_m/2)]^{-1}, \end{aligned} \quad (1.93)$$

that are approximated by a Lorentzian which is valid for  $\Omega_a \gg \Gamma_a$  and  $\Omega_m \gg \Gamma_m$ . Eliminating  $\tilde{x}_a$  in equations 1.92 results in the membrane amplitude

$$\begin{aligned}\tilde{x}_m(\Omega) &= \frac{\tilde{F}_{\text{th}}}{\chi_m^{-1}(\Omega) - \eta^2 t^2 K^2 \chi_a(\Omega)} \\ &= \frac{\tilde{F}_{\text{th}}}{2M\Omega_m \left( \Omega_m - \Omega - i\frac{\Gamma_m}{2} - \frac{\eta^2 t^2 g_N^2}{\Omega_a - \Omega - i\Gamma_a/2} \right)}.\end{aligned}\quad (1.94)$$

with

$$g_N = |r_m| \Omega_a \sqrt{\frac{Nm\Omega_a}{M\Omega_m}} \frac{2\mathcal{F}}{\pi} \frac{G}{G_{\text{max}}}\quad (1.95)$$

as already described. For  $\Gamma_a \gg g_N, \Gamma_m$  one can replace  $\Omega \rightarrow \Omega_m$  in the last term in the denominator and obtains

$$\begin{aligned}\tilde{x}_m(\Omega) &= \frac{\tilde{F}_{\text{th}}}{2M\Omega_m \left( \Omega_m - \delta\Omega_m - \Omega - i\frac{\Gamma_m + \Gamma_{\text{sym}}}{2} \right)} \\ &= \chi'_m(\Omega) \tilde{F}_{\text{th}},\end{aligned}\quad (1.96)$$

where

$$\Gamma_{\text{sym}}[N, \Omega_a] = \frac{g_N^2 \eta^2 t^2 \Gamma_a}{(\Omega_a - \Omega_m)^2 + (\Gamma_a/2)^2}\quad (1.97)$$

is the sympathetic cooling rate<sup>1</sup>,

$$\delta\Omega_m = (\Omega_a - \Omega_m) \Gamma_{\text{sym}} / \Gamma_a\quad (1.98)$$

a frequency shift of the membrane resonance, and  $\chi'_m(\Omega)$  the effective susceptibility of the membrane coupled to the atoms. The optomechanical effects present in the system for  $\Delta \neq 0$  can be added to the atom-membrane coupling terms, as the extra forces and thus modifications to the intrinsic mechanical susceptibility given by equations 1.47 and 1.96 add up. The resulting total damping  $\Gamma_{\text{tot}} = \Gamma_m + \Gamma_{\text{opt}} + \Gamma_{\text{sym}}$  leads to a final temperature of the mechanical oscillator of

$$T_{\text{sym}} = T_{\text{bath}} \frac{\Gamma_m}{\Gamma_{\text{tot}}}.\quad (1.99)$$

### 1.4.2 Ensemble-integrated sympathetic cooling rate

In the experiment, the cloud of molasses cooled atoms has a radius  $R_a$  that is much larger than the waist  $w$  of the coupling laser beam. Atoms at different radial positions  $r$  in the lattice show different axial vibration frequencies,  $\Omega_a(r) = \Omega_a(0)e^{-r^2/w^2}$ , see equation 1.75. In the system the atomic number density  $n_a$  in the molasses is approximately constant over the lattice profile. To quantitatively model

---

<sup>1</sup>There is a typo in [45], causing the cooling to be a factor 4 smaller

the sympathetic cooling rate in dependence of laser power, the sympathetic cooling rate has to be integrated over the lattice laser beam profile,

$$\Gamma_{\text{sym}}^{\text{int}} = 2R_a n_a \int_0^{R_a} dr 2\pi r \Gamma_{\text{sym}}[N = 1, \Omega_a(r)]. \quad (1.100)$$

Converting this to an integral over frequency leads to

$$\Gamma_{\text{sym}}^{\text{int}} = N_{\text{lat}} \int_{\Omega_a(R_a)}^{\Omega_a(0)} d\Omega_a \frac{\Gamma_{\text{sym}}[N = 1, \Omega_a]}{\Omega_a}, \quad (1.101)$$

where  $N_{\text{lat}} = 2R_a \pi w^2 n_a$  is the number of atoms in the lattice volume. Using equations 1.2 and 1.1 one obtains

$$\Gamma_{\text{sym}}^{\text{int}} = |r_m|^2 \frac{m N_{\text{lat}}}{M} \left(\frac{2\mathcal{F}}{\pi}\right)^2 \eta^2 t^2 \frac{\Gamma_a}{\Omega_m} \int_{\Omega_a(R_a)}^{\Omega_a(0)} d\Omega_a \frac{\Omega_a^2}{(\Omega_a - \Omega_m)^2 + (\Gamma_a/2)^2}. \quad (1.102)$$

Since  $R_a \gg w_0$  the lower integration limit can be set to  $\Omega_a(R_a) \rightarrow 0$  which results in

$$\begin{aligned} \Gamma_{\text{sym}}^{\text{int}} = \frac{4g_{N_r}^2 \eta^2 t^2}{\Gamma_a \pi} & \left\{ \left(1 - \frac{\Gamma_a^2}{4\Omega_m^2}\right) \left( \arctan \left[ \frac{2\Omega_m}{\Gamma_a} \right] + \arctan \left[ \frac{2(\Omega_a(0) - \Omega_m)}{\Gamma_a} \right] \right) \right. \\ & \left. + \frac{\Gamma_a}{2\Omega_m^2} \left( \Omega_a(0) + \Omega_m \ln \left[ \frac{\Gamma_a^2 + 4(\Omega_a(0) - \Omega_m)^2}{\Gamma_a^2 + 4\Omega_m^2} \right] \right) \right\}. \end{aligned} \quad (1.103)$$

Here,  $N_r = N_{\text{lat}}(\pi\Gamma_a/2\Omega_m) = \pi^2 R_a w^2 n_a \Gamma_a / \Omega_m$  is the number of resonantly coupled atoms and  $g_{N_r} = |r_m| \Omega_m \sqrt{\frac{N_r m}{M}} \frac{2\mathcal{F}}{\pi}$  the corresponding coupling constant. For  $\Gamma_a \ll \Omega_m$  one can approximate equation 1.103 as

$$\Gamma_{\text{sym}}^{\text{int}} \simeq \frac{4g_{N_r}^2 \eta^2 t^2}{\Gamma_a \pi} \left( \arctan \left[ \frac{2\Omega_m}{\Gamma_a} \right] + \arctan \left[ \frac{2(\Omega_a(0) - \Omega_m)}{\Gamma_a} \right] \right), \quad (1.104)$$

which is a step-like function with step width  $\Gamma_a$  and step height  $4g_{N_r}^2 \eta^2 t^2 / \Gamma_a$ .

### 1.4.3 Modifications in fully quantized calculation and coherent dynamics

In the fully quantized description given in [45] additional terms show up. First of all, the shot noise of the cavity photons leads to a membrane heating rate by momentum diffusion of

$$\Gamma_m^{\text{diff}} = \frac{16P_{\text{in}}}{Mc^2} \frac{\omega_L}{\Omega_m} |r_m|^2 \left(\frac{2\mathcal{F}}{\pi}\right)^2 \quad (1.105)$$

which results in a minimum phonon occupation

$$\bar{n}_1 = \frac{\Gamma_m n_{\text{bath}} + \Gamma_m^{\text{diff}}/2}{\Gamma_{\text{tot}}} \quad (1.106)$$

#### 1.4. Atom-membrane coupling mechanism

---

with  $n_{\text{bath}} = k_B T_{\text{bath}} / \hbar \Omega_m$  being the thermal bath occupation. A second term originates for strong damping of the atoms such that counter-rotating terms of the rotating wave approximation start playing a role

$$\bar{n}_2 = \left( \frac{\Gamma_a}{4\Omega_a} \right)^2. \quad (1.107)$$

Having  $\bar{n}_2 \ll 1$  corresponds to resolved sidebands of the atoms, which is equivalent to being able to groundstate cool the atoms. A third term describes the limitation due to atomic momentum diffusion caused by photon scattering  $\Gamma_a^{\text{diff}} = \Gamma_{\text{sc}}(k_L x_{a,0})^2$

$$\bar{n}_3 = \frac{\Gamma_a^{\text{diff}}}{2\Gamma_a}. \quad (1.108)$$

These terms add up to the total steady state occupation of the mechanical oscillator of

$$\bar{n}_{ss} = \bar{n}_1 + \bar{n}_2 + \bar{n}_3. \quad (1.109)$$

The cooperativity  $C$  is a general indicator for coherent dynamics and a value  $C > 1$  is the threshold for observing phenomena like electro-magnetically induced transparency (EIT)[75, 76]. For our atom-membrane coupling the cooperativity is defined as

$$C = \frac{4t^2 \eta^2 g_N^2}{\Gamma_a \Gamma_m} = \frac{\Gamma_{\text{sym}}}{\Gamma_m}. \quad (1.110)$$

Additional optomechanical damping  $\Gamma_{\text{opt}}$  and inhomogeneous broadening of  $\Gamma_a$  can increase the threshold. The optomechanical damping can be minimized by minimizing the optomechanical cavity length  $L$  and detuning  $\Delta$ .

A necessary condition for groundstate cooling is  $C > n_{\text{bath}}$  [47]. Additional requirements are  $\Gamma_{\text{sym}} < \Gamma_m^{\text{diff}}/2$ ,  $\Gamma_a < \Omega_a$  and  $\Gamma_a^{\text{diff}} < \Gamma_a$ , see equations 1.106 to 1.109. Here, additional optomechanical coupling only increases the damping, such that it has no negative influence in this case.

Another condition is the one for strong coupling  $2t\eta g_N > (\Gamma_m n_{\text{bath}}, \Gamma_m^{\text{diff}}/2, \Gamma_a)$ , which is equal to overcoming all decoherence rates in the system and enables the coherent exchange of excitations between the system. This can be fulfilled when being able to groundstate cool the membrane and switching off the atomic cooling  $\Gamma_a$ , if the inhomogeneous broadening of the atomic linewidth is small enough. This is not given in the situation of constant spatial atomic density.

In a scenario with an optimized parameter set of  $Q = 4 \times 10^7$ ,  $w = 100 \mu\text{m}$ ,  $\mathcal{F} = 1000$ ,  $\Omega_{m,(4,4)}/2\pi = 1 \text{ MHz}$ ,  $n_a = 10^{17} / \text{m}^3$ ,  $R_a = 3.5 \text{ mm}$ ,  $\Delta_{\text{LA}} = 2\pi \times 0.5 \text{ GHz}$ ,  $\Gamma_a = 10^5 / \text{s}$ ,  $\eta^2 = t^2 = 0.9$ ,  $r_m = 0.42$ ,  $\Delta = -0.01\kappa$ ,  $L = 1 \text{ mm}$ ,  $S_I(\Omega_{m,(4,4)}) = -156 \text{ dBc/Hz}$ ,  $T_0 = 4 \text{ K}$ ,  $a_m^2 = 4 \times 10^{-6}$ ,  $\kappa_{\text{th}} = 3 \text{ W/K m}$  a final phonon occupation  $\bar{n} < 1$  and thus the groundstate can be reached, as shown in figure 1.6.  $a_m^2$  and  $\kappa_{\text{th}}$  are the optical absorption and thermal conductivity, which characterize the thermal heating  $T_a$  of the membrane. They will be analysed in chapter 2. The challenge is to achieve a high enough atom density and low laser noise, while the

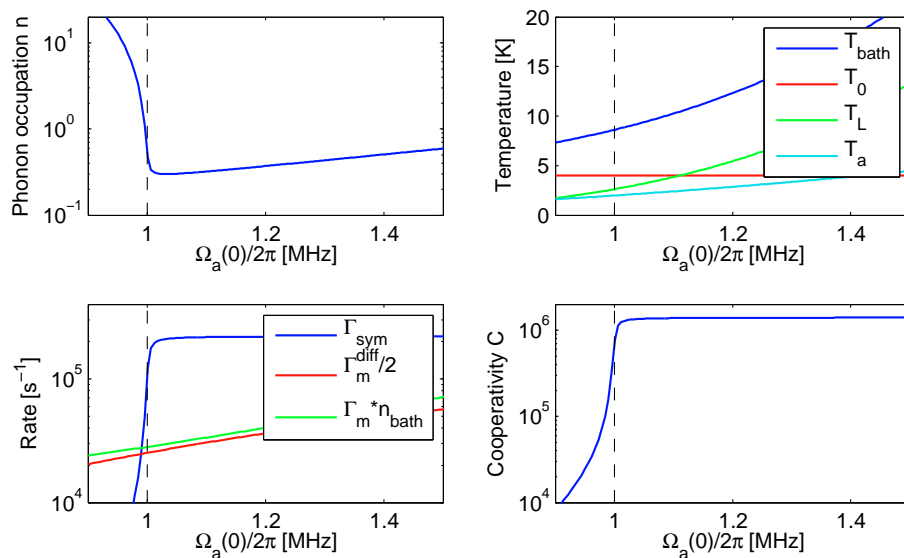


Figure 1.6: Evaluated parameters for sympathetic cooling as a function of lattice center atomic frequency  $\Omega_a(0)$ . The parameters are given in the text. The dashed line represents the membrane frequency  $\Omega_m$ .

largest uncertainty lies in the bulk membrane heating due to laser absorption  $a_m^2$  with thermal conductivity  $\kappa_{\text{th}}$ , which is discussed in chapter 5. The optimization is discussed in detail in the outlook.

#### *1.4. Atom-membrane coupling mechanism*

---

## Chapter 2

# SiN Membrane oscillators

In our experiments we investigate membranes made of Silicon Nitride (SiN) that have a typical thickness of only  $d \approx 50$  nm, whereas the lateral dimensions on the mm scale are macroscopic. These membranes are known to have very high quality factors  $Q > 10^6$  and are therefore used in a variety of experiments aiming at observing quantum behaviour of mechanical systems [77, 11, 68, 78, 15, 10]. They are commercially available<sup>1</sup> and were originally developed as transmission electron microscopy windows. In the following, their basic material and mechanical properties will be discussed, followed by a deeper analysis of the loss mechanisms using a novel frequency tuning method that we developed for low-stress membranes [79]. After that, a comparison to high-stress stoichiometric membranes is made. Parts of this chapter are published in [79].

### 2.1 Basic properties

Silicon nitride membranes are produced by microfabrication methods, as shown in figure 2.1a. A silicon nitride film is evaporated onto a quadratic silicon substrate of  $200 \mu\text{m}$  thickness and 5 mm side length using low-pressure chemical vapour deposition (LPCVD). Afterwards, the substrate is back-etched locally, resulting in a free standing SiN membrane on a silicon frame. There are two types of SiN membranes, so called low-stress  $\text{SiN}_x$  with typically  $4/3 > x > 1$  and high-stress, stoichiometric  $\text{Si}_3\text{N}_4$  membranes. The membrane can perform out-of-plane vibrations, that is described as the motion of a rectangular drum. The vibrational mode functions of a square membrane are given by [80]

$$\phi(x, y) = \cos\left(\frac{m\pi x}{l}\right) \cos\left(\frac{n\pi y}{l}\right) \quad (2.1)$$

with the mode numbers  $(m, n)$ , labelled by the number of anti-nodes  $m$  and  $n$  along the two dimensions, and the side length  $l$ . The modes up to  $(3, 3)$  are shown in

---

<sup>1</sup>We are using membranes from Norcada, [www.norcada.com](http://www.norcada.com)

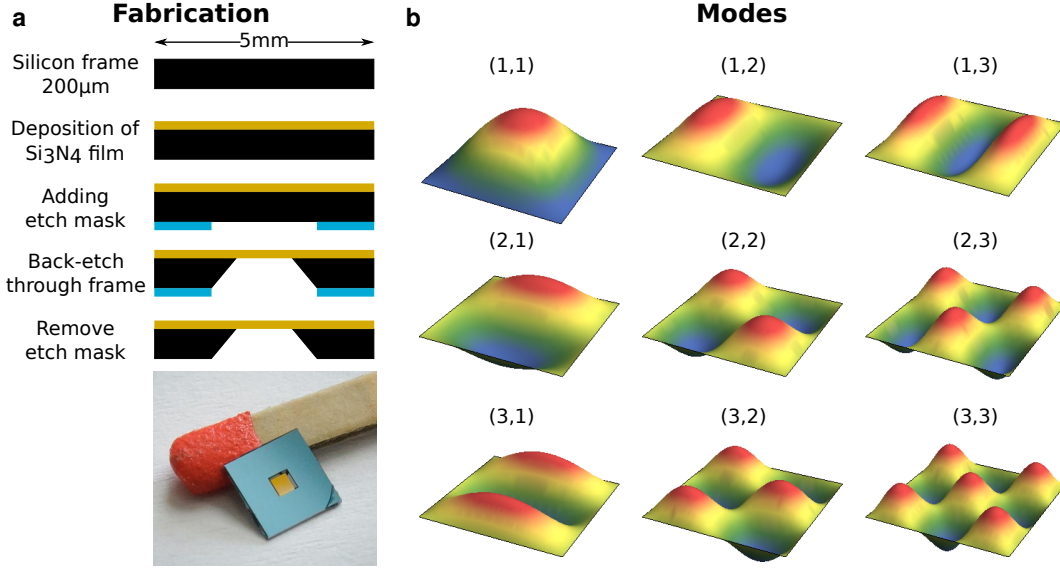


Figure 2.1: **a**: Schematic of the membrane fabrication process and picture of a membrane ( $l = 1$  mm,  $t = 100$  nm). The apparent color depends on viewing angle and membrane thickness. **b**: Calculated membrane mode functions up to (3,3). Complementary modes  $\Omega_{m,n}$  and  $\Omega_{n,m}$  have the same frequency and can hybridize.

figure 2.1b. The frequencies of these modes are described by [80]

$$\Omega_{m,n} = \frac{\pi}{l} \sqrt{\frac{S}{\rho} (m^2 + n^2)}, \quad (2.2)$$

with the mass density  $\rho$  and tensile stress  $S$ . The tensile stress of the membrane is caused by the lattice mismatch between silicon and silicon nitride during the evaporation process and can be modelled as a membrane length change out of equilibrium  $l_0$  by tensile stress  $S = E(l - l_0)/l_0$  with  $E$  being the Young's modulus. The tensile stress dominates over the elasticity modulus by orders of magnitude due to the large aspect ratio and large tensile stress, such that the elasticity modulus can be neglected. A spectrum of the membrane displacement PSD in figure 2.2 shows the membrane frequencies as peaks. Complementary modes  $\Omega_{m,n}$  and  $\Omega_{n,m}$  with  $m \neq n$  are in theory degenerate, but due to slightly different side lengths  $l$  along the axes, their frequencies differ by typically  $< 100$  Hz.

The basic material properties are summarized in table 2.1. Notice that the properties of low stress SiN<sub>x</sub> membranes can vary from membrane to membrane, as the exact material composition is not well defined.

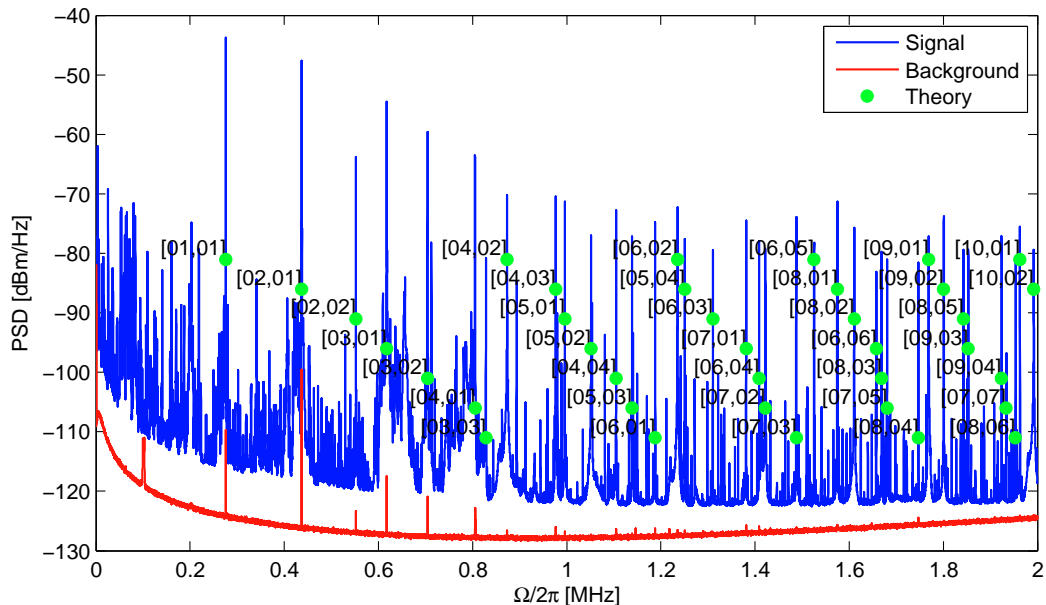


Figure 2.2: Measured uncalibrated displacement PSD of a high-stress membrane with  $l = 1.5$  mm and  $d = 50$  nm. The marked points represent the expected frequencies based on the fundamental frequency with deviations from the measured frequencies  $< 500$  Hz. The spectrum was recorded from a membrane inside a cavity using homodyne detection, as discussed in section 6.1, and 100 Hz bandwidth. The red line represents the measurement background. The (5,5) does not appear, as it is degenerate with the (7,1) mode. Other mechanical modes of the mirrors and membrane mount show up as smaller peaks.

	Low-stress	High-stress	Source
Density $\rho$	2900 kg/m <sup>3</sup>	2700 kg/m <sup>3</sup>	[81, 11]
Youngs modulus $E$	260 GPa	325 GPa	[82, 83]
Tensile stress $S_0$	60-200 MPa	920 MPa	
Refractive index at $\lambda = 780$ nm	2.2	2.0	[83, 11]
Expansion coefficient $\alpha$	1.6 ppm/K		
Thermal conductivity at 300 K $\kappa_{th}$	3 W/K m	25 – 36 W/K m	[81, 84]
Absorption $\text{Im}[n]$ at $\lambda = 780$ nm	$0.2 \dots 1.7 \times 10^{-3}$	$4 \times 10^{-6}$	

Table 2.1: Basic material properties for stoichiometric high-stress and low-stress SiN membranes. Values without source are measured in this thesis.

## 2.2 Quality factor analysis

The source and limitation of the membrane's exceptional mechanical quality factor  $Q$  is subject of intense research [85, 86, 87, 88, 89, 90, 91, 92], but not yet completely understood. In the following, we use absorption of laser light to reversibly tune the frequency of a membrane and use this to investigate the quality factors frequency dependence.

### 2.2.1 Frequency tuning

Silicon nitride membranes, especially low-stress membranes, absorb laser light at  $\lambda = 780 \text{ nm}$  [93]. The heating results in a thermal expansion of the membrane, such that the tensile stress  $S$  is reduced, leading to a reduction of the membranes oscillation frequency. This method of frequency tuning has the advantage that the frequency dependence of  $Q$  can be studied with a single membrane *in situ*, resulting in a detailed spectrum of the coupling to the environment of this particular mode. Other methods that compare  $Q$  between various structures of different sizes have to rely on the assumption that the environment of all these structures is comparable [90].

In order to systematically investigate the  $Q$  factor an experimental setup as depicted in figure 2.3 is used. The frame is glued at one edge to a holder inside a

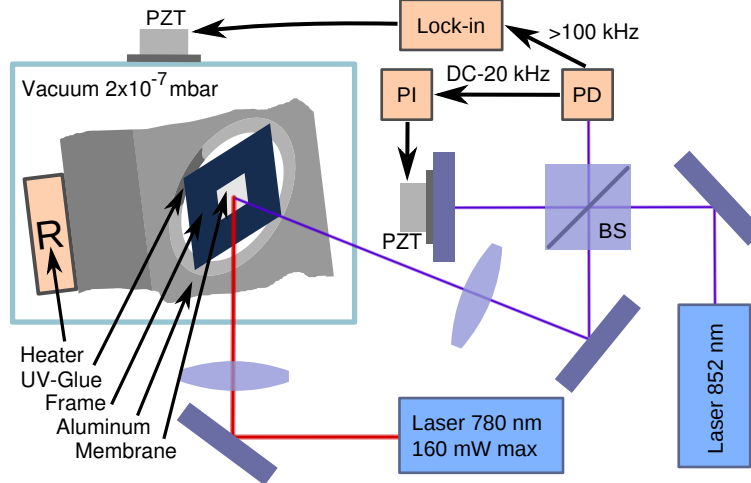


Figure 2.3: Membrane frequency tuning setup. The SiN membrane in a Si frame is glued at one edge to an aluminium holder inside a room-temperature vacuum chamber. The heating laser (red) at  $\lambda = 780 \text{ nm}$  is power stabilized to  $2 \times 10^{-4}$  RMS in a bandwidth of 12 kHz, and focused onto the membrane under an angle. The membrane vibrations are read out with a stabilized Michelson interferometer (blue). The interferometer signal is also used for feedback driving of the membrane with a piezo (PZT). A picture of the setup is also shown in figure A.2 in the appendix.

vacuum chamber using a small amount of UV curable glue. Several membranes are arranged inside a vacuum chamber, that is pumped down to  $\approx 10^{-7}$  mbar using an ion pump [94]. To read out the membrane vibrations, a Michelson interferometer operating at  $\lambda = 852$  nm is used, where one end mirror consists of the membrane. The interferometer is stabilized by the DC to 20 kHz part of the photodiode (PD) signal. The incident power on the membrane is  $580 \mu\text{W}$  in a diameter of  $2w_L = 150 \mu\text{m}$  and the position sensitivity is  $1 \times 10^{-14}$  m/ $\sqrt{\text{Hz}}$ . The  $> 100$  kHz frequency components of the signal are fed into a lock-in amplifier with integrated phase locked loop, which measures the membrane amplitude and drives its motion via a piezo mounted outside the vacuum chamber. To tune the membrane frequency, a power stabilized 780 nm laser is focused onto the membrane to a diameter of  $350 \mu\text{m}$ . This laser heats the membrane locally in its center. A second method of heating the whole membrane and frame is by a resistive heater (R) in the chamber.

The mode spectrum of a low stress  $l = 0.5$  mm,  $d = 50$  nm membrane as a function of heating laser power  $P$  is shown in figure 2.4a. One can see a decrease of all mode frequencies  $\Omega_{m,n}$  with  $P$ , which is reversible. Additional features like avoided crossings of modes (figure 2.4b) and different shifts due to mode hybridization (figure 2.4a,d) can be observed. There, the (1,3)+(3,1) mode has a much larger center amplitude than the (1,3)-(3,1) mode and therefore experiences a larger frequency shift. The decrease in frequency can be attributed to a thermal expansion of the membrane

$$\Delta l_0/l_0 = \alpha_0 \Delta T + \alpha_1 \Delta T^2 \quad (2.3)$$

where  $\Delta l_0$  is the equilibrium length change and  $\alpha_0$  ( $\alpha_1$ ) the first (second) order expansion coefficient for a temperature change  $\Delta T$ . This reduces the tensile stress by  $\Delta S = -E (\Delta l_0/l_0)$ . In a simple model assuming a spatially homogeneous and linear temperature change with power  $\Delta T = \chi P$ , one can describe the power-dependence of the stress as

$$S = S(P=0) - E (\Delta l_0/l_0) = S_0 - E (\alpha_0 \chi P + \alpha_1 \chi^2 P^2). \quad (2.4)$$

A fit of  $\Omega_{1,1}(P)/2\pi = \sqrt{a + bP + cP^2}$  to the data describes the observed dependence within  $\pm 1$  kHz (figure 2.3c). For low  $P$  a linear shift of  $\Delta\Omega_{1,1}/2\pi = -363$  Hz/mW can be observed. The dependence of  $E$  on  $\Delta T$  can be neglected because it is small [82, 95].

In order to extract  $\chi$  from the fit, one has to measure  $\alpha_0$ . This is done by heating up the whole sample holder with the resistive heater. In this case both  $l$  and  $l_0$  change and the difference in the linear expansion coefficients  $\Delta\alpha = \alpha_f - \alpha_0$  of the frame and the membrane determines  $S - S_0 = E\Delta\alpha\Delta T$ . Heating the setup by  $\Delta T = 16$  K measured using a built in temperature sensor and using [82]  $E = 260$  GPa and [96]  $\alpha_f = 2.6$  ppm/K, one gets  $\alpha_0 = 1.6$  ppm/K,  $\alpha_1 = 1.3 \times 10^{-8}/\text{K}^2$  and  $\chi = 0.6$  K/mW. This yields an average membrane temperature of  $T = 100^\circ\text{C}$  for  $P = 160$  mW of heating laser power.

To model laser absorption in the membrane, one can perform a finite element (FEM) simulation of laser heating [97] using a Gaussian beam profile and a SiN

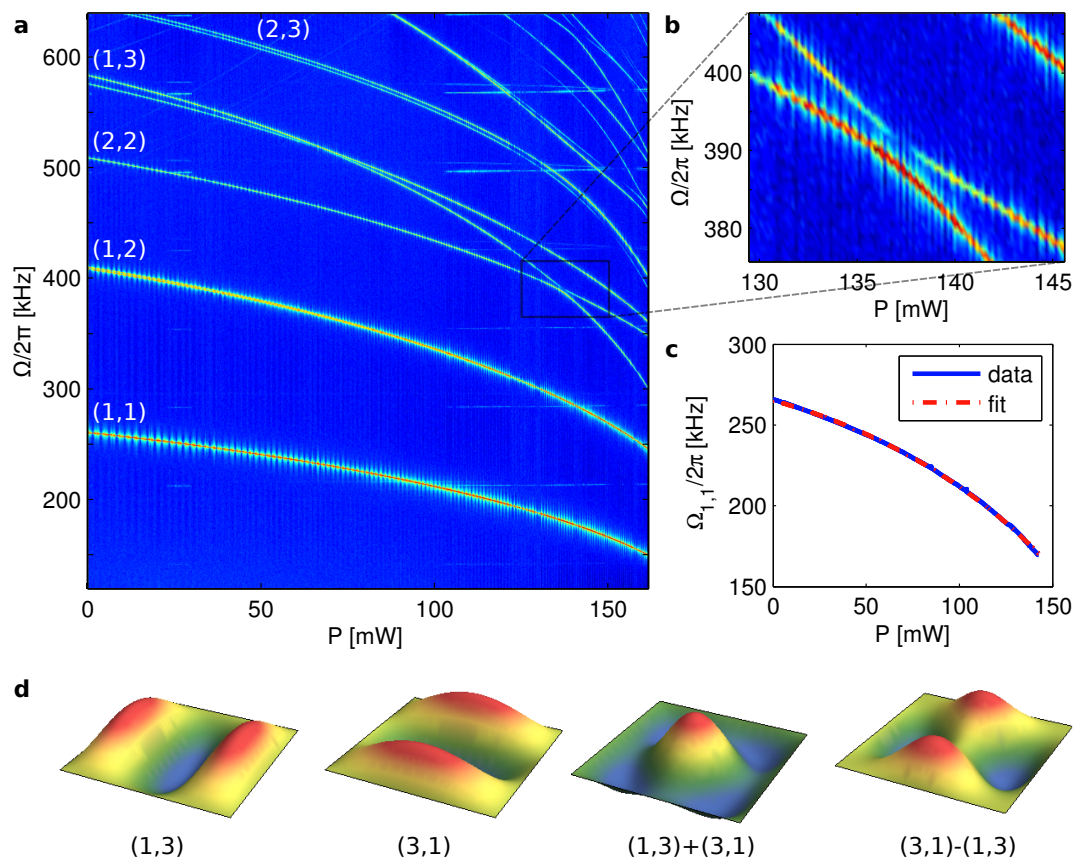


Figure 2.4: **a**: Mode spectrum  $\Omega_{m,n}$  of a low-stress membrane ( $l = 0.5$  mm, thickness  $d = 50$  nm) as a function of incident laser power  $P$ . At  $P = 0$ , the lowest 13 modes lie within 2% of the expected frequency. At higher  $P$ , anticrossings between higher order modes are visible. **b**: Zoom into avoided crossing showing coupling between mechanical modes. **c**: Fit to the fundamental membrane mode frequency shift. **d**: Mode hybridization, that can explain the different tuning behaviours of the (3,1) and (1,3) mode. The symmetric hybrid mode with large center amplitude is stronger influenced by the central heating than the asymmetric one with zero amplitude in the center.

heat conductivity [81]  $\kappa_{\text{th}} = 3 \text{ W/K m}$  and assuming the frame temperature does not change. From the resulting temperature distribution the average membrane temperature can be calculated for a given absorbed laser power. By comparing with  $\chi$ , one finds that a fraction of  $a_m^2 = 1.7 \times 10^{-3}$  of the  $\lambda = 780 \text{ nm}$  laser power is absorbed, corresponding to a refractive index imaginary part of  $\text{Im}(n) = 1.6 \times 10^{-3}$  (equations 1.28 and 1.29). This is an order of magnitude larger than the absorption in low-stress membranes at  $\lambda = 1064 \text{ nm}$  [10, 77]. Alternatively, the temperature increase by absorption can be calculated by solving the heat equation

$$\rho c_p \frac{\partial T}{\partial t} = \kappa_{\text{th}} \nabla^2 T + Q_{\text{th}} \quad (2.5)$$

with specific heat capacity  $c_p$  and heat source per volume  $Q_{\text{th}}$ . For a flat top laser beam profile of radius  $w < l/2$  and a round membrane of diameter  $l$  the average temperature increase is

$$\Delta T = \frac{P_{\text{abs}}}{4\pi\kappa_{\text{th}}t} \left( 1 - 2 \left( \frac{w}{l} \right)^2 \right). \quad (2.6)$$

The resulting temperature increases differ only by a few percent from the FEM simulation of a square membrane for  $w < l/2$ . A more detailed description is given in [45]<sup>2</sup>.

### 2.2.2 Mechanical dissipation mechanisms

Using the described method of frequency tuning, one can record a spectrum of the quality factor  $Q$  as a function of  $\Omega_{m,n}$ . The decay time  $\tau = 2/\Gamma_m$  of the membrane amplitude is measured in ring-downs after driving it to an amplitude of  $\approx 0.5 \text{ nm}$ . The upper plot in figure 2.5 shows the dissipation

$$Q^{-1} = \frac{2}{\Omega_{m,n}\tau} \quad (2.7)$$

of the fundamental membrane mode. For each data point an average over five ring-downs is taken. Distinct resonances are observed, changing  $Q$  by more than two orders of magnitude. The resonances in  $Q^{-1}$  can be attributed to coupling of the membrane mode to modes of the frame. To prove this, the interferometer is pointed onto the frame next to the membrane and the amplitude response to a driving with the piezo is recorded, as shown in the lower plot in figure 2.5. The observed frame modes clearly overlap with the resonances in  $Q^{-1}$ . To show that the spectrum directly depends on  $\Omega_{1,1}$  and not on  $P$ , the heating laser is pointed off center such that a different dependence  $\Omega_{1,1}(P)$  results, see figure 2.6a. The dependence  $Q^{-1}(\Omega_{1,1})$  is unchanged, showing that  $Q$  only indirectly depends on  $P$ . If the frame is heated with the resistive heater, one observes a shift in the resonances in  $Q^{-1}(\Omega_{1,1})$ , as shown in figure 2.6b. One can explain this by a shift of

---

<sup>2</sup>There is a typo in the corresponding equation C6 of [45]

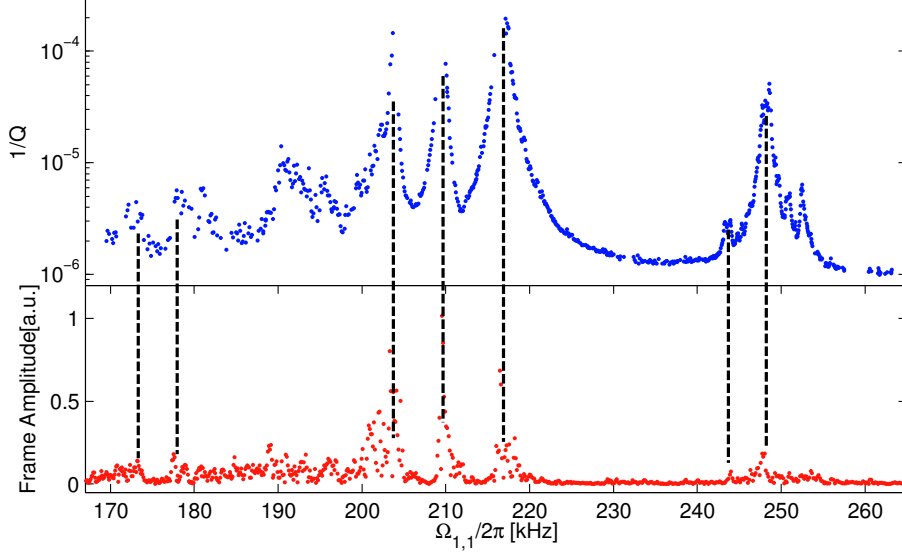


Figure 2.5: Upper plot: spectrum of membrane dissipation  $Q^{-1}(\Omega_{1,1})$ , showing a variation over two orders of magnitude. Lower plot: vibrations of the frame measured close to the membrane. The resonances in  $Q^{-1}(\Omega_{1,1})$  coincide with the frame modes.

the frame modes due to thermal expansion and decreasing Young’s modulus [95]. All these measurements prove that the coupling to frame modes is responsible for the observed behavior of  $Q$ . A FEM simulation of the frame modes shows roughly the right amount of modes in the frequency range of interest. As the eigenfrequencies depend strongly on the exact mounting, dimensions, and Young’s modulus of the frame, it is difficult to model them quantitatively. Besides coupling to frame modes, the frequency dependence of other dissipation mechanisms is of interest. Figure 2.6c shows the dissipation spectrum of another low-stress membrane. Away from the resonances, a constant baseline  $Q_{\max}$  can be observed, indicating that other dissipation mechanisms are independent of  $\Omega(S)$  and  $T$  within our tuning range, and  $Q$  is not being limited by clamping losses. This is in contrast to what has been observed in SiN strings [85, 88].

### 2.2.3 Further Q factor dependencies

Furthermore, the frequency dependent  $Q$  factor for higher order modes can be investigated. The resulting losses  $Q^{-1}$  are shown in figure 2.7 as a function of the mode frequency for the same membrane as in figure 2.5. The spectrum shows that some modes couple much stronger to support modes than others. In general, modes with higher symmetry seem to have lower losses on average. Especially symmetric modes  $\Omega_{n,n}$  are likely to have lower losses, as well as modes with even mode num-

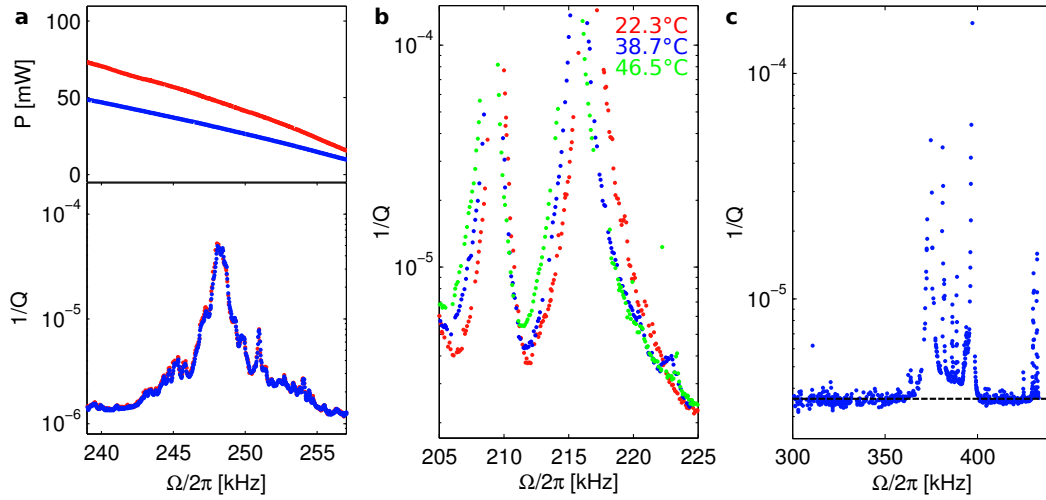


Figure 2.6: **a:**  $\Omega_{1,1}(P)$  and  $Q^{-1}(\Omega_{1,1})$  for different heating laser positions (membrane center: blue, off-center: red). The spectra  $Q^{-1}(\Omega_{1,1})$  overlap, indicating that  $Q$  is directly dependent on frequency. **b:**  $Q^{-1}(\Omega_{1,1})$  for different sample holder temperatures. Heating shifts the frame modes to lower frequencies. **c:** Spectrum of membrane dissipation  $Q^{-1}(\Omega_{1,1})$  for another membrane ( $l = 250 \mu\text{m}$ ,  $d = 50 \text{ nm}$ ). Besides coupling to frame modes, the dissipation is independent of frequency.

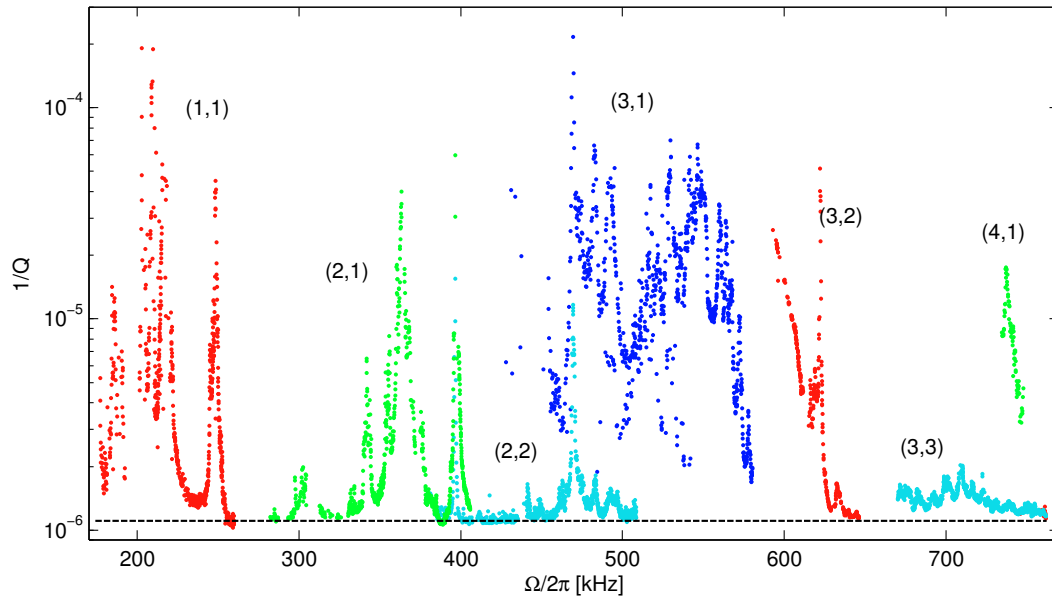


Figure 2.7: Inverse  $Q$  factors for higher membrane modes in comparison.

## 2.2. Quality factor analysis

---

$l$ [ $\mu\text{m}$ ]	250	500	1000	1500	500	500
$d$ [nm]	50	50	50	50	75	100
$S_0$ [MPa]	66.4	98.0	120	78.8	114	217
$\Delta S_0$ [MPa/mW]	0.08	0.27	0.12	0.10	0.07	0.01
$\Omega_{1,1}/2\pi$ [kHz]	428	260	144	77.7	281	387
$\Delta\Omega_{1,1}/2\pi$ [Hz/mW]	-259	-363	-68.9	-49.5	-89.6	-10.5
$Q_{\text{max}}$ [ $10^5$ ]	3.2	10	15	5.7*	10	0.37*
$a_m^2$ [ $10^{-3}$ ]	1	1.7	0.7	0.8	0.9	0.2

Table 2.2: Summary of measured low-stress SiN membrane parameters.  $Q_{\text{max}}$  refers to the maximum observed  $Q$ . Values marked by \* were limited by the available tuning range.

bers  $\Omega_{2m,2n}$ , as their mode amplitude integrates to zero over the whole membrane. This behaviour has also been observed in recent publications [89, 92]. If one looks at resonances in  $Q$  that were probed by different membrane modes, like in the frequency range of 450 – 500 kHz, one can see that the coupling to frame modes and therefore  $Q$  can change over more than one order of magnitude depending on the mode shape. Apart from coupling to frame modes, one can again see a universal maximum  $Q$  factor for all modes, indicated by the dashed line. This shows that the other losses in the system are even independent of the mode shape. This is in contrast to other experiments [89] using high-stress membranes and could be due to the different frame geometry and mounting. In contrast to [89], the frame is a relatively small resonant structure with eigenmodes at distinct frequencies.

Besides probing higher modes of the same membrane one can also investigate the general dependence of membrane parameters to their dimensions and material properties. For this purpose a series of membranes with different thickness  $d$  and sidelength  $l$  are analysed. The results are shown in table 2.2. First of all one can see that these membranes all have different tensile stress  $S_0$ . This can be explained by the production process, where the material composition of SiN can vary between different deposition runs. For membranes of same size within the same production batch, one only observes differences in frequencies on the 1% level, which correspond to stress or geometry differences on the same level. The tuning capability  $\Delta\Omega$  depends on the temperature increase on the membrane, which can depend on the heat conductivity, geometry, and absorption. The calculated optical absorption values tend to decrease with increasing stress. The measurements done in [93] show this behaviour, as a rising nitrogen content in  $\text{SiN}_x$  leads to a shift of large optical absorption towards shorter wavelength, such that the absorption for a given long wavelength should decrease. In our measurement, one cannot differentiate between an increased absorption and a decreased heat conductivity. According to [81] and [84] the heat conductivity of high-stress  $\text{Si}_3\text{N}_4$  is ten times larger, so one can assume that the temperature increase should also drop with rising nitrogen content. A look

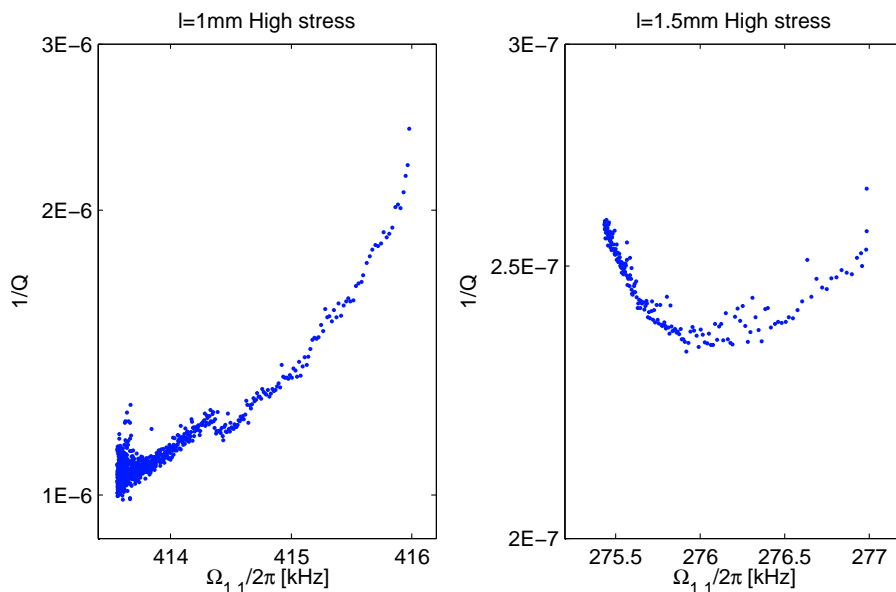


Figure 2.8: Fundamental mode quality factor tuning measurements for two high stress membranes with different side length  $l$ . The tuning was carried out by resistive heating of the frame.

at the geometries shows that the tunability decreases with increasing membrane size and thickness, which is mostly caused by the difference in absorption. A minor effect is that the temperature increase rises with membrane size according to equation 2.6. The observed  $Q_{\max}$  increases with membrane length  $l$ , which was also observed in other experiments [92], where an empirical scaling of  $Q_{\max} \propto l^2/d$  was found.

### 2.3 High-stress membranes

Besides the previously investigated low-stress membranes, high-stress stoichiometric  $\text{Si}_3\text{N}_4$  membranes exist with defined material composition and tensile stress around  $S_0 = 920$  MPa. These membranes have much lower absorption  $a_m^2$ , so the described tuning via laser heating does not work with the available power. However, the resistive heater can be used to tune via the differential thermal expansion. The results are shown in figure 2.8. As in the low-stress case, the membranes show a variation in  $Q$  over a small frequency range, pointing to the same coupling to frame modes. The  $Q$  factor of larger membranes is larger as well. While the much lower absorption limits the tunability, it is beneficial in experiments utilizing these membranes, as one can apply much higher laser powers.

In order to tune the membrane by heating with laser light a different wavelength can be used that is effectively absorbed. According to [93], blue light is absorbed more efficiently. However, a  $\lambda = 405$  nm laser diode with 200 mW was not able to

tune the membrane frequency significantly.

## 2.4 Improving membrane properties

Increasing the membrane's  $Q$  and decreasing its effective mass  $M$  can lower the requirements for ground state cooling and coherent dynamics (see chapter 1). One possibility is to decrease the membrane's coupling to the environment by engineering the clamping, the other is to change the physical properties themselves.

### 2.4.1 Conclusions for mounting

The observation of coupling to frame modes allows to manipulate the membrane's clamping losses. This can be directly done by tuning the membrane off resonant to the frame modes. However, this means heating the membrane, which is not beneficial for cooling to the quantum ground state. In practice one has to try out different membranes to find a situation where the membrane is already off resonant with the frame. To increase the probability, it is favourable to have high  $Q$  frame modes, as this narrows down the coupling regions. Before the frame modes were found, we empirically optimized the membrane mounting to only gluing down the frame on one corner. In [92] the contact area was also minimized to achieve high  $Q$  factors. The small contact area therefore appears to increase the frame modes  $Q$ .

The gaps between modes of the frame are analogous to phononic bandgap shieldings [98]. Phononic bandgap shields prevent clamping losses in the mechanical oscillator, as phonons of certain energy bands are forbidden to enter the shield and are therefore contained to the membrane inside the shielding. Phononic bandgaps have been integrated to SiN membranes recently [99, 100] and allow for a more rigid mounting of the membrane thus increasing the thermal contact, but not yet a general improvement on the maximum possible  $Q$ , as the fabricated structures were most likely limited by intrinsic losses[101].

### 2.4.2 Structuring membranes

Besides the membrane  $Q$  its effective mass  $M$  is an important figure of merit, as a reduced effective mass increases optomechanical damping (equation 1.48) and also atom-membrane coupling (equation 1.1).

Compared to a string with fundamental frequency  $\Omega_m = \pi/l\sqrt{S/\rho}$  [102], a membrane only has a  $\sqrt{2}$  higher frequency, but a  $l/2s$  larger effective mass, if  $s$  is the string's width. It seems natural to switch to a string geometry, if one is able to maintain the high  $Q$  factor and low optical absorption. To try this out, we used a focussed ion beam (FIB) to cut pieces out of a low-stress membrane. The designed structure is shown in figure 2.9a as a FEM simulation. The shape was optimized for low effective mass and fitted into the maximum FIB structuring area of  $(300 \mu\text{m})^2$ . The structuring itself turned out to be quite challenging, as the membrane rips apart from too much tensile stress during the cutting process. In addition, the membrane

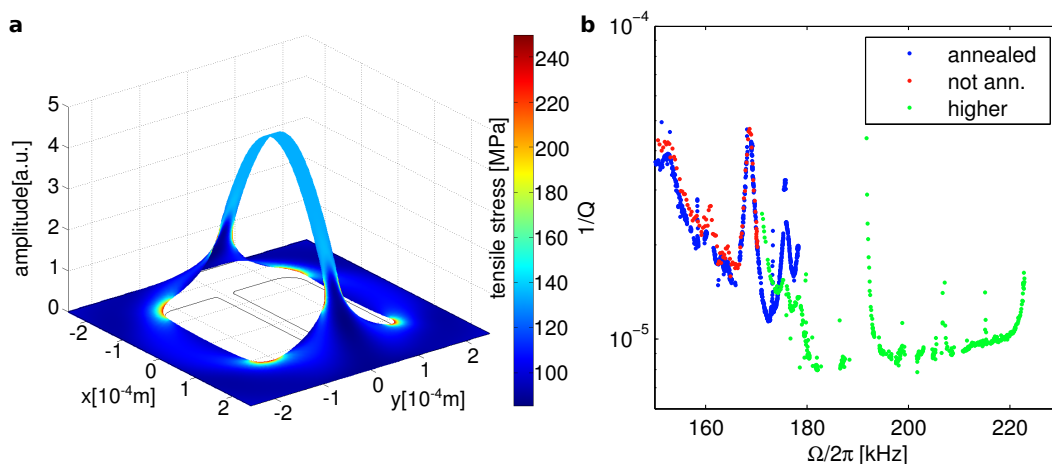


Figure 2.9: **a:** FEM simulation of the fundamental mode of a structured membrane. **b:** Frequency dependent membrane Q factor. The red curve was taken before the membrane was exposed to high heating laser powers, the blue one after. The green curve shows the first higher mode.

can charge up, as it is insulating, thus distorting the FIB pointing. To lower the stress in the process, the membrane was first perforated with small slits, before cutting the remaining parts. The resulting structure is shown in figure 2.10b. One can see a few defects in the structure, especially the SiN piece in the middle of the string, the overall shift of the structure and the ripped membrane on the right side. The shown membrane was the only one that was successfully produced. In general, the process lacks reproducibility, as most membranes got destroyed. In figure 2.9b the loss  $1/Q$  of the structured membrane is shown. The red curve shows an initial measurement. After exposing the membrane to high laser powers, the membrane frequency  $\Omega_m (P = 0)$  increases due to annealing permanently from  $\Omega_m/2\pi = 170$  kHz to 178 kHz. The annealing process is also present in unstructured membranes, but weaker. A maximum  $Q = 9 \times 10^4$  for the fundamental mode and  $Q = 12 \times 10^4$  for a higher mode is observed, an order of magnitude less compared to unstructured membranes. Given the imperfections in the structuring process this is not surprising. In addition to the lowered  $Q$ , the tunability of the membrane increased to  $\Delta\Omega_m/2\pi = 1.7$  kHz/mW. This increase can have its origin in impurities implanted by the FIB, the defects in the structure, but also purely the change in geometry. Starting from the heat equation 2.5, one can calculate the temperature distribution of a membrane string by splitting into two regions

$$\frac{\partial^2 T_1}{\partial x^2} = -\frac{Q_{\text{th}}}{\kappa_{\text{th}}} \quad 0 \leq x \leq w_L \quad (2.8)$$

$$\frac{\partial^2 T_2}{\partial x^2} = 0 \quad w < x \leq l/2 \quad (2.9)$$

with  $x = 0$  being the middle of the string,  $w$  the radius of the laser beam with constant intensity, and evaluated only to  $+l/2$  for symmetry reasons. With boundary conditions  $T_1(x = w) = T_2(x = w)$ ,  $\partial T_1/\partial x(x = w) = \partial T_2/\partial x(x = w)$ ,  $\partial T_1/\partial x(x = 0) = 0$  and  $T_2(x = l/2) = 0$  for simplicity one gets

$$T_1 = \frac{Q_{\text{th}}}{2\kappa_{\text{th}}} (-w^2 - x^2 + wl) \quad (2.10)$$

$$T_2 = \frac{Q_{\text{th}}w}{\kappa_{\text{th}}} \left( \frac{l}{2} - x \right) \quad (2.11)$$

with a maximum temperature  $T_{\text{max}} = Q_{\text{th}}w(l-w)/2\kappa_{\text{th}}$ . Using  $P_{\text{abs}} = Q_{\text{th}}2wds$  with  $s$  being the membrane string width and an assumed quadratic laser cross section with  $2w = s$ , one gets an average temperature increase relative to the frame of

$$\Delta T = \frac{P_{\text{abs}}}{4\kappa_{\text{th}}t} \frac{l}{w} \left( \frac{1}{4} - \frac{1}{3} \left( \frac{w}{l} \right)^2 \right). \quad (2.12)$$

In the limit  $w \ll l$  the temperature increase ratio between full membrane and structured string is

$$\frac{\Delta T_{\text{membrane}}}{\Delta T_{\text{string}}} = \frac{4w}{\pi l}. \quad (2.13)$$

The factor  $4/\pi$  originates from modelling the full membrane round, the factor  $w/l$  however scales as  $s/2l$  with the geometry. If the system is limited by thermal heating of the membrane, the maximum allowed power is smaller by this factor. Putting this together with the effective mass reduction by  $2s/l$  and the  $\sqrt{2}$  longer string length to get the same frequency, one ends up with a factor  $4\sqrt{2}/\pi$  reduced optomechanical damping according to equation 1.48 and sympathetic cooling (equations 1.1 with  $\Omega_a \propto P$ ). In the described limits it is therefore not favourable to switch to a string oscillator.

As an alternative improvement, we tried to increase the membrane reflectivity by adding a mirror to the membrane. In order not to increase the mass significantly, a gold mirror was used instead of a multilayer dielectric coating. The mirror was created by sputtering 40 nm of gold (plus 3.5 nm Titanium adhesion laser between AU and SiN) onto the membrane using a shadow mask that itself was made of a SiN membrane and supplied by IBM<sup>3</sup>. Two membranes were fabricated, one with a gold mirror diameter of 100  $\mu\text{m}$ , one with 20  $\mu\text{m}$ , thus increasing the mass by 100% respectively 4%. The resulting membrane is shown in figure 2.10a. The resulting membranes have a strong frequency shift of 20 kHz/mW for the small gold mirror, the larger mirror membrane was even destroyed by the incident light. In addition, the  $Q$  factor of the intact membrane was too low to be measured with the setup. The reason for that is unknown, as it has been demonstrated that aluminium coated membranes can have high  $Q$  factors [91]. However, the large frequency shift caused by absorption in the gold makes these membranes impractical to use in our experiment.

---

<sup>3</sup>Courtesy of Leo Gross, IBM research, Rüschlikon

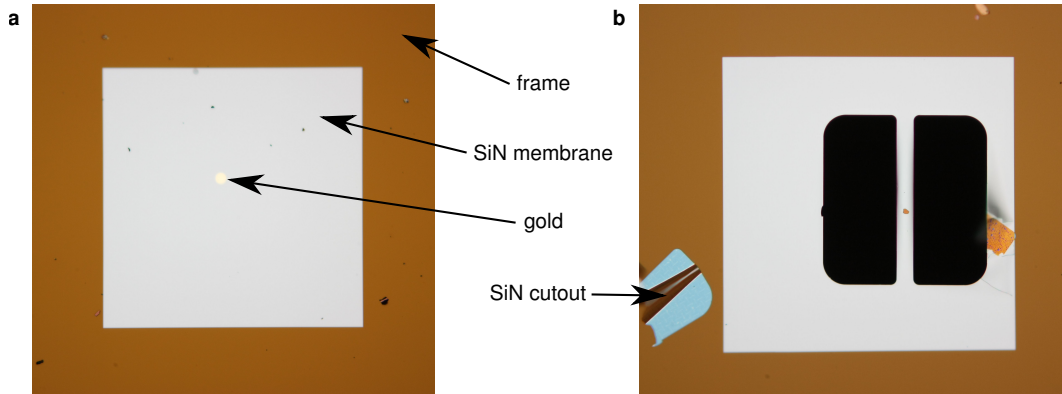


Figure 2.10: **a:** Optical microscope pictures of a membrane with a  $20\ \mu\text{m}$  diameter and  $40\ \text{nm}$  thickness gold mirror and **b:** a membrane structured using a FIB down to form a thin string. The dust particles are a result of a longer storage outside vacuum before taking the pictures.

As a conclusion, standard high-stress  $\text{Si}_3\text{N}_4$  membranes seem to be the best choice for implementation into our system.

The only question remaining is which membrane geometry to use. The empirical relation  $Q_{\text{max}} \propto l^2/d$  [92] suggests to use the thinnest membrane, but the membrane thickness dependent reflectivity  $r_m \propto d$  compensates the larger  $Q$  and lower  $M$  for  $d \ll \lambda/n$ . This condition however is not given, such that a thinner membrane is still advantageous. The membrane length is not important, as  $M \propto l^2$ , resulting in the same cooling ratio according to equation 1.1 and 1.3, given that a mode of same frequency is available. As the fundamental mode rarely has the highest  $Q$ , using a higher even symmetric mode like  $\Omega_{2,2}$  represents the optimum. In our case the low atomic vibrational frequencies in our current lattice geometry force us to use the fundamental mode of the largest  $\text{Si}_3\text{N}_4$  membrane.

## *2.4. Improving membrane properties*

---

## Chapter 3

# Ultra-cold atom apparatus

Techniques of laser cooling and trapping [69] are used to prepare ultracold atoms for our hybrid optomechanical experiment. A necessary requirement is an ultra-high vacuum chamber, in which the atoms can be isolated from the environment. Typically, a vacuum pressure  $p \leq 10^{-9}$  mbar is needed to trap atoms on the second time scale. A second requirement is to have precisely controllable laser beams and magnetic fields available for cooling and trapping. The last ingredient is a source of rubidium for loading the trap. In order to characterize the trap absorption imaging is used and the whole system is computer controlled. This chapter explains the design and setup of a new ultra-cold atom apparatus as well as its characterisation, including the optical lattice for the hybrid system. First the desired parameters and properties will be explained, then the experimental implementation. After that, a full characterization of the system will be given.

### 3.1 Design considerations

The ultracold atom apparatus used in previous experiments consisted of a glass cell with attached atom chip, which was designed to couple a BEC to an AFM cantilever on the chip [103, 14]. The magnetic fields were created using the chip and the chip surface was used to reflect laser beams of the magneto-optical trap (MOT) [69], such that the system allowed to trap atoms next to the surface and transfer them further into a magnetic trap. In subsequent experiments [15, 104] the atoms were free-space coupled via a light beam to a membrane inside another vacuum chamber, leaving the chip as an unnecessary limitation to optical access and atom number.

The new atom apparatus that was constructed as part of this thesis is therefore designed to produce large atomic clouds to optimize the coupling and provide enough optical access to support a transverse optical lattice, multiple imaging axes and large angular accessibility along the main experimental axis. The setup is versatile enough to also allow for other experiments like an atomic quantum memory for  $\lambda = 780$  nm quantum dot photons [105] with experimental configurations like in [106] or creating a BEC in an optical trap [107]. Still, we wanted to keep the overall setup simple

### 3.1. Design considerations

and compact. For maximum optical access and compactness a glass cell instead of a metal chamber is the best choice.

In order to trap many atoms a two chamber construction is chosen. Loading the trap directly from the background vapour has the disadvantage of having to increase the background vapour pressure in order to load atoms faster, which increases the background gas collision losses as well, resulting in an unchanged maximum atom number. The two chamber setup separates the loading and trapping zones, as in one chamber the rubidium atoms are gathered from gas vapour and are then sent as a cold beam to the main experiment chamber.

Two different techniques are commonly used as an atom source, either a two dimensional MOT (2D-MOT) [108] or a Zeeman slower [109]. A Zeeman slower typically consists of an oven, where a collimated hot gas beam exits towards the trap. On the way, a red detuned laser beam in combination with a varying magnetic field is used to slow down the atoms. This Zeeman slower has the advantage of producing large atomic fluxes [109] and being available for all laser coolable atoms, but is more complex and has, for rubidium, a typical length of 1 m, thus making it impractical for a small vacuum chamber. In a 2D-MOT, only two axes are laser cooled and the atoms can leave the system along the open axis. This produces a transversally cold atomic beam, that is also somewhat cooled longitudinally. The atom beam is sent through a small differential pumping tube between the chambers, that allows a large pressure difference between them and therefore long lifetimes and large loading rates. The advantage of the 2D-MOT lies in the lower complexity of the construction, as only a small chamber volume is needed and the lasers are already available. We therefore decided on the 2D-MOT.

The complete vacuum apparatus is drawn in figure 3.1. In addition to the men-

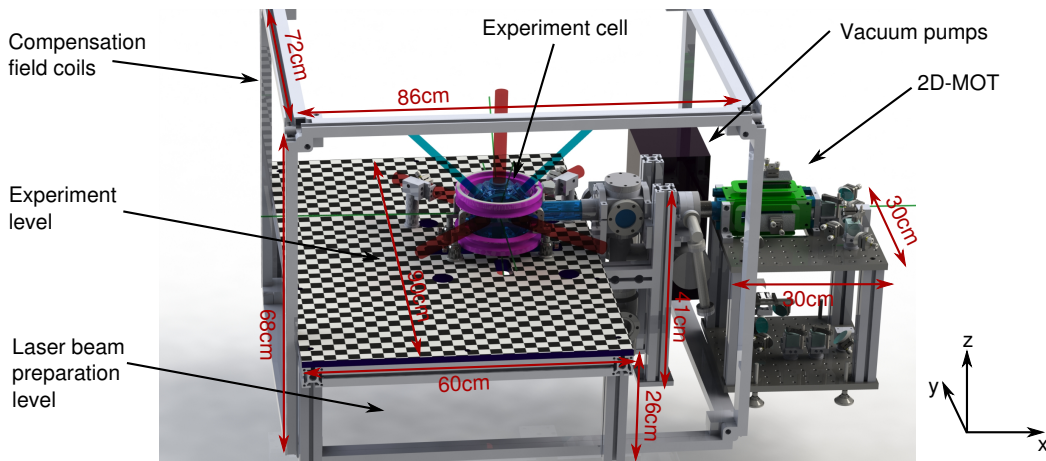


Figure 3.1: Drawing of the apparatus. The compact system for trapping rubidium atoms is a two-chamber setup with a 2D-MOT for loading the main 3D-MOT in the experiment cell. Details are given in the text.

tioned components the mounting construction and other vacuum components are shown. The big cage surrounding the experiment contains magnetic field compensation coils. The components will be described in detail in the following sections.

## 3.2 Vacuum system

In the following the two parts of the vacuum chamber will be discussed and the assembly and baking procedure will be described.

### 3.2.1 3D-MOT chamber

**Experiment cell** The primary part of the vacuum chamber is the experimental section. As already mentioned using a glass cell is advantageous for optical access, minimizing the vacuum chamber size and also for placing optics close to the trapped atoms in order to get higher imaging resolution.

For these reasons we decided on an octagonal glass cell with two big side windows and seven 45° separated smaller windows around, as pictured in figure 3.2. The cell was assembled by Precision Glassblowing<sup>1</sup> using a technique called fritting, which allows the windows to be anti-reflection (AR) coated (for 0°) on both sides. The 4-inch window supports the main coupling beam and under 45° two axes of the MOT beams (red) with a diameter up to 2 cm. The third MOT axis is vertically aligned and a transverse lattice (blue) can be implemented through the smaller 45° windows. In order to image the atomic cloud an optical path through the cell connector

<sup>1</sup><http://www.precisionglassblowing.com/>

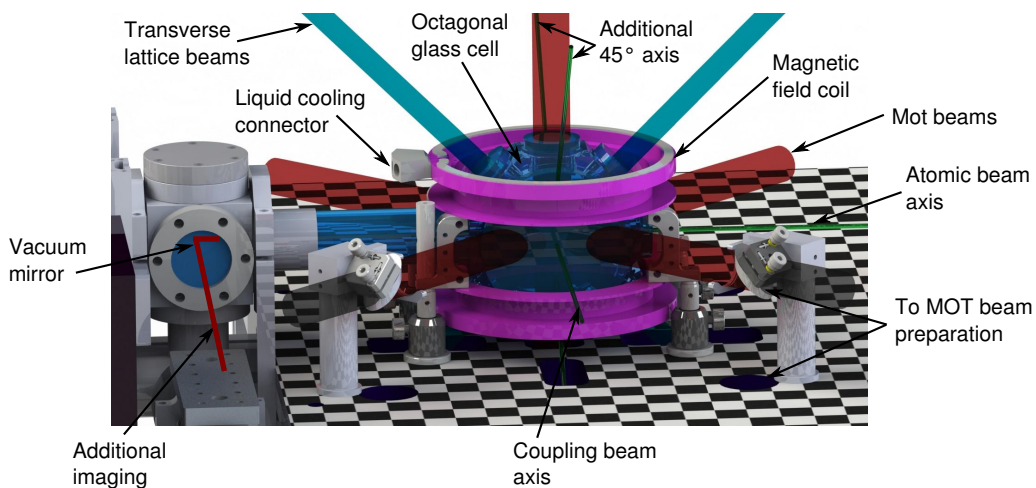


Figure 3.2: Schematics of glass cell and optical beams. Red represents 3D-MOT beams, blue transverse lattice beams. Green are additional beams as labelled. Pink is the 3D-MOT magnetic field coil support surrounding the chamber.

flange in combination with an in vacuum mirror is available. Additional optical pathways for imaging and pumping can be placed under various angles through the large windows. The robustness of the MOT operation to imperfections in the beam polarization allows the MOT beams to be on the 'bad' axes of the chamber and has the advantage of keeping the main axis available for the actual experiment. The MOT beams are prepared on a level below the glass cell in order to not require space on the experiment level breadboard. The breadboard is made insulating out of POM (Polyoxymethylen) to prevent Eddy currents, which have a 20 ms decay time in aluminium and cause problems when switching magnetic fields.

In addition to the cooling beams anti-Helmholtz coils are required for spatial confinement of the MOT atoms. The coils are described in detail in section 3.3. The required currents rise quadratically with coil dimensions, so the coils are placed as close to the vacuum chamber as possible. The resulting coil design is a compromise between optical access and power supply constraints and has an additional Helmholtz coil layer and water cooling integrated.

**Chamber construction** The rubidium atoms captured in the 2D-MOT are transferred to the main chamber along the atomic beam path depicted in figure 3.3 in a top cut view through the vacuum chamber. Starting from the octagonal glass cell the vacuum chamber consists of a main CF40 cube, which has additional viewports<sup>2</sup> on the side (top and bottom in picture) and the connector to the 2D-MOT on the right side under a small angle to be able to house the in-vacuum mirror for imaging. The in-vacuum mirror is attached to a holder using titanium screws and the 2D-MOT will be described in the following section 3.2.2. On top of the CF-40 cube a pressure gauge<sup>3</sup> is placed (not in picture), below a 4-port T-connector is placed to connect to the ion pump<sup>4</sup> behind an additional valve, a titanium sublimation pump (TSP)<sup>5</sup> below the outcoupler platform and a valve connecting to an external primary pump, that is removed after pumping down. The setup is quite compact this way, but limited in pumping speed due to the relatively thin and long pump connections. The pump parameters will be discussed in the following.

**Pressure estimate** The ultra high vacuum in the chamber is kept by an ion pump in combination with a TSP. The TSP evaporates titanium onto the surrounding chamber surface, which then acts as a getter material. This way mostly hydrogen and nitrogen gets absorbed. Noble gases and organic molecules get captured in the 40l/s ion pump in a starcell configuration, which has a much higher pumping rate for these particles. An estimate of the final pressure is hard, as a lot of the parameters and effects are unknown and have to be estimated. Especially the effect of the titanium sublimation pump as well as the outgasing of the surfaces in the

---

<sup>2</sup>Allectra, CF40, non magnetic viewport, fused silica, AR coating, 110S-QZ-IR-C40-NM

<sup>3</sup>Leybold Ionivac IE514 Extractor

<sup>4</sup>Varian/Agilent VacIon Plus 40 starcell

<sup>5</sup>Agilent Titanium Sublimation Cartridge

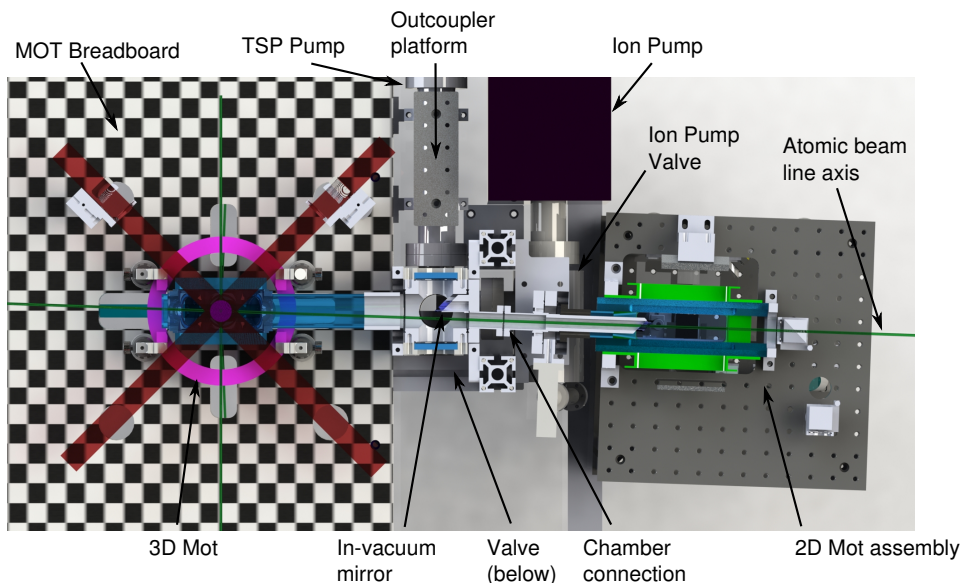


Figure 3.3: Top cut through the vacuum chamber showing the atomic beam path within the chamber and the vacuum components.

chamber are hard to predict. Empirical values from previous vacuum chambers with similar pumping capacity are  $p = 3 \times 10^{-10}$  mbar [103],  $p = 2.4 \times 10^{-10}$  mbar [110] and  $p = 5 \times 10^{-10}$  mbar [111]. The difference to these vacuum chambers is the more compact construction, leading to larger pumping rates at the experiment position, and the attached 2D-MOT chamber, leading to a leakage rate through the differential pumping tube. This leakage is assumed to be dominated by the rubidium pressure inside the 2D-MOT chamber, which is around  $p_{Rb} = 2 \times 10^{-7}$  mbar [72] at room temperature. In order to estimate the effect of this additional leak, one can calculate the conduction through the differential pumping tube as [112]

$$C_T = \frac{8r}{3l} S_0 \quad (3.1)$$

with length  $l = 8.5$  mm, radius  $r = 0.5$  mm and the material flow  $S_0 = A\bar{v}/4 = 0.06$ , l/s through the cross section  $A = \pi r^2$ . Here  $\bar{v}$  is the average particle speed, for rubidium  $\bar{v} = \sqrt{3k_B T/m} = 290$  m/s following the Maxwell-Boltzmann distribution. For these parameters a final pressure of [112]

$$p = \frac{1}{\frac{1}{S_0} + \frac{1}{C_T}} \frac{p_{Rb}}{S} \quad (3.2)$$

can be reached, where  $S = 40$  l/s is the assumed pumping speed. For the assumed values a pressure  $p = 4 \times 10^{-11}$  mbar can be reached using only the ion pump when neglecting reductions due to conduction losses through the chamber. This

### 3.2. Vacuum system

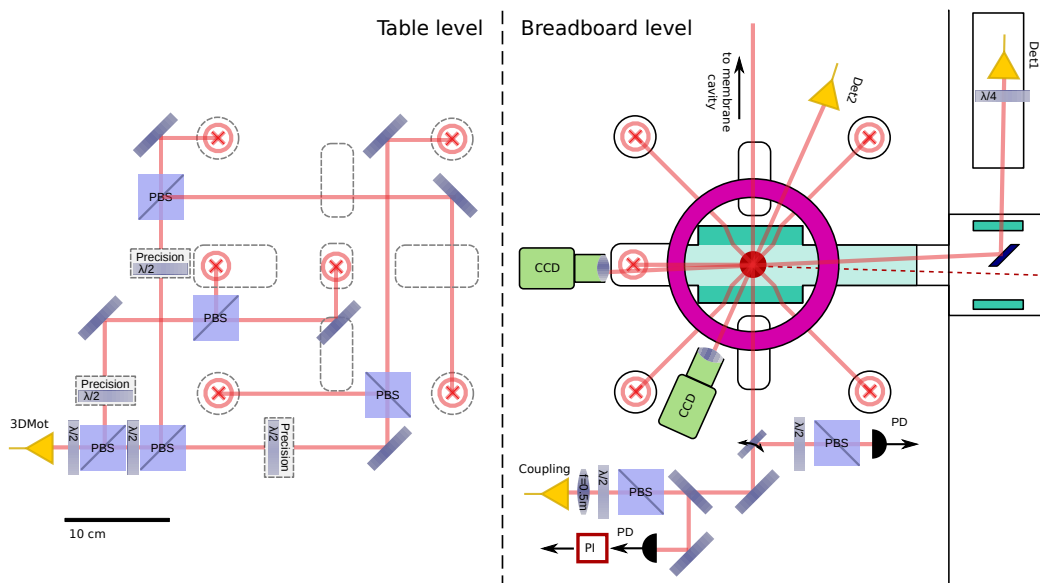


Figure 3.4: 3D-MOT chamber optics: 3D-Mot light is distributed on the table level and sent upwards. On the experiment level, two imaging systems and the membrane-atom coupling laser are situated. The vacuum chamber and breadboard cut-outs are drawn to scale.

is sufficiently small compared to the typical final pressures reached in the previous systems, such that it should not limit the final vacuum pressure. In addition it represents an upper bound, as rubidium tends to stick on vacuum chamber walls and is itself a getter material for other particles. The effect of the TSP strongly depends on the effective titanium coated surface and connection to the main chamber. It is here assumed to have a similar pumping rate as in previous systems and not further investigated.

**Optics assembly** The optical construction surrounding the 3D-Mot chamber is shown in figure 3.4. The outcoupled MOT cooling and repumping light on the lower table level has  $2w = 1.2$  cm diameter and is distributed along the cooling axis into 6 beams next to the vacuum chamber. The advantage of this method is the increased long term stability of the alignment compared to a system with each MOT beam being coupled out of a separate fiber. Especially the beam balancing between counter-propagating beams is fixed using a  $\lambda/2$  waveplate in a precision mount. Realignment is only required in the fiber couplings. In addition to the 3D-MOT beams, imaging beams and cameras along two axes are installed and the membrane-atom coupling beam assembly is also shown in the drawing.

### 3.2.2 2D-MOT

The design of the 2D-MOT is inspired by previous work in other groups [113, 114]. The 2D-MOT assembly is schematically drawn in figure 3.5. It consists of a rectangular cell of four inch length and a solid rubidium reservoir connected via a valve. The atoms are captured from background vapour and the resulting beam has small lateral dimensions, allowing it to be sent through the 1 mm diameter differential pumping tube between the two chambers. The differential pumping tube consists of a dielectric mirror mounted under  $45^\circ$  with a hole drilled using an ultrasonic drill. This way, a laser beam counter-propagating to the atomic beam can be sent in from the side, allowing for a  $2D^+$ MOT [108] configuration, that offers larger atomic fluxes and lower velocities. The 2D-MOT chamber is, in contrast to many other experiments, constructed without additional pumps and only pumped down via the small connection to the main chamber, which reduces its size significantly. In order to align the atomic beam to the differential pumping tube the 2D-MOT optics and quadrupole magnetic field coils are mounted independently of the vacuum chamber on an adjustable platform. The optics can therefore be first aligned to the magnetic fields and thus create an optimal atomic beam. Then, the whole assembly can be moved independent of the vacuum chamber to align the atomic beam through the chamber connection. This way, the design also avoids having to use a bellow to tilt the chamber.

**Atom source** The rubidium reservoir is a glass ampoule filled with 1 g Rb of natural isotope abundance. The alternative would have been dispensers, that allow to control the rubidium pressure. However, the gas pressure of rubidium is  $P_{\text{Rb}} = 2 \times 10^{-7}$  mbar [72] at room temperature, close to the optimum for a high atomic flux [108]. A control of the pressure is therefore not needed. The disadvantage of a dispenser is the lower lifetime and the additional complexity due to vacuum feed through and current source, which is why we decided against it. The rubidium ampoule rests inside a flexible tube, such that it can be broken once the chamber has reached the final pressure.

**Differential pumping tube** The dimensions of the differential pumping tube (length  $l = 8.5$  mm, radius  $r = 0.5$  mm) lead to a conduction of  $C_T = 0.0141$  l/s for air with  $\bar{v} = 470$  m/s [112], see equation 3.1. The pumping time constant therefore is  $\tau = V/C_T = 7$  s for an estimated chamber volume of  $V = 0.1$  l. For the final pressure being dominated by rubidium, the wall leakage rate has to be  $Q A \ll C_t p_{\text{Rb}} = 3 \times 10^{-9}$  mbar l/s. For a surface area of  $A = 500$  cm<sup>2</sup> a leakage  $Q \ll 6 \times 10^{-12}$  mbar l/s cm<sup>2</sup> has to be achieved, which is lower than typical values [112]. However, in practice the rubidium itself provides pumping [115] and no limitations due to background pressure have been observed.

Another design factor is the alignability of the atomic beam. For an assumed divergence of  $\Theta = 40$  mrad [108], a maximum alignment angle of  $\Theta_{\text{max}} = 2r/l - \Theta/2 = 100$  mrad =  $6.5^\circ$  can be achieved assuming negligible initial beam diameter.

### 3.2. Vacuum system

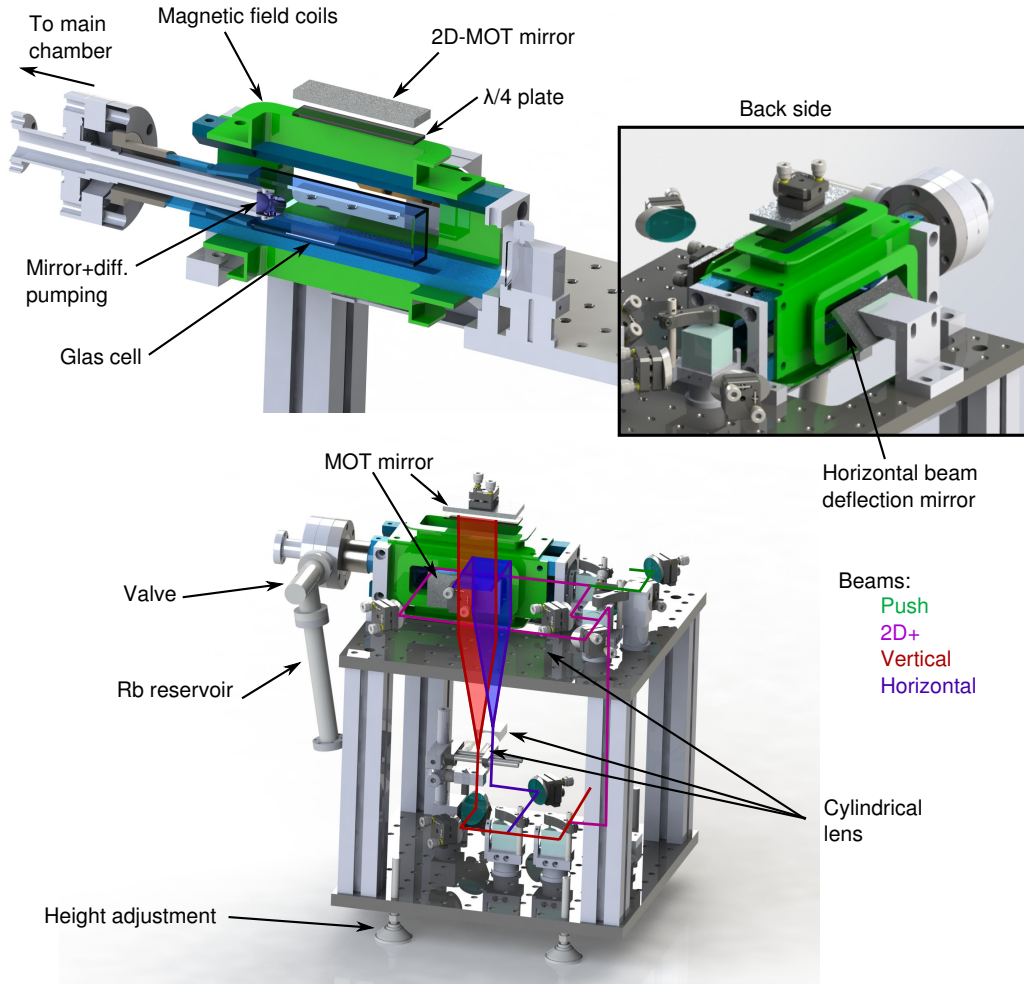


Figure 3.5: 2D-MOT schematics: The lasers and magnetic fields are created on an platform surrounding the glass cell without a physical connection. This way, the atomic beam can be aligned relative to the vacuum chamber. The elliptical beams are generated using cylindrical lenses and reflected after passing through the glass cell. With additional beams, a 2D<sup>+</sup>MOT configuration can be achieved.

**Optical construction** The 2D-MOT laser beams are distributed from a single optical fiber that provides cooling and repumping light, see figure 3.5. The 2D-MOT is operated with retro-reflecting beams, such that only two beam paths are required. The main beam of 2 cm diameter is therefore split into two paths on the lower level of the platform and then send circularly polarized and stretched by a cylindrical lens pair to 2 cm  $\times$  6 cm upwards. The vertical beam is directly sent through the cell, and reflected by a  $\lambda/4$  and gold mirror assembly, while the horizontal beam is first deflected by another gold mirror. The gold mirrors ensure the polarization conservation. In addition a small part of the optical power can be split off to provide counter-propagating beams for a 2D+MOT. A separate push beam can also be deployed.

### 3.2.3 Assembly and baking

The assembly of vacuum chambers requires a proper cleaning and assembly as well as baking the chamber in order to achieve low vacuum pressures.

**Cleaning and assembly** In order to include as little residual particles, especially organic compounds, into the vacuum chamber, all standard vacuum parts are cleaned in an ultrasonic bath using soap, water, acetone and iso-propanol in that order. The more fragile valves, pressure gauge and TSP are only wiped clean with acetone and iso-propanol. The glass cells, ion pump and viewports are just cleaned at the flange. The in-vacuum mirror including the differential pumping tube was baked at 200°C before assembly. The assembly is carried out under a flow box to minimize dust particles. The main chamber is first assembled without the 2D-MOT and 3D-MOT cells, which are added after the chamber was placed at the final position.

**Pumping and vacuum baking** The initial pumping down is carried out using a turbo pump in combination with an oil free scroll pump<sup>6</sup>. The ion pump is then added and a pressure of  $p = 5 \times 10^{-8}$  mbar is achieved when closing the turbo pump connection. The baking is carried out using multiple independently controllable heating wires to ensure a homogeneous temperature distribution. The glass cells and viewports are protected by a surrounding cage construction or additional aluminium plates to prevent temperature gradients in the glass, before adding heating wires and wrapping the chamber in aluminium foil. The apparatus is heated up to about 200°C (glass cells 190°C) over a day and kept on this temperature for 2 weeks. Before cooling down again, the TSP is initialized by several deposition cycles in order to clean the filaments. The final pressure reached, as estimated later from the MOT lifetime [116], is  $p \approx 5 \times 10^{-9}$  mbar, see section 3.7. However, this value might not be very reliable. The built-in sensor did also not work correctly, as it showed a slowly rising pressure above  $p = 10^{-9}$  mbar after falling below  $p = 5 \times 10^{-10}$  mbar while cooling down the system. We assume this is caused by a charge up of the

---

<sup>6</sup>Agilent TPS-compact TV81M

in-vacuum dielectric mirror close to the pressure sensor, as the behaviour could be reproduced after another baking cycle. If the sensor was working correctly, it would hint to a leak opening up in the last phase of cooling down to room temperature. In comparison to the previous built chambers, the pressure would then be higher higher. However, for all practical purposes the lifetime of the traps is the important parameter. It will be discussed in section 3.7 and turns out to be comparable to previous vacuum systems.

## 3.3 Magnetic fields

In order to cool and control ultracold atomic ensembles, proper control over magnetic fields is required. The trapping in a MOT relies on a field gradient with the atoms accumulating at zero field. Apart from cooling, magnetic fields are required to eliminate offset fields, set quantization axes and shift atomic levels via the Zeeman effect [117].

In our system, as shown in figure 3.1, a pair of circular coils close to anti-Helmholtz configuration create the MOT magnetic field and are placed horizontally around the glass cell (purple). The 2D-MOT requires only a gradient in two dimensions, that is created by two pairs of rectangular coils surrounding the 2D-MOT cell (green). The compensation of offset fields and creation of quantization axis is done using a large cage surrounding the whole apparatus. Three pairs of Helmholtz coils can create a homogeneous magnetic field at the 3D-MOT in arbitrary direction. In addition, a pair of coils in Helmholtz configuration is integrated into the 3D-MOT coils and able to create stronger fields along the Z axis.

In the following the details of these coils will be discussed and their properties analysed.

### 3.3.1 Coil parameters

The field calculations are carried out using the Biot-Savart law [118]

$$\mathbf{B}(\mathbf{r}) = \frac{\mu_0}{4\pi} \int_c \frac{I d\mathbf{l} \times \mathbf{r}}{|\mathbf{r}|^3} \quad (3.3)$$

and the simplification of a single winding with negligible wire diameter. This approximation is only valid if  $\sqrt{A} \ll r, d$  with total wire cross section  $A$ , coil radius  $r$  (or side length  $a$  and  $b$  in case of rectangular coils) and coil distance  $d$ . The calculated value underestimate the real field as the coil magnetic field has a  $1/r$  and  $1/d$  dependence in anti-Helmholtz configuration and the used geometry represents the wire cross section center.

The wire resistance can be calculated using

$$R = \frac{4\rho l}{\varnothing^2 \pi} \quad (3.4)$$

Coil	l x w [cm]	d [cm]	N	$\varnothing$ [mm]	$I_d$ [A]	R/coil [ $\Omega$ ]	$P(I_d)$ [W]
$C_x$	64x64	83	41	1.8	5	0.70	17.5
$C_y$	83x64	68	49	1.6	3	1.21	10.9
$C_z$	79x64	64	45	1.6	3	1.09	9.8
$C_{2D}$	11.45x4.45	7.8	112	0.9	2.5	0.96	6
$C_{3D}$	$\varnothing = 15$	7	65	1.5	12	0.30	43.2
$C_{3D-H}$	$\varnothing = 17$	7	20	1.3	10	0.10	10

Table 3.1: single Coil paramters, coils:  $C_{x,y,z}$  compensation coils,  $C_{2D,3D,3D-H}$  MOT field coils and additional Helmholtz coil on 3D-MOT, design current  $I_d$ .

with wire length  $l$ , wire diameter  $\varnothing$  and resistivity  $\rho = 1.7 \times 10^{-8} \Omega/\text{m}$  [119] for copper.

The coil inductance can be calculated as [120]

$$L_{\text{circ}} = N^2 r^2 \mu_0 \mu_r \left[ \ln \left( \frac{16r}{\varnothing} \right) - 2 \right] \quad (3.5)$$

$$L_{\text{rect}} = N^2 \frac{\mu_0 \mu_r}{\pi} \left[ -2(w+h) + 2\sqrt{h^2+w^2} - h \ln \left( \frac{h+\sqrt{h^2+w^2}}{w} \right) - w \ln \left( \frac{w+\sqrt{h^2+w^2}}{h} \right) + h \ln \left( \frac{4h}{\varnothing} \right) + w \ln \left( \frac{4w}{\varnothing} \right) \right] \quad (3.6)$$

for circular and rectangular mono layer coils with  $N$  windings, radius  $r$ , width and height  $w, h$  and wire diameter  $\varnothing$ .

Using these formulas, the coils were optimized for minimum size or optimal fitting for a given current source. In case of the compensation coils, minimizing the inductance was also a goal, as the coils have to be switched on a ms time-scale during the experiment and are also supposed to be used for active field stabilization. The parameters of the coils are listed in table 3.1 and discussed in the following. The operational data is shown in table 3.2.

### 3.3.2 3D-MOT coil

The 3D-MOT coils were dimensioned such that most of the optical access was preserved, see figure 3.2. The wiring consists of two separate coils for 3D-MOT  $C_{3D}$  and additional fields in z direction  $C_{3D-H}$ , see table 3.1 and 3.2. The desired field gradients of up to  $\approx 15 \text{ G/cm}$  [114, 116] require a relatively large amount of power consumption  $P$ , such that a water cooling circuit is included at the far side of each

<sup>7</sup>EA-PS 2016-050, 16V,5A

<sup>8</sup>Delta Elektronika SM 15-100

<sup>9</sup>FUG 15A 20V

### 3.3. Magnetic fields

coil pair	B/I, $\nabla B/I$ [G/A],[G/A cm]		R [ $\Omega$ ]		L [mH]		$B_0$ [G]	$T$ [ms]	source
	calc.	meas.	calc.	meas.	calc.	meas.			
$C_x$	0.40	0.406	1.40	1.48	4.4	6.71	-0.32	1.1	i-source 5A
$C_y$	0.67	0.69	2.42	2.56	7.5	11.75	-0.61	1.5	i-source 3A
$C_z$	0.66	0.66	2.18	2.26	6.1	8.37	-0.20	2.2	i-source 3A
$C_{2D}$	8	8.71/ 8.57	3.84	3.73	10.8	5.19	-	-	EA <sup>7</sup>
$C_{3D}$	0.63/ 1.25	0.66/ 1.4	0.6		3.7	1.65	-	-	Delta <sup>8</sup>
$C_{3D-H}$	2.33	2.61	0.2	0.35	0.4	0.29	-	0.02	FUG <sup>9</sup>

Table 3.2: Coil performance: The multiple entries in magnetic field relay to different axes of the coil, the difference in resistance between coils of a pair is  $< 1\%$ , the inductance is measured at 120 Hz. The large deviations from theory for the inductance originate in the interaction of the coils, leading either to a larger (Helmholtz) or lower (Anti-Helmholtz) value.  $B_0$  is the offset magnetic field at the trap position, the total field is  $|B_0| = 0.72$  G. Rise time  $T$  (10%-90%) is for switching  $0 \rightarrow -1G$ ,  $C_y$  field was confirmed using spectroscopy in addition to the direct measurement. The current sources are described in [103, 121]

coil. The cooling unit is a chiller<sup>10</sup> which is cooled itself using the lab cooling water supply. With  $I = 15$  A, the coil stabilizes  $2^\circ\text{C}$  above the cooling water temperature and a temperature difference of  $1^\circ\text{C}$  across the coil is measured. The coil frame is made of aluminium and has a gap between the water cooling connectors, that is filled with insulating glue and ensures that no Eddy currents [118] are induced during a fast switching operation.

The switch-off is done via short-circuiting the coil over a 200 V Zener diode [122] within  $80 \mu\text{s}$  (90%-10%), while the turning-on typically takes 20 ms and is a function of the maximum supply voltage. The ratio of the measured  $z$  and  $r$  (in  $x-y$  plane) field gradients is not exactly 2 like expected, which could be caused by an off-axis measurement. The  $r$  field gradient was taken as the reference.

#### 3.3.3 2D-MOT coil

The 2D-MOT coils  $C_{2D}$  were constructed such that they are four identical elongated coils in quadrupole configuration and leave optical access for the complete 4x1 inch glass cell inside the loop. The typical larger gradients in 2D-MOTs [108, 114] lead to more windings, but the smaller form factor reduces the total power consumption in the optimized configuration, that can be operated with 10V. The coils are operated with a standard linear power supply and stay always on, as the 2D-MOT is directly

<sup>10</sup>ThermoCube 10-400L-3G20-2-EF-DC-VD-AR

controlled via switching the cooling light. At the design current, the coils heat up to about 40° C with a time constant of 30 min (10%-90%) and a 5% increase in resistance is observed. The larger than calculated gradient can be explained by the approximation in the calculation and the asymmetry between the axis is probably due to an off axis measurement.

### 3.3.4 Compensation fields

The coil cage surrounding the whole experiment with the center being at the atom position consists of 3 pairs of Helmholtz coils  $C_{x,y,z}$ , one for each dimension, see figure 3.1. The construction is made of U-shaped aluminium profiles with one insulating corner per coil, thus preventing currents in the frame. The coils are connected to a cube, where the insulating corners are joined in two diametric cube corners. This way, currents can only flow along one path, which is not aligned with a field axis and not relevant in practice. The cage is designed to compensate magnetic offset fields and define a quantization axis for imaging light. In addition, for other experiments involving atomic quantum memories, it is important to reduce field fluctuations in order to increase the storage time. Therefore, an active stabilization can be integrated, whose bandwidth (BW) has to be larger than the strong 150 Hz field noise in the lab. In order to be able to quickly take absorption images after trap switch-off, a typical switching time of 1 ms is desired, which roughly corresponds to the stabilization requirement  $BW \gg 150$  Hz. The coil's windings and resistance were optimized to be able to provide a  $\pm 2$  G field with the low noise 'i-source' [121] current sources. For minimal inductance the maximum available current is used in order to reduce the windings. The resulting coils have 1 G switching times of 1 – 2 ms, see table 3.2. In order to limit the maximum backwards voltage during switching, a pair of 10 V Zener diodes is integrated in each coil pair.

On top of the compensation coils another small coil was installed in case the bandwidth of the main coils is insufficient. These coils have  $N = 7$  windings and  $\varnothing = 0.5$  mm wire diameter resulting in  $R = 3(3.4) \Omega$  for the  $y,z(x)$  axis, field  $B/I = 0.1(0.07)$  G/A and inductance  $L = 0.32(0.36)$  mH, such that they have a  $L/R = 0.1$  ms switching time as an upper bound.

The magnetic offset field in the experiment was measured using Hanle spectroscopy [123] at the atomic cloud position. Residual gradients caused by the ion pump are  $< 0.08$  G/cm estimated from Hanle spectroscopy of a displaced cloud.

**Field stabilization** Using a 3-axis flux gate sensor<sup>11</sup> with 9 kHz bandwidth and PID controllers on all spatial axis, one can actively suppress magnetic field fluctuations. This extends, for example, the lifetime of single photons stored in the atomic cloud [124]. The performance is shown in figure 3.6, where the fluctuating field components are shown with and without stabilization for the  $y$  axis. Since there was only own one sensor available, the data had to be taken directly from the

---

<sup>11</sup>Bartington Mag-03MCTP

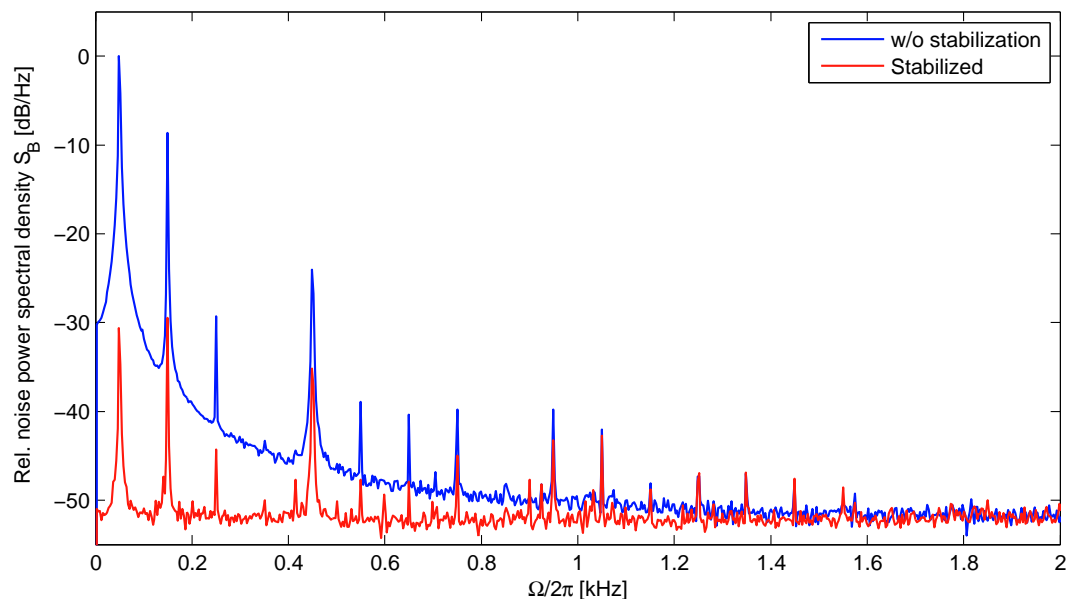


Figure 3.6: Active stabilization of the magnetic field fluctuations along the  $y$  axis. The plot shows the magnetic field noise power spectral density relative to the noise without stabilization. The unstabilized noise adds up to  $\Delta B_{\text{rms}} = 2.2 \text{ mG}$ .

sensor inside the feedback loop, so the data might overestimate the performance. The measurement floor is given by the oscilloscopes fast Fourier transform (FFT) performance. Without feedback, a rms noise of  $\Delta B_{\text{rms}} = 2.2 \text{ mG}$  is measured, with feedback  $\Delta B_{\text{rms}} = 0.45 \text{ mG}$ , which might be limited by measurement noise at higher frequency in the oscilloscope.

### 3.4 Laser system

The laser system for creating and controlling ultra-cold atoms is based on a previous one [103] and modified for supporting a 2D-MOT. The system is depicted in figure 3.8. It consists of two homebuilt diode lasers in Littrow configuration [125] with frequencies around the  $D_2$  line of  $^{87}\text{Rb}$ , one repumper for the  $F = 1 \leftrightarrow F'$  transitions, one cooling and imaging laser for the  $F = 2 \leftrightarrow F'$  transitions. The lasers are stabilized via saturated absorption spectroscopy [117] using a radio-frequency-modulation-locking (rf-lock) technique [126] at the strongest crossover transitions, see figure 3.7.

The cooling laser ('Master') is sent through an acousto optical modulator (AOM<sup>12</sup>) in double-pass configuration for frequency tuning without a change in beam point-

<sup>12</sup>Crystal Technologies

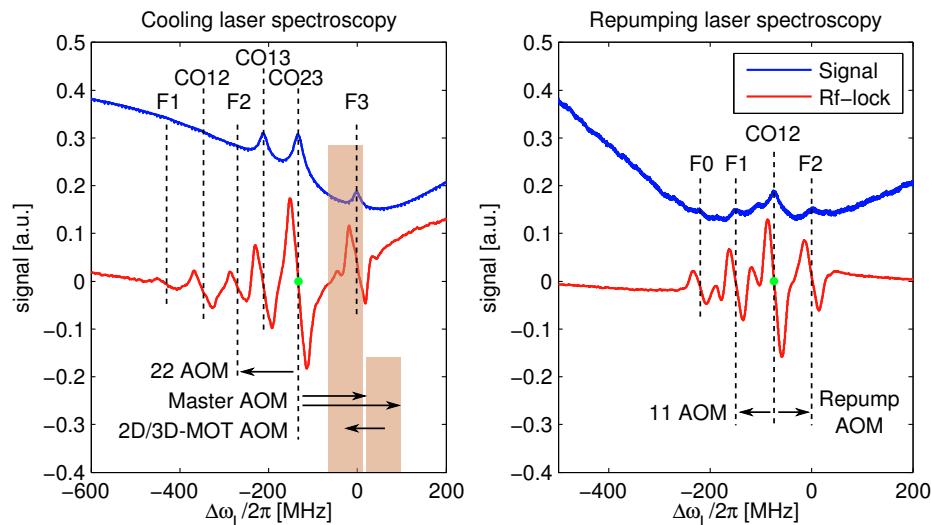


Figure 3.7: Saturated absorption spectroscopy signal plus rf-lock error signal and illustration of generated laser frequencies for cooling and repumper laser. The Master-AOM and 22-AOM are in double pass configuration, in the first case in order to realize a large tuning range, as displayed by the boxes. The lock points are marked by the green dots. The marked states are transitions to the excited state hyperfine levels  $F' = 0 \dots 3$  and crossover transitions CO in between.

ing, before it is seeding an amplifier chip ('Slave'), that is itself seeding a tapered amplifier (TA). The amplification step in between is required to provide the power necessary for seeding a TA. The laser is then split up for 3D-MOT, 2D-MOT and imaging, sent through switching AOMs and fed into optical fibers. In total it provides a cooling light power of 232 mW after the fiber and is tunable in a range of  $-11\Gamma$  to  $+2\Gamma$  from the  $F = 2 \leftrightarrow F' = 3$  transition of the  $^{87}\text{Rb}$  D2 line in units of natural linewidth  $\Gamma = 2\pi * 6.1$  MHz [72]. The switching time is only limited by the AOM, which makes it faster than other methods involving an offset lock.

The repumping laser is only shifted and switched via one AOM to the  $F' = 1 \leftrightarrow F' = 2$  transition and provides up to 8.4 mW of fiber coupled power, depending on the distribution between 2D-MOT, 3D-MOT, separate repumper fiber and 1-1 pumping beam. The additional repumper fiber can be used to create a dark-spot MOT via a central hole in the repumping beam [69], which allows a larger atomic density.

A part of the master laser is split off and shifted via a another double-pass AOM to the  $F = 2 \leftrightarrow F' = 2$  transition for optical pumping, a part of the repumper laser is transformed to  $F = 1 \leftrightarrow F' = 1$  pumping light. About 2.5 mW for the 2-2 and 0.1 mW for the 1-1 are coupled into both detection fibers.

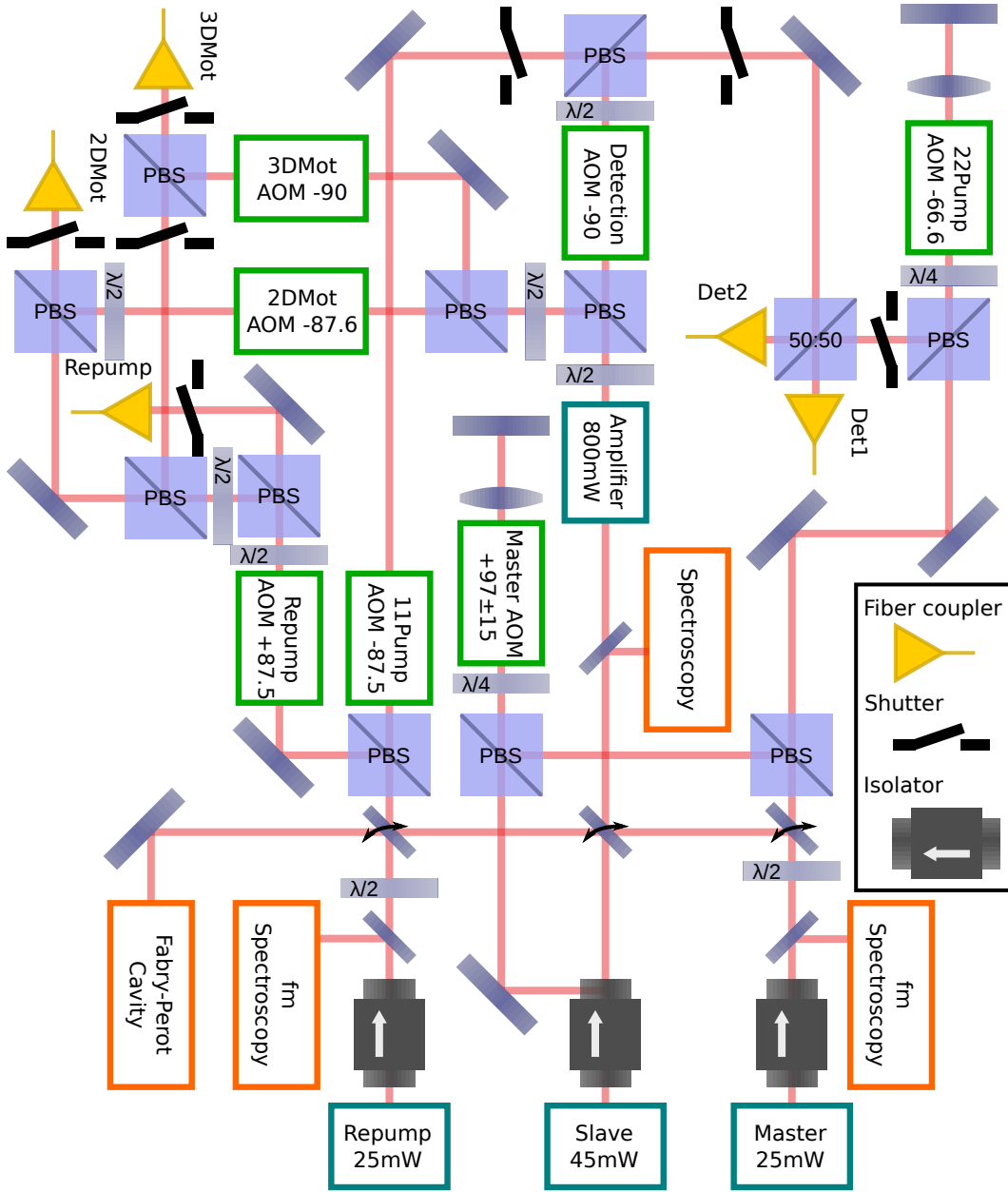


Figure 3.8: Schematics of laser system: A detailed description is given in the text. All lasers are stabilized by a saturated absorption spectroscopy, frequency shifted, switched by AOMs and distributed into fibers. The Fabry-Perot cavity can be used to check single mode laser operation. The stated laser and amplifier powers are typical values. Labels: Det1/2: imaging fibers, PBS: Polarizing beam splitter,  $\lambda/x$ : retardation wave plate. AOM frequency values are given in MHz.

In addition to the AOM switches, a shutter<sup>13</sup> is inserted into each beam in order to be able to completely block every laser component independently (except for the 1-1 pumping beam, which is right now dependent on the imaging shutter). In the optimized configuration of the cold atom setup, the 2D-MOT fiber carries 180 mW cooling plus 5.6 mW repumping light, while the 3D-MOT fiber carries 52 mW cooling plus 1.2 mW repumping light.

### 3.5 Imaging system

In order to characterize the atomic cloud an absorption imaging system [127] is built along two axis of the experiment. An image of the atoms is taken by sending the imaging light through the atomic cloud onto a camera, where the atoms cast a shadow by scattering the imaging light. The atoms scatter light from the circular polarized laser beam on the  $F = 2, m_F = 2 \leftrightarrow F' = 3, m_F = 3$  cycling transition, that is defined by a 1 G magnetic field along the imaging axis. The MOT repumping light is always present, such that all atoms are in  $F = 2$  at the beginning of the imaging process. The camera optics consist of a single achromatic lens with  $f = 40$  mm focal length, that projects the atomic cloud onto the the camera sensor. There is one camera<sup>14</sup> perpendicular to the main optical axis in the horizontal plane and one<sup>15</sup> under an angle of  $22^\circ$  to the axis, also in the horizontal plane, see figure 3.4. Table 3.3 shows the properties of these cameras. The system parameters are chosen such that a large atomic cloud can be imaged. The light absorption can be calculated using the Beer-Lambert law [127].

$$\frac{dI}{I} = -n_a(z) \sigma(I) dz \quad (3.7)$$

where a fraction of the light  $dI/I$  is absorbed in a thin slice  $dz$  by a medium with photon scattering cross section  $\sigma(I)$  and atomic volume density  $n_a(z)$ . The atomic column density can be related to the absorbed intensity using

$$\frac{dN}{dA} = \int n_a(z) dz = - \int_{I_0}^{I_1} \frac{1}{I\sigma(I)} dI. \quad (3.8)$$

The light scattering on the cycling transition can be modelled as a two level system with scattering cross section [69]

$$\sigma(I) = \frac{\sigma_0}{1 + \frac{4\Delta_{LA}^2}{\Gamma^2} + I/I_s} \quad (3.9)$$

with resonant crosssection  $\sigma_0 = 3\lambda^2/2\pi$ , laser detuning from resonance  $\Delta_{LA} = \omega_L - \omega_0$  and  $I_s = \hbar\omega\Gamma/2\sigma_0 = 1.67 \text{ mW/cm}^2$  being the saturation intensity [72]. Integrating

---

<sup>13</sup>Stanford Research Systems SR475

<sup>14</sup>AVT Guppy Pro F-031B

<sup>15</sup>AVT Manta G-145B MOD RCG

equation 3.8 gives

$$\frac{dN}{dA} = \frac{1}{\sigma_0} \left[ \left( 1 + \frac{4\Delta_{LA}^2}{\Gamma^2} \right) \ln \left( \frac{I_0}{I_1} \right) + \frac{I_0 - I_1}{I_s} \right]. \quad (3.10)$$

In order to determine  $I_0$  a second image is taken after the atoms have left the imaging region. An additional dark image without any imaging light can be taken to compensate for residual room light.

A laser detuning  $\Delta_{LA} \neq 0$  can be favourable in a case where the resonant optical density  $OD = \ln(I_0/I_1) \gg 1$  so that the light intensity reaching the camera is very small. In this case, residual light and detector noise have a strong effect. When imaging large and dense clouds, the scattered photons can also significantly contribute to the residual light. Therefore an  $OD \leq 1$  is chosen for quantitative measurements, such that the minimum incident light on the detector is far above the contributions from scattered and residual light. Another error source is that the atomic ensemble is not spin-polarized at the beginning of the imaging process. In this case, the atomic scattering cross section is smaller than  $\sigma_0$  on the cycling transition. A few photons ( $\approx 5$ ) [128] have to be scattered to pump an atom into the cycling transition. The number of these scattering events has to be small compared to the total number of scattered photons  $n_{sc} = Rt = \sigma(I)It\Gamma/2I_s$  during imaging time  $t$ , which can lead to a large number of photons being required for the imaging process. The amount of detectable photons per camera pixel  $n_{ph} = I A QEt/\hbar\omega_L$  with the image area per pixel  $A = A_{px}/M^2$ , pixel area  $A_{px}$ , magnification  $M$  and camera quantum efficiency QE can therefore exceed the well depth of the camera. The ratio of the total amount of detected photons per pixel and the scattered photons per atom is

$$\frac{n_{ph}}{n_{sc}} = \frac{A \text{QE}}{\sigma_0} \left( \frac{I}{I_s} + 1 + \frac{4\Delta_{LA}^2}{\Gamma^2} \right). \quad (3.11)$$

This ratio can be even larger at high OD, as the atoms on the far side of the cloud see a reduced imaging intensity  $I$ . For our parameters the requirement  $n_{sc} \gg 5$  leads to a limitation by the camera's well capacity. Therefore we artificially lower the quantum efficiency by inserting filters in front of the camera until the detected atom number reaches a maximum, indicating that the atoms are mainly scattering on the cycling transition with maximum cross section  $\sigma_0$ . If, on the other hand, the total number of scattered photons is too large, the transferred momentum to the atoms leads to a Doppler shift, that distorts the resonance shape and leads to an incorrect atom number, especially in detuned imaging. To verify the correct operation in detuned imaging, the detected atom number is measured without a correction for  $\Delta_{LA}$  as a function of detection laser detuning  $\Delta_{LA}$  and fitted to a Lorentzian, whose width has to reproduce the natural rubidium linewidth  $\Gamma$ .

The camera's dynamic range, signal-noise-ratio (S/N) and gain in table 3.3 are measured by analysing the variance of 100 images of a Gaussian beam with maximum pixel values close to the camera saturation. The dynamic range is then the ratio of maximum pixel value  $N_{px}^{\max}$  to the signal/noise=1 value. The maximum

camera	Manta	Guppy
angle to main axis	90°	22°
pixels	1388 × 1038	656 × 492
pixel area $A_{\text{px}}$	6.45 × 6.45 $\mu\text{m}^2$	5.6 × 5.6 $\mu\text{m}^2$
quantum efficiency $QE$ @ 780 nm	0.17	0.30
additional attenuation	×0.17	×0.17
well capacity	17000 $e^-$	16000 $e^-$
dynamic range	1 : 2000	1 : 1100
S/N max.	150	100
gain @ zero gain setting	3.7/ $e^-$	4.1/ $e^-$
magnification $M$	0.4146	0.3726
field of view	21.6 × 16.1 mm	9.9 × 7.4 mm
resolution	14 $\mu\text{m}$	14 $\mu\text{m}$
peak imaging intensity	0.28 $I_s$	0.14 $I_s$
imaging pulse length	125 $\mu\text{s}$	100 $\mu\text{s}$
scattered photons for $\Delta_{\text{LA}} = 0$	515	230

Table 3.3: Properties of the two imaging cameras.

signal/noise is determined close to camera saturation and the gain  $g$  can be calculated as  $\text{var}(N_{\text{px}}) = g\overline{N_{\text{px}}} + C$  with pixel value  $N_{\text{px}}$  and noise offset  $C$  in the regime of shot noise limitation. This sets the well capacity to  $N_{\text{px}}^{\text{max}}/g$ . The quantum efficiency is calculated by shining a calibrated amount of photons  $n_{\text{ph}}$  onto the sensor and comparing to the summed up values of all pixels  $\sum N_{\text{px}} = g n_{\text{ph}} QE$ . The spatial resolution is measured using the 1951 USAF resolution test chart. The magnification is determined from a free fall experiment of a molasses cooled atomic cloud and checked using the resolution test chart.

In order to quantify the imaging performance, the standard deviation in atom number and fitted cloud width is measured 50 times for a small molasses cooled atomic cloud with  $N = 3 \times 10^8$  atoms after  $t_{\text{TOF}} = 5$  ms (time of flight, without any optical and magnetic fields). The atom number difference is 5% between the cameras with at standard deviation for the Manta (Guppy) camera of  $\sigma = 1.5\%(2.5\%)$  and a difference in fit width of 1.4% with standard deviations of  $\sigma = 0.75\%(0.51\%)$  for the Manta (Guppy) camera. The error in the atom number includes also the variation for different realizations of the cloud, so it is also a measure for the overall reproducibility of the experiment.

### 3.6 Experiment control

The magnetic fields, lasers and other devices are controlled by a desktop computer running a script-based program, that sends commands to built-in National Instru-

ments (NI) hardware<sup>16</sup>, GPIB, RS-232 or via Ethernet (VISA) to the experiment components. The NI hardware consists of 4 cards with analog and digital outputs, in total 48 digital (5 V), 16 analog 16Bit and 32 analog 13Bit channels with  $\pm 10$  V output. The timing resolution of the control program is  $25 \mu\text{s}$  for the cards with a precise timing while all other interfaces are set by the operating system which leads to few ms jitter. These devices are therefore only configured via these interfaces and triggered via the digital NI cards. The control program is called *Goodtime* and was developed by Jakob Reichel with further additions by Pascal Böhi [111] and Caspar Ockeloen [129]. The camera data is recorded and analysed by *Matcam2*, a matlab based program that has been programmed by Caspar Ockeloen. For recording spectra and traces of the membrane oscillator a spectrum analyser<sup>17</sup> sends the data to *Goodtime* via ethernet.

## 3.7 System performance

This section describes the performance of the 2D-MOT and 3D-MOT including optical molasses and lattice for the parameters used in the experiment. Photographs of the operational 2D-MOT and 3D-MOT can be found in appendix A.

### 3.7.1 2D-MOT performance

In the experiment we use the 2D-MOT in a configuration without the counter-propagating  $2\text{D}^+$  molasses beam along the atom beam axis. This way the beam co-propagating with the atoms acts as a push beam, with the difference that usually a push beam is resonant with the atoms and its size is that of the differential pumping tube. The full  $2\text{D}^+$ MOT configuration has so far not been necessary, as the 3D-MOT gets fully loaded in about one second, which is sufficient. The 2D-MOT beams use in total 180 mW of cooling light and 5.6 mW of repumping light, which corresponds to a maximum cooling light intensity in each beam of  $I = 11 I_s$ .

The frequencies of 2D-MOT and 3D-MOT are linked via the common source laser frequency, such that the relative frequency cannot be changed within the experimental sequence. The loading rate optimization is therefore done exploiting the time-of-flight (TOF) between 2D-MOT and 3D-MOT by shortly switching on the 2D-MOT for different parameters and capturing the atoms using a fixed parameter set. The resulting parameters are a laser detuning  $\Delta_{\text{LA}} = -2.7\Gamma$  and a gradient of 20 G/cm, at which a loading rate of  $R = 2.4 \times 10^9 \text{s}^{-1}$  is achieved with a maximum atom flux around 13 m/s, equal to a transit time of 37 ms between 2D and 3D-MOT. The data is shown in figure 3.9. The flux distribution is calculated from the switch-off function of the 2D-MOT in TOF by recording the atomic fluorescence  $S(t)$  at the 3D-MOT using resonant light in zero magnetic field as a function of time [108, 113]. The time delay between switching off the 2D-Mot and the reduction of

---

<sup>16</sup>NI 6534, 2x NI 6733, NI 6723

<sup>17</sup>Rohde & Schwarz FSV7

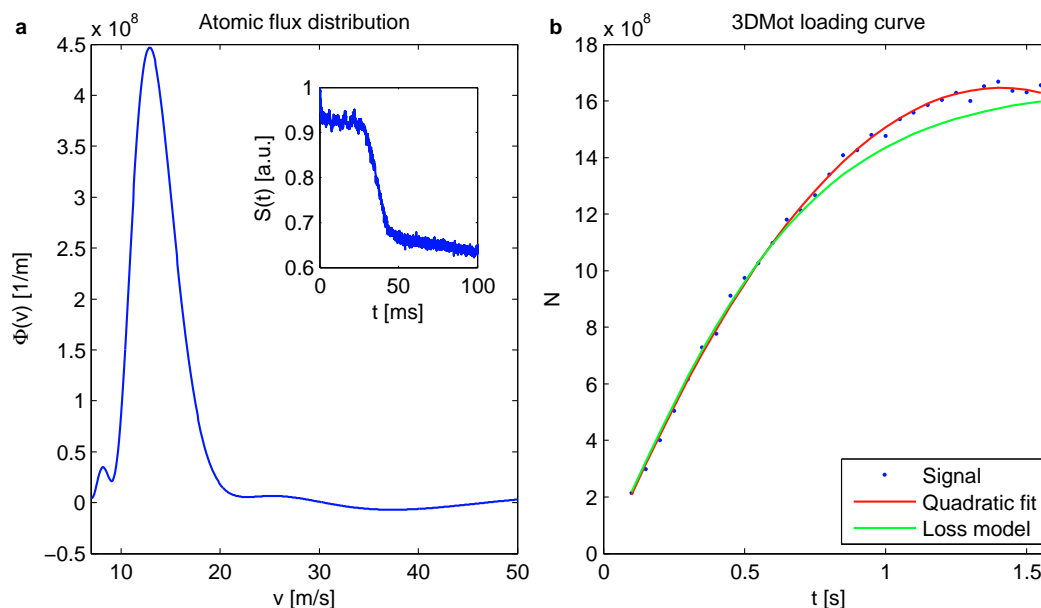


Figure 3.9: **a**: 2D-MOT flux distribution and **b**: MOT loading curve. The loading rate is deduced from the initial slope of the loading curve fit. The flux was calculated using a polynomial fit to the fluorescence signal  $S(t)$  shown in the inset. The fits to the loading curve are one using a density dependent loss model and a better fitting quadratic curve that is used to extract the loading rate as the initial slope.

recorded fluorescence allows to calculate velocity dependent flux  $\Phi(v)$ , which is

$$\Phi(v) = -\frac{t}{\eta} \frac{dS(t)}{dt}, \quad t = \frac{d}{v} \quad (3.12)$$

with atom travelling length  $d$  and normalization factor  $\eta$  that relates the measured signal to the number of atoms, such that  $\int \Phi(v) dv = R$  assuming a full capture in the 3D-MOT. The loading rate  $R$  is extracted as the initial slope of the quadratic fit in figure 3.9b. To calculate the derivative  $dS/dt$  a higher order polynomial was fitted to the data.

Compared to other 2D-MOT setups [113, 114, 108], our flux distribution has a similar peak velocity and a total flux not quite as high as in the 2D<sup>+</sup>MOT configurations, but can probably be increased by implementing the full 2D<sup>+</sup> configuration if necessary. In addition, the measured value represents a lower limit, as one assumes perfect capturing of the atomic beam by the 3D-MOT.

### 3.7.2 3D-MOT performance

The 3D-MOT was first optimized similar to the 2D-MOT by only loading for a short time with fixed 2D-MOT conditions, switching to the 3D-MOT parameters and

### 3.7. System performance

---

switching the 2D-MOT off before the first atoms arrive. In the end, a configuration with  $\Delta_{\text{LA}} = -3.1\Gamma$  was found to be optimal in terms of maximum atom number together with a magnetic field gradient of 11 G/cm along the strong vertical axis. To account for the different optimal detunings of 2D-MOT and 3D-MOT, the 2D-MOT AOM frequency was lowered by  $0.4\Gamma$ . A total cooling power of 52 mW, which corresponds to  $9.2 I_s$  peak intensity is available together with 1.2 mW of repumping light.

The loading performance is shown in figure 3.9b. For a large and dense cloud the atom number is limited by density dependent losses or trap size, showing up as a non-exponential loading behaviour.

For the loading process in figure 3.9b the temperature, cloud size and peak initial volume density is recorded for each data point and shown in figure 3.10 as a function of atom number. The density is determined as peak density assuming a Gaussian profile and rotational symmetry ( $\sigma_x = \sigma_y$ ,  $T_x = T_y$ ) around the vertical axis. From the width of the atomic cloud for different  $t_{\text{TOF}}$  one can deduce the atomic temperature assuming ballistic expansion as

$$\sigma_{x,y,z}(t_{\text{TOF}}) = \sqrt{\sigma_{x,y,z}(0)^2 + \frac{k_B T_{x,y,z}}{m} t_{\text{TOF}}^2} \quad (3.13)$$

with temperature  $T$ , atomic mass  $m$ , Boltzmann constant  $k_B$ , and initial width  $\sigma_{x,y,z}(0)$ . The atomic volume density is then described as

$$n_a(x, y, z) = \frac{N}{(2\pi)^{3/2} \sigma_x \sigma_y \sigma_z} e^{-\frac{x^2}{2\sigma_x^2} - \frac{y^2}{2\sigma_y^2} - \frac{z^2}{2\sigma_z^2}}. \quad (3.14)$$

As one can see in figure 3.10, the temperature as well as the *in situ* cloud size increases with atom number. This shows the effect of radiation pressure caused by scattered photons. The outward force is increasing the volume as can be seen in the increased cloud width, which is equivalent to an increased temperature inside a trapping potential. For large traps like this one, a large MOT temperature up to mK is typical [130], as the temperature is expected to grow as  $T \propto n_a^{2/3} N^{1/3}$  [131].

When looking at the density, it first increases and then decreases again with atom number. Up to the maximum, the growing atom number is not compensated by the increased temperature, after that the density is limited by the rising temperature, that even decreases the density again. The overall change is only about 20%.

The maximum atom number is not limited by background gas collision losses, as one would expect an exponential loading curve  $N(t) = R/\gamma(1 - e^{-\gamma t})$  as a result of the rate equation  $dN/dt = R - \gamma N(t)$ . In this case, the lifetime of the atomic cloud would correspond to the loading time constant  $1/\gamma$ . One explanation for the non-exponential loading curve are density dependent losses, such as light assisted collisions [71]. To incorporate these losses into the loading curve, the differential

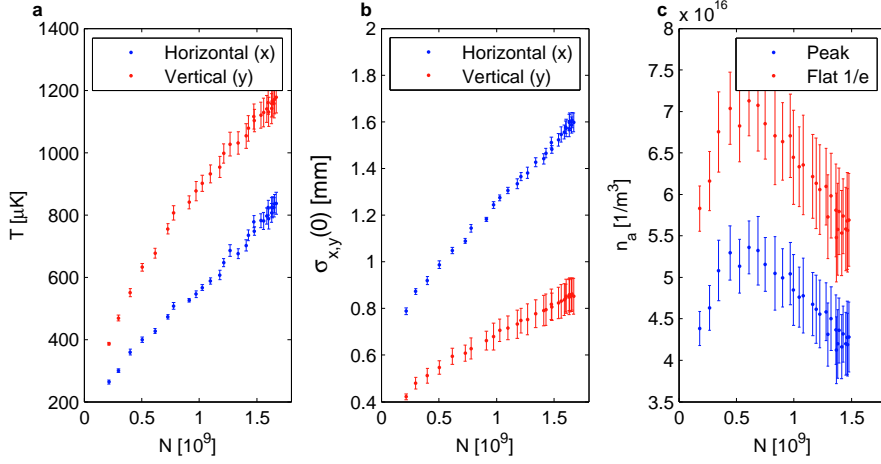


Figure 3.10: 3D-MOT parameters in dependence of loaded atom number: **a** Temperature, **b** *In situ* cloud width, **c** Maximum density for a Gaussian distribution and alternatively a constant density up to the  $1/e$  width of the Gaussian. The two scenarios are hard to distinguish in TOF.

equation is extended by a density dependent loss rate  $\beta n_a(t)$  and comes to

$$\frac{dN}{dt} = R - \int_V \gamma n_a(t) - \int_V \beta n_a(t)^2 \quad (3.15)$$

$$\approx R - \gamma N(t) - \frac{\beta}{V} N(t)^2 \quad (3.16)$$

where the approximation assumes a homogeneous density  $n_a$  over the constant trap volume  $V$ . The solution is

$$N(t) = \frac{V\sqrt{\gamma^2 + 4\beta R/V}}{2\beta} \tanh\left(\tanh^{-1}\left(\frac{\gamma}{\sqrt{\gamma^2 + 4\beta R/V}}\right) + \frac{t}{2}\sqrt{\gamma^2 + \frac{4\beta R}{V}}\right) - \frac{\gamma V}{2\beta}. \quad (3.17)$$

Although this model assumes a constant volume, which is not true in our case, this flaw cannot explain the quick stop in loading as observed in figure 3.9b. For an increasing volume  $\beta/V$  would decrease and so would the curvature. Surprisingly a quadratic curve perfectly fits the loading process.

The lifetime of the 3D-MOT can in principle be used to determine the residual gas pressure in the vacuum chamber [116]. However, density-dependent loss terms increase the loss rate, so a simple exponential fit overestimates the vacuum pressure. Taking into account these losses the decay can be calculated using equation 3.16 with  $R = 0$  and initial atom number  $N_0$  to

$$N(t) = \frac{\gamma}{\beta/V + (\gamma/N_0 + \beta/V) e^{\gamma t}} \quad (3.18)$$

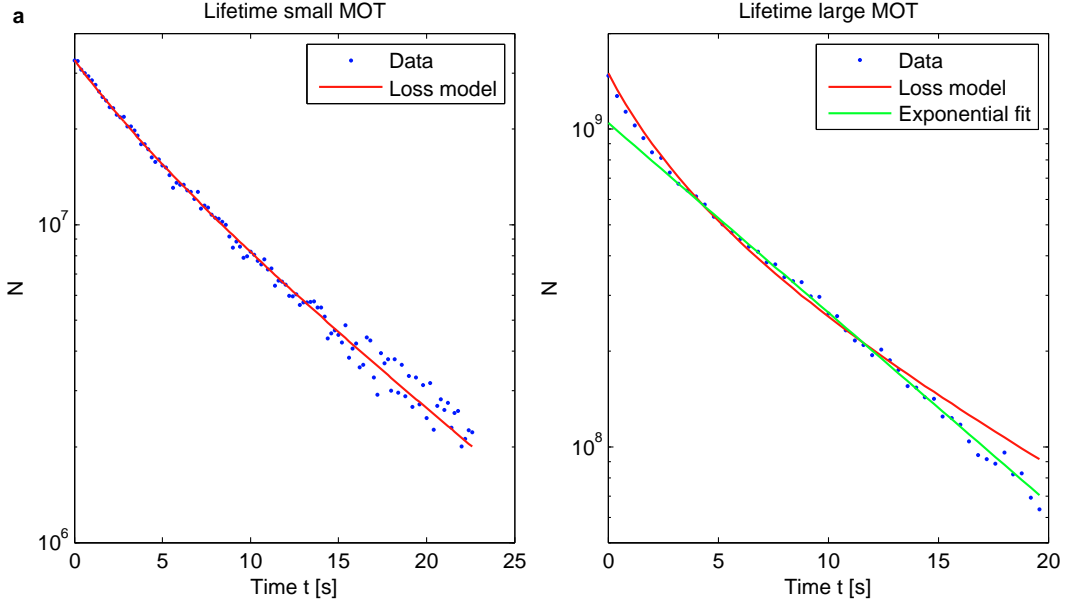


Figure 3.11: 3D-MOT lifetime evaluated for a large (a) and small (b) atomic cloud. The density fit model is not compatible with the large cloud measurement, as the initial decay is too steep. The rest of the data fits to a simple exponential decay.

which fits well for a small atom cloud with  $N_0 = 5 \times 10^7$  atoms,  $\gamma = 0.1/s$  and  $\beta/V = 2 \times 10^{-9}/s$  being extracted, see figure 3.11a. Assuming a volume up to the  $1/e$  width of the Gaussian fit to the cloud results in  $\beta \approx 10^{-17} \text{ m}^3/s$ , which is in reasonable agreement to values in literature [132], as  $\beta$  strongly depends on all MOT parameters [116]. For a full cloud the initial decay is faster than allowed by the model, resulting in a bad fit in figure 3.11b. In addition, the parameters found in the analysis of the small MOT lifetime would lead to a much faster decay in the large MOT. An explanation is the transition into a regime of constant density ( $n_a = N/V$  in equation 3.16) for increasing atom number, which leads to a constant decay rate  $\gamma + \beta n_a = 0.14/s$ , in agreement with the initial loss rate of  $0.14/s$  in figure 3.11a. This is supported by the measured density values in figure 3.10, which only vary by 20% over the measurement.

The initial strong losses of  $0.27/s$ , which are not accounted for in the constant density explanation, behave analogously to the abrupt stop in the loading curve. This loss process, which does not behave like a density dependent effect, could be a limitation of the cloud volume due to laser beam size. A cloud size of  $\sigma_x = 1.6 \text{ mm}$  corresponds to a  $1/e^2$  radius of  $3.2 \text{ mm}$ . There, the laser intensity already dropped to 56%.

The extracted  $\gamma$  is still dependent on the MOT configuration. For the presented system the lifetime is  $\tau = 1/\gamma = 9.7 \text{ s}$ , for a smaller MOT detuning of  $\Delta_{LA} = 2\Gamma$  the lifetime is  $\tau = 14.8 \text{ s}$  with a much higher cloud temperature. This behaviour can be

explained by the changed recapture probability for background gas collisions [132] due to the change in trap depth. For an assumed trap depth of 1K [132] for our parameters the pressure-dependent loss coefficient is about  $\gamma/p \approx 2 \times 10^7/\text{mbar s}$  [116], which leads to a relatively high pressure of  $p = 5 \times 10^{-9}$  mbar. The recently installed far detuned dipole trap, which is not discussed in this thesis (see outlook), shows a lifetime of about 3.5s, which is similar to the magnetic trap lifetime in comparable chip trap based vacuum systems [103, 110, 111]. Therefore, the pressure seems to be much better than the value derived from the MOT lifetime.

### 3.7.3 Optical molasses

The goal of the optical molasses [69] is to cool the atomic cloud to lower temperatures after an initial MOT and apply a damping force to the atoms, that will extract energy from the mechanical oscillator in the coupled system. Our molasses is operating at the same laser intensities as the MOT, but with the maximum detuning  $\Delta_{\text{LA}} = -11\Gamma$  and without magnetic field gradient. The residual earth magnetic field is zeroed by the compensation coils. The initial cooling performance is shown in figure 3.12. From the decay in temperature one extracts a cooling rate of  $\Gamma_a = 9.0 \times 10^3/\text{s}$  ( $9.3 \times 10^3/\text{s}$ ) for the horizontal (vertical) axis. This roughly fits to the theoretical value of  $\Gamma_a = 7.6 \times 10^3/\text{s}$  calculated using equation 1.81. Furthermore, the final temperatures of  $T = 25\mu\text{K}$  ( $40\mu\text{K}$ ) are axes dependent due to the initial conditions, but the horizontal one rises afterwards to  $40\mu\text{K}$  (not shown in plot). As a second effect of the molasses, the cloud size is decreased and therefore the density increases on short time scales. This is unexpected, as the molasses does not provide any trapping potential. A residual magnetic field during the switching process could lead to a short term compression, as the increased detuning lowers the outward radiation pressure due to less rescattered photons. The temperature and cloud size along the horizontal imaging axes differ about 20% after 10ms of molasses cooling, as determined by imaging a small molasses cloud with the second camera.

For longer molasses phases the properties change as shown in figure 3.13. The atom loss is much larger in the beginning with  $\tau = 0.021\text{ s}$  and a long term lifetime of  $\tau = 1.1\text{ s}$ . Besides the atom loss, the nature of the molasses leads to atomic diffusion, which increases the cloud width. Interestingly, the cloud does not diffuse in vertical direction, which could be due to a residual magnetic field gradient along this axis. Another possibility is the interplay between gravitation and the spatially dependent optical force due non-vanishing OD. The density is therefore roughly  $n_a \propto 1/t$  dependent instead of  $n_a \propto 1/t^{3/2}$  for 3 dimensional diffusion  $\partial n_a(\vec{r}, t)/\partial t = D\nabla^2 n_a(\vec{r}, t)$  with diffusion constant  $D$ . In case of a smaller atom cloud a perfect  $1/t$  dependence is realized, although atom losses and initial vertical expansion are present. The molasses temperature also decreases with decreasing density, showing that the temperature is limited by density.

### 3.7. System performance

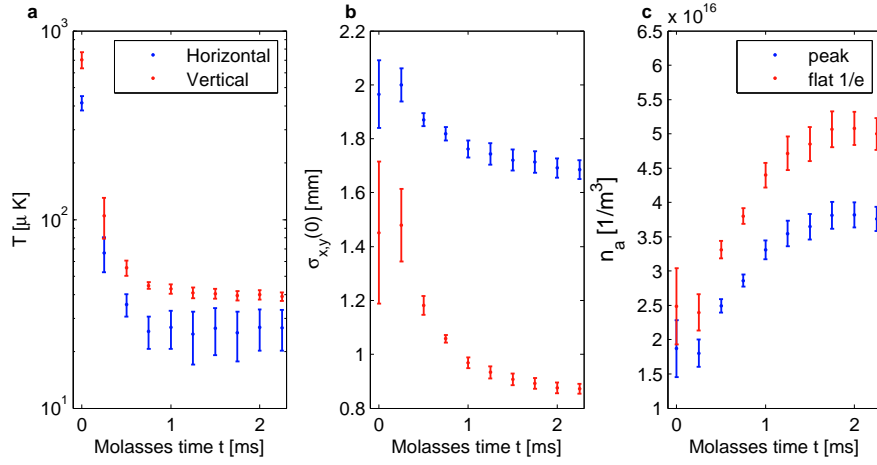


Figure 3.12: Cloud parameters of the molasses after a short time  $t$ . The molasses is quickly cooling the atomic ensemble. The atom cloud is also compressed on the short time scale, which is probably the result of a finite magnetic field switching time.

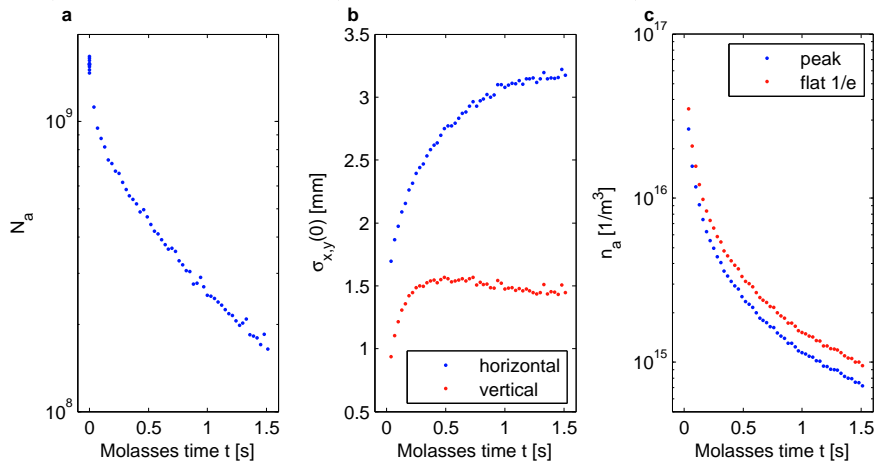


Figure 3.13: Cloud parameters in a long molasses phase. **a:** A very high initial atom loss is followed by a slower exponential decay. **b:** the expected increase in cloud size caused by atomic diffusion is not present in the vertical axis. **c:** the density shows a  $1/t$  dependence, which would be expected in a 2 dimensional system.

### 3.7.4 Optical lattice

The optical lattice is part of the membrane-atom coupling setup. The laser used is described in detail in chapter 4. It consists of a power stabilized gaussian beam of power  $P_0$  with  $1/e^2$  intensity radius  $w = 284\mu\text{m}$  and detuning  $\Delta_{\text{LA}}$  from  $^{87}\text{Rb}$   $D_2$  line, and a fraction  $\alpha^2 = 0.51$  of its intensity is reflected from the optomechanical cavity. The intensity transmission through the whole glass cell is  $t_{\text{cell}}^2 = 0.95$ . The stated width is a mean over the incoming and reflected beam values for both axis ( $w_x^{\text{in}} = 287\mu\text{m}$ ,  $w_y^{\text{in}} = 282\mu\text{m}$ ,  $w_x^{\text{re}} = 265\mu\text{m}$ ,  $w_y^{\text{re}} = 301\mu\text{m}$ ), which is a good approximation for calculating the trap frequency and depth. The lattice is loaded by overlapping it with the optical molasses and extends over  $2R_a = 7\text{mm}$ , as shown in figure 3.14 in the upper plot, where the molasses was dropped by switching it off to separate it from the atoms inside the lattice. For this configuration the axial trap frequency is calculated according to equation 1.77 as  $\Omega_a = \zeta\sqrt{P_0/|\Delta_{\text{LA}}|}$  with  $\zeta = 2\pi \times 6.0 \times 10^{11}\text{Hz}^{3/2}/\text{W}^{1/2}$ , and a frequency ratio  $\Omega_a/\Omega_r = 1.6 \times 10^3$ . A calibration measurement yields  $\zeta = 2\pi \times (5.3 \pm 0.1) \times 10^{11}\text{Hz}^{3/2}/\text{W}^{1/2}$ , which is a reasonable agreement.

This calibration was carried out using parametric heating by modulation of the lattice power. Plot **a** in figure 3.14 shows the measurement for a detuning of  $\Delta_{\text{LA}} = -20.2\text{GHz}$  and different lattice powers. The measured parameter is the relative atom loss caused by the modulation in dependence of the modulation frequency  $\Omega_{\text{mod}}$ . For parametric modulation of trap depth one expects a resonance at  $\Omega_{\text{mod}} = 2\Omega_a$ . The atom number is measured after a hold time to separate the lattice and molasses. In total seven measurements with different detunings  $\Delta_{\text{LA}}$  were taken, and the lower right edge of the loss resonance was taken as the maximum trap frequency in the lattice center, as marked by the thick dots in the figure. The dip around the membrane frequency is the same for every configuration and probably due to direct membrane excitation, which leads to atom heating due to the coupling. The overall width of the resonance points to a large inhomogeneous broadening of the atomic oscillation frequencies. In plot **b** of figure 3.14 the values are plotted against  $\sqrt{P_0/|\Delta_{\text{LA}}|}$ .  $\zeta$  is calculated as the slope in a linear fit to the data.

In order to characterize the lattice parameters, one has to separate the trapped lattice atoms from the molasses by switching the molasses off and letting it drop out of the lattice volume. This takes at least 30 ms, in which most of the lattice atoms are already lost in the case of small detuning  $|\Delta_{\text{LA}}| \lesssim 20\text{GHz}$ . Therefore a proper characterisation of the lattice itself cannot be carried out below this detuning.

For a larger detuning, the temperature, the lifetime and extrapolated initial atom number were measured. The lifetime and therefore also atom number show large variations with  $\tau \approx 15\text{ms}$  (40 ms) lifetime and  $N \approx 3 \times 10^8$  ( $1 \times 10^7$ ) initial atoms in the lattice for  $\Delta_{\text{LA}} < 20\text{GHz}$  ( $> 20\text{GHz}$ ). The temperature measurement is more complicated than for a regular molasses, as the aspect ratio of the cloud is large and the atomic distribution is not uniform along the lattice direction due to interference patterns of the molasses beams, see figure 3.14. These interference patterns show up in the atomic density in *in situ* images of very small MOT cooled clouds. To

### 3.7. System performance

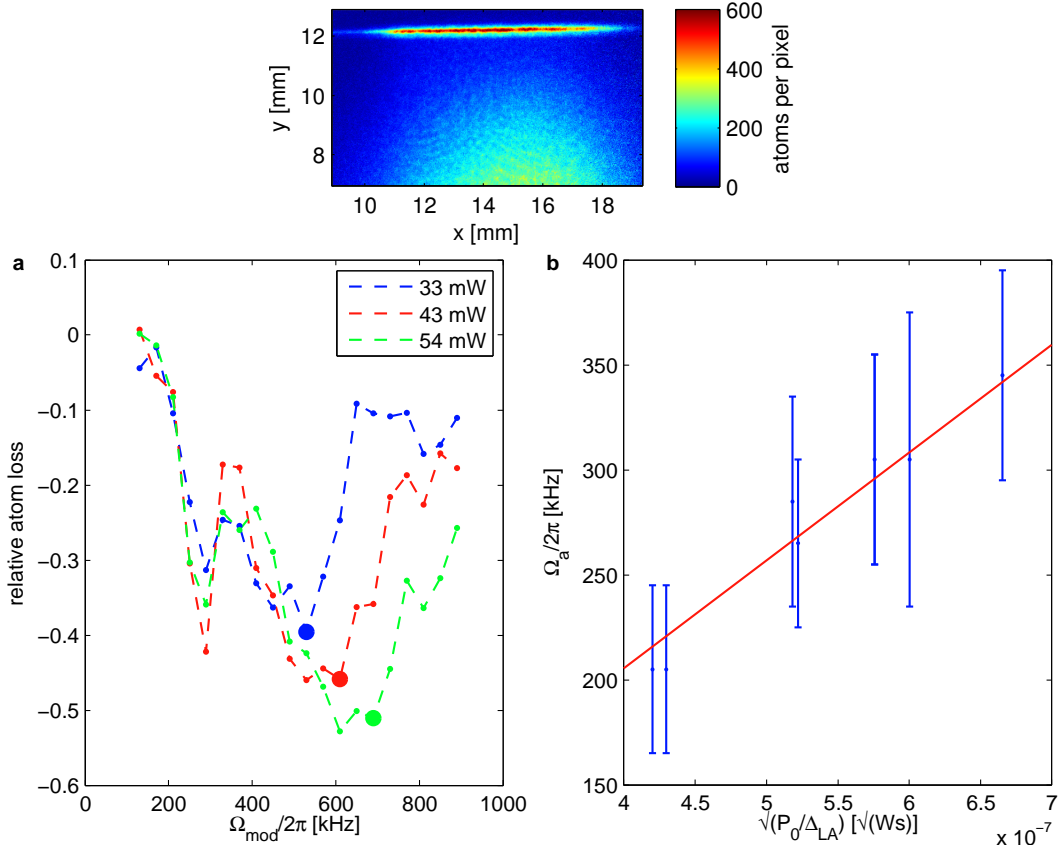


Figure 3.14: Lattice oscillation frequency measurements: The lattice and molasses have to be separated by dropping the molasses in order to perform measurements, as shown in the top picture. **a**: Relative change of atom number due to lattice power modulation. The measurement points are connected for clarity. **b**: atomic frequency in dependence of  $\sqrt{P/\Delta_{\text{LA}}}$  and linear fit to calculate the proportionality constant  $\zeta$ .

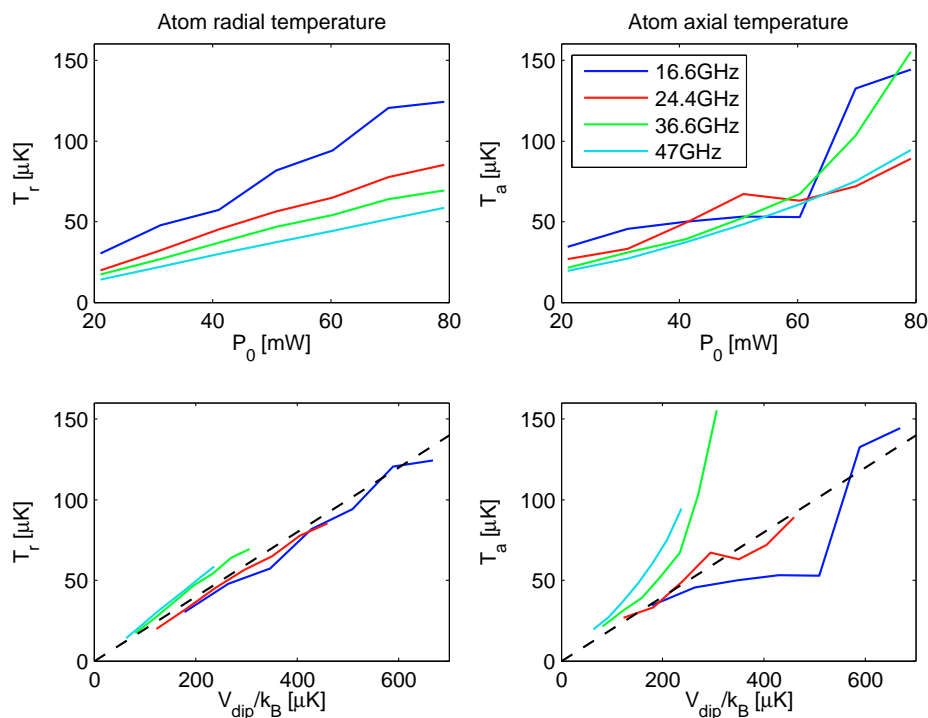


Figure 3.15: Lattice temperature in dependence of laser power and potential depth for the radial and axial direction and different detunings. The dotted line corresponds to  $k_B T = V_{\text{dip}}/5 \approx V_m/5$ .

analyse the temperature, the molasses was first switched off and dropped, before the atomic distribution in the lattice is recorded  $50 \mu\text{s}$  after switching off the lattice. This distribution is then taken as the *in situ* distribution and convolved with a two-dimensional Gaussian to fit the cloud expansion in larger TOF measurements, from which the temperature is inferred. The resulting values as a function of lattice power, lattice depth and detuning are shown in figure 3.15 for the radial and axial component.

The radial temperature increases with lattice power and lower detuning, which when plotted as a function of trap depth follows a line of  $k_B T = V_{\text{dip}}/5$ , which points to a trap depth limited temperature, possibly due to evaporation [133]. The scattering rate from the lattice that heats the atoms is  $\Gamma_{\text{sc}} \approx 10^4/\text{s}$  according to equation 1.74 and 1.78 for  $\Omega_a = \Omega_m$  and  $\Delta_{\text{LA}} = 2\pi \times 20 \text{ GHz}$ . The expected heating rate is  $\dot{T} = T_{\text{rec}}\Gamma_{\text{sc}}/3 = 1.2 \text{ mK/s}$  [71] with recoil temperature  $T_{\text{rec}} = 360 \text{ nK}$ , which can easily be compensated by the molasses. Indeed, without the molasses the atoms inside the lattice are heated up by  $V_{\text{dip}}/5$  within 33 ms, which is approximately the lattice lifetime.

The observed  $k_B T = V_{\text{dip}}/5$  temperature limit requires therefore a thermalization

process, such that evaporation can take place. The thermalization rate via elastic ground state collisions [134] is only about  $\Gamma_{\text{el}} = n_a 16a^2 \sqrt{\pi k_B T / m} \approx 15/\text{s}$  with scattering length  $a \approx 100a_0$  and Bohr radius  $a_0$  for the trap density of  $n_a = 3 \times 10^{17}/\text{m}^3$  and temperature  $T = 40 \mu\text{K}$  in the trap. An additional contribution are excited state collisions, where the scattering cross section is much larger. In addition, the initial energy distribution when switching off the molasses is not a thermal distribution, but corresponds rather to a uniform atomic density over the lattice volume. The heating therefore directly expels atoms on the high energy tail of the distribution directly. Other loss mechanisms like hyperfine changing collisions [135] also contribute to the atom loss, at the calculated atomic density of  $3 \times 10^{17}/\text{m}^3$  for  $k_B T = V_{\text{dip}}/5$  and  $N = 10^7$  the loss rate is  $\beta n_a = 6/\text{s}$  for a maximum  $\beta = 2 \times 10^{-17}/\text{m}^3$  [135].

The axial temperature is much less stable, probably due to the fluctuating phase in reflection of the optomechanical cavity caused by the imperfect stabilization of cavity detuning  $\Delta$ . The temperature measurement shows therefore much larger fluctuations, as the phase noise amplitude changes slowly between measurements. It appears to be dependent on the lattice power  $P_0$  rather than the potential  $V_{\text{dip}}$  as one can see in figure 3.15. This leads to temperatures  $k_B T > V_{\text{dip}}/5$  with the lowest temperature for the lowest detuning, the inverse of the expected result. The very presence of larger temperatures might be explained by the larger extend of the cloud along the axial direction, such that atoms take longer to leave the trap and can be recaptured along the way. The atoms are only coupled to the membrane motion for a potential depth  $V_{\text{dip}}/k_B \gtrsim 500 \mu\text{K}$ , corresponding to  $\Omega_a(0) > \Omega_m$ , so this heating mechanism can mostly be excluded in this measurement, except in the 16.6 GHz measurement, where a strong temperature increase above  $500 \mu\text{K}$  is observed. As another possible heating process, technical heating by parametric excitation is also dependent on the potential via the atomic oscillator frequency [136], such that it cannot explain the apparent pure power dependence of the temperature.

In our coupling experiment, the lattice is overlapped with a molasses for cooling and preventing fast atom loss all the time, which realizes a different setting. The measurements in chapter 5 suggest that for a lattice overlapped with a molasses, the lattice properties are dominated by the molasses. Especially the model of a constant atomic density across the lattice leads to a correct description of the coupling. A comparison of molasses parameters with and without a lattice present also suggests that the lattice does not significantly alter the molasses properties.

#### 3.7.5 Conclusion

The constructed ultra-cold atom system is able to trap about  $N = 1.6 \times 10^9$  atoms, much more than the previous one [104]. The loading rate of  $R = 2.4 \times 10^9/\text{s}$  is also larger. With the compact construction and available additional optical access future extensions like a transverse lattice and other beams are possible. The atomic cloud appears to be limited by the cooling laser beam size right now, which can be overcome by increasing the magnetic field gradients at the expense of a larger

temperature.

The optical molasses cools the atoms to a temperature of  $T = 40 \mu\text{K}$  with a damping rate of  $\Gamma_a = 9 \times 10^3/\text{s}$  and initial densities up to  $n_a = 4 \times 10^{16}/\text{m}^3$ . These are the parameters that characterize the membrane-atom coupling in the hybrid system in chapter 5, as the properties of the coupling lattice turns out to be dominated by the molasses.

The near-resonant lattice with the low lifetime could not be characterized in the configuration of the hybrid system experiment, but the presented measurements at higher detuning are used to measure the trap frequency constant  $\zeta$ , such that the frequencies for a lower detuning can be calculated. The lattice temperature analysis shows, that the heating associated with the lattice light scattering rate is a mayor source of atom loss. This process will also be present in future systems, where the atoms are isolated using an additional transverse lattice. The instability in the cavity lock also has to be addressed in future experiment improvements.



## Chapter 4

# Optomechanical system: Membrane in a Cavity

Optomechanical systems in the membrane-in-middle configuration are usually designed to reach the resolved sideband regime  $\kappa \ll \Omega_m$  to enable groundstate cooling [4]. This leads to long cavities with very high finesse and high frequency oscillators [64, 137, 11]. In our case the membrane in a cavity system is part of the hybrid membrane-atom system and designed differently to match the requirements for the hybrid system. This includes explicitly not being in the resolved sideband regime, as the coupling requires an instantaneous response of the cavity field at the membrane frequency  $\Omega_m \ll \kappa$ . This significantly reduces the requirements on the optomechanical cavity, especially in the case of low frequency mechanical oscillators. Furthermore, the trapping of atoms with axial oscillation frequency  $\Omega_m$  requires large laser powers  $P_0 \propto \sqrt{\Omega_a}$  to fulfill the resonance condition  $\Omega_m = \Omega_a$ . Therefore, a relatively low frequency  $\Omega_m$  and finesse  $\mathcal{F}$  is needed to keep the peak circulating power low in order not to heat the membrane mode too much. Although the design is not optimal for standard cavity optomechanics, it still shows the optomechanical spring and damping effect as well as the impact of laser noise, which will be analysed in the following.

First the design of the membrane in a cavity system and laser system is discussed, followed by a characterization of the cavity and laser parameters. The following measurements of optomechanical behaviour are compared to the theoretical prediction based on the system characterization.

### 4.1 Design of the cavity system

In the following the desired parameters for the system are determined and the design of the cavity body is discussed.

#### 4.1. Design of the cavity system

---

Cavity length $L$	26.1(4) mm
Mirror curvature $R$	30 mm
Mirror reflectivity $r_1^2$	96.6%
Mirror reflectivity $r_2^2$	99.99%
Mirror diameter	1/4"
Free spectral range $\omega_{\text{FSR}}$	$2\pi \times 5.75(8)$ GHz
Linewidth FWHM $\kappa$	$2\pi \times (19 \dots 41)$ MHz
Finesse $\mathcal{F}$	140 ... 300
Coupling constant $G_{\text{max}}$	$2\pi * 9.75(15)$ MHz/nm

Table 4.1: Optomechanical experiment cavity parameters. Their measurement is discussed in the text.

##### 4.1.1 Cavity parameters

As already mentioned the finesse is the most important parameter, as  $\Gamma_{\text{sym}} \propto \mathcal{F}^2$  (equation 1.1 and 1.2). The required incoupled laser power is dependent on the beam waist  $w$  at the position of the atoms for a given atomic oscillation frequency as  $P_0 \propto w^2$ , see equation 1.70. Furthermore, the atom number in the lattice volume is  $N \propto w^2$ , so that the coupling constant for a maximum tolerable power on the membrane  $P_{\text{max}} = P_0 \mathcal{F}$  is  $g_N^2 \propto \mathcal{F}^2 N \propto \mathcal{F} P_{\text{max}}$ , such that a larger Finesse is favourable. However, by adding noise sources an optimum finesse of 400 for groundstate cooling was determined [45]. As a first step we decided to take a lower finesse of up to  $\mathcal{F} = 300$  to reduce alignment requirements and the influence of vibrations on the system.

The cavity end mirror was chosen to be low loss with high reflectivity  $r_2^2 > 99.99\%$  and  $t_2^2 = 70$  ppm to fulfil  $t_2^2 \ll t_1^2$ , while different front mirrors were fabricated in a series of reflectivities  $r_1^2 = 92, 96.6, 98, 99, 99.5\%$  within one evaporation run and  $r_1^2 = 96.6\%$  was chosen for the experiment, resulting in  $\mathcal{F} = 140 \dots 300$ . The radius was chosen to be  $R = 30$  mm and the mirrors are backside anti reflection (AR) coated. The cavity length is  $L = 26.1$  mm, which results in  $\omega_{\text{FSR}} = 5.75$  GHz and thus  $\kappa = 2\pi \times 19$  MHz to  $\kappa = 2\pi \times 41$  MHz.

With a mirror pair with  $r_1^2 = 96.6\%$  and  $r_2^2 = 99.99\%$ , the intensity reflection of the cavity on resonance is  $r_{\text{res}}^2 > 98\%$ , such that the loss is negligible for the coupling.

A summary of the optical properties discussed here and in the following sections is given in table 4.1.

##### 4.1.2 Mounting and alignment

The cavity mount design is shown in figure 4.1. The top input mirror is placed inside the titanium body and fixed with a screw from the back to make it exchangeable. The output mirror is mounted the same way, except that it is placed on a piezo

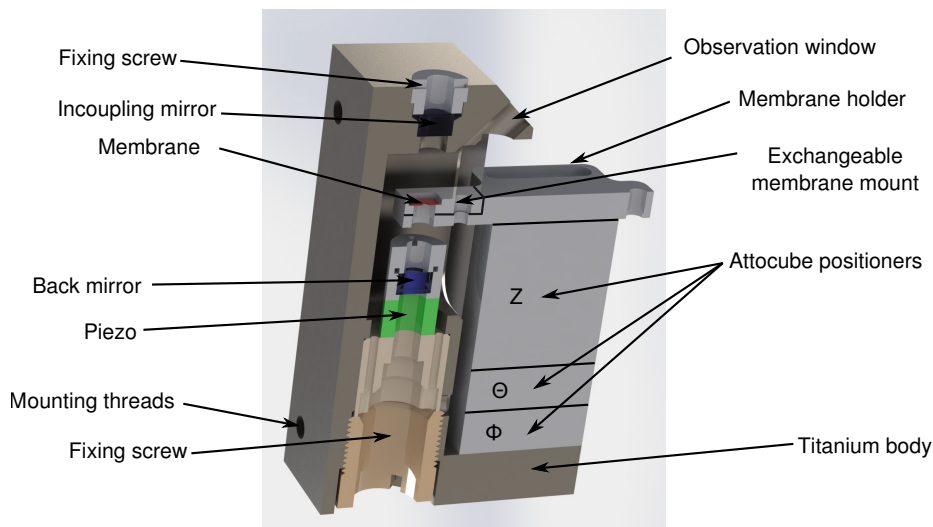


Figure 4.1: Schematics of the optomechanical membrane-in-middle cavity system.

to achieve tunability of the cavity resonance frequency. The membrane is put in between the mirrors on an aluminium mount, that is screwed into a holder. This holder rests on attocube positioners, which can move along the optical axis and tilt the membrane with respect to the optical axis. The maximum movement is  $\Delta z = 5 \text{ mm}$ ,  $\Delta\phi = 5.6^\circ$  and  $\Delta\theta = 6.4^\circ$ . This allows to place the membrane perpendicular to the optical axis in the exact middle of the cavity. The drawback of this design is the inability to transversally move the membrane, such that the match of optical and mechanical mode cannot be adjusted. As a second point, the rotation center of the  $\theta$  and  $\phi$  angle is not at the membrane position, but above the positioner stack. This leads to a crosstalk between the angular alignment and membrane position.

The cavity body material titanium was chosen as a well machinable material, which matches the positioners thermal expansion coefficient, thus preventing a differential shift of the membrane relative to the cavity due to thermal expansion.

The cavity is directly screwed upright to the wall of a vacuum chamber with AR-coated top and bottom viewports. The vacuum chamber is pumped down to  $\approx 10^{-7}$  mbar using an Ion pump and initially pumped down using a portable turbo pump station, see chapter 3. The chamber is placed with vibration isolation pads<sup>1</sup> onto a platform that itself rests on vibration isolation posts<sup>2</sup> to prevent vibrations of the system, especially the attocube positioners, which have low fundamental mode vibrational frequencies  $\Omega = 2\pi \times 140 \text{ Hz}$ . The platform holding the vacuum chamber also supports a second breadboard above the chamber for mounting optical components.

<sup>1</sup>Thorlabs Sorbothane sheet

<sup>2</sup>Newport NewDamp series

A more detailed description is given in [138].

## 4.2 System characterisation

The membrane-in-middle system properties are characterized using a laser system and optical assembly that is described in the following, before the actual cavity parameters are investigated and the laser's noise, which determines the cooling limit, is analysed.

### 4.2.1 Optical readout

The optical system layout is shown in figure 4.2. It consists of one diode laser with tapered amplifier<sup>3</sup>, which is split up into two parts, where one is used to read out the membrane motion with power  $P_R$  and the other one to cool the membrane mode with power  $P_0$  (at the position of the atoms). Their powers can be independently adjusted via two AOM that are operated using the same frequency source in order to prevent amplitude noise due to a beatnote between the beams. The laser power is controlled via a feedback loop using a photodiode signal [138] that is fed back on the control AOM power. Readout and cooling laser have orthogonal polarizations as they are combined on a polarizing beam splitter. The  $\lambda/4$  wave plate afterwards is only used to fine-tune the polarization to ensure that the reflected light travels back its incident path. The reflected readout light is separated using an optical isolator before detection.

The laser-cavity stabilization uses a Pound-Drever-Hall (PDH) scheme [66, 67], where sidebands are modulated onto the readout beam using a fiber electro-optical phase modulator (EOM) and demodulated from the readout photodiodes signal. Using this system, the phase information of the reflected light can be used to stabilize the system around resonance  $\Delta = 0 \pm \kappa/2$  as well as to readout the membrane motion. Therefore the signal is separated into a low frequency part for feedback and a high frequency part to readout the membrane motion, which is done using an additional amplifier<sup>4</sup> and a spectrum analyser<sup>5</sup>. The power spectrum of the membrane signal is proportional to the membrane temperature, see equation 1.13.

The feedback signal of the  $\Delta$  stabilization PI controller is used to change the resonance frequency of a high finesse optical reference cavity, on which the laser itself is locked via a fast lock to reduce its frequency noise around  $\Omega_m$ . The fast laser stabilization lock itself consists of a PDH based fast feedback on the laser current and piezo.

The system is identical to the one for coupling the atom-membrane system, except for the absence of atoms. A total laser power of 960 mW is available of which up to  $P_0 = 100$  mW are used for the cooling/coupling beam and  $P_R = 200$   $\mu$ W is

---

<sup>3</sup>Toptica Ta Pro, 780 nm, 1.5 W output power

<sup>4</sup>Stanford Research Systems SR560

<sup>5</sup>Rohde & Schwarz FSV7

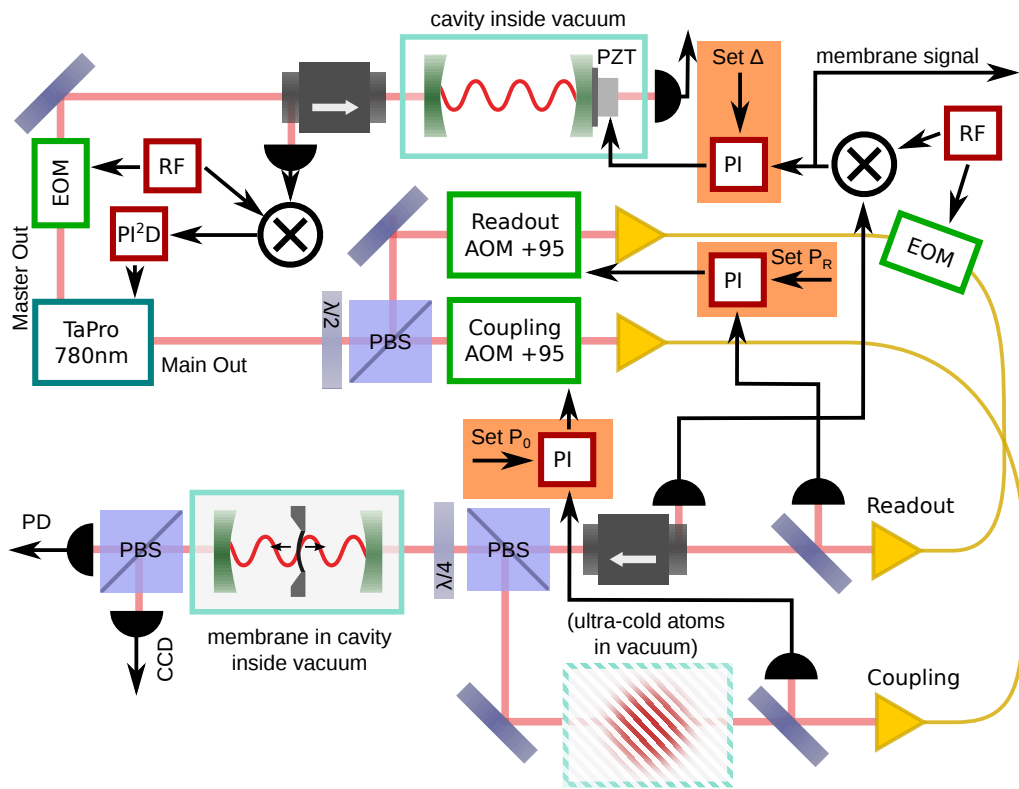


Figure 4.2: Schematics of laser system and optical assembly used in the optomechanics experiments. Details are given in the text. RF: Radio frequency source, PD: Photo diode, EOM: Electro-optical modulator, PBS: Polarizing beam splitter, PI: Proportional-integral controller

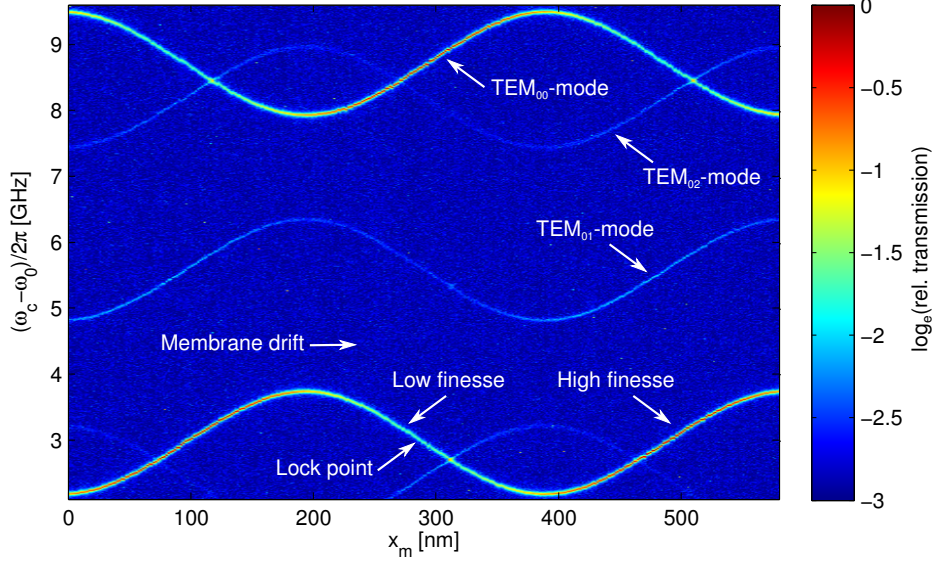


Figure 4.3: Cavity transmission spectrum as a function of laser frequency and membrane position. the marked modes are Hermite-Gauss modes  $\text{TEM}_{lm}$ . The high finesse regions can be identified by the higher transmission.

used for detection with 15% of the power per sideband. The modulation frequency is  $\Omega_{\text{mod}} = 2\pi \times 237$  MHz. The total power incident on the cavity at frequency  $\omega_L$  is then  $P_{\text{in}} = P_0 t^2 + 0.7 P_R$  with intensity transmission  $t^2$  between atoms and cavity.

### 4.2.2 Optical properties

The cavity's finesse, FSR and membrane reflectivity are analysed by measuring the cavity's transmission spectra. The laser is scanned over about  $\Delta\omega_L \approx 2\pi \times 26$  GHz and the transmission is recorded as a function of membrane position. A part of the resulting 2D spectrum is shown in figure 4.3. The spectrum shows several modes, that can be assigned to transverse cavity modes  $\text{TEM}_{lm}$  [55] using the CCD camera in transmission. If the membrane is properly aligned, they do not show any avoided crossings, which would be a sign of coupling between them.

In the picture the fundamental  $\text{TEM}_{00}$  mode repeats at the bottom with flipped sinusoidal resonance frequency modulation as expected (compare figure 1.4a). From the distance between the resonances one can determine the  $\omega_{\text{FSR}} = 2\pi \times 5.75(8)$  GHz and therefore the cavity length  $L = 26.1(4)$  mm. A fit to the modulation amplitude in equation 1.27 gives the membrane reflectivity  $|r_m| = 0.4148(5)$ , such that the maximum optomechanical coupling constant is  $G_{\text{max}} = 2\pi * 9.75(15)$  MHz/nm. The  $x_m$  dependent parameters and fit are shown in figure 4.4.

Using equation 1.28, the membrane thickness is estimated to be  $d = 40.6$  nm

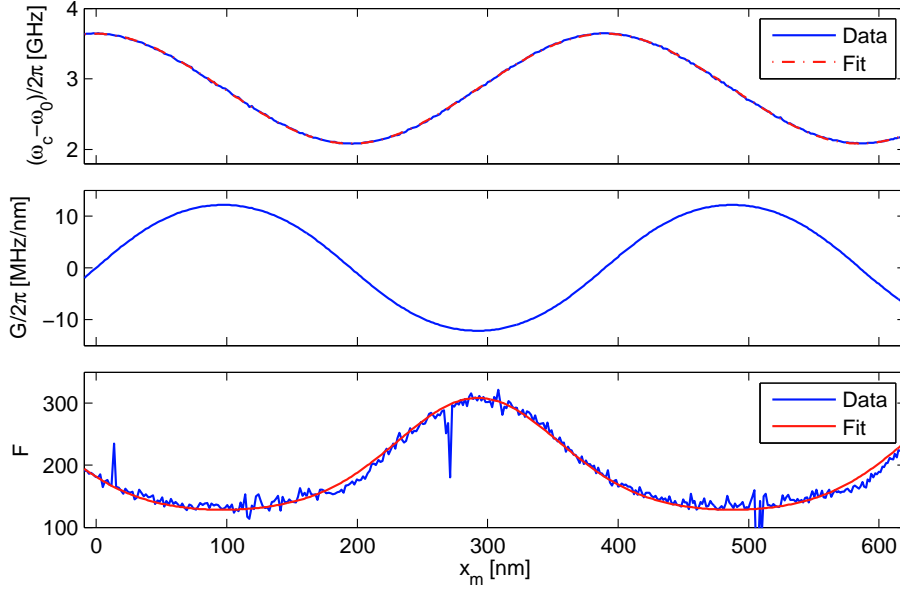


Figure 4.4: Membrane position dependent cavity frequency  $\omega_c$ , coupling  $G$  and finesse  $F$  measured using the optomechanical cavities fundamental TEM<sub>00</sub> mode. The fit to the resonance frequency results in  $|r_m| = 0.4148(5)$ . The finesse fit was carried out manually by varying the input mirror reflectivity as only free parameter with result  $r_1^2 = 0.966$ .

for a refractive index  $n = 2.0$  [11], such that the total membrane mass comes to  $M_{\text{phys}} = \rho dl^2 = 247 \text{ ng}$  with  $l = 1.5 \text{ mm}$ .

The cavities finesse is analysed by fitting to the Lorentzian resonance shape for each  $x_m$  in order to determine  $\kappa$ . The resulting finesse is shown as a function of  $x_m$  in figure 4.4. The finesse shows a variation dependent on  $x_m$  with the lowest and highest points of finesse located at  $\pm G_{\text{max}}$ , as expected from equation 1.38. The function is fitted to the data using the input mirror reflectivity  $r_1^2$  as a parameter, resulting in  $r_1^2 = 96.6\%$ , while the back mirror reflectivity was assumed to be  $r_2^2 = 99.99\%$  and has only little influence as long as  $t_1^2 \gg t_2^2$ . The sharp dips in the measured finesse are observed when the TEM<sub>00</sub> and the TEM<sub>02</sub> modes cross, resulting in a larger apparent  $\kappa$ .

The spectrum's frequency axis was calibrated and linearized using a reference cavity with known FSR. The  $x_m$  axis was calibrated using the resonance frequency function 1.27 with a second order argument  $\cos(\phi_0 + c_1 U + c_2 U^2)$  in order to compensate for nonlinearities in the voltage dependent piezo expansion  $x_m(U)$ . The shift in fitted  $\phi_0$  from one mode to the next higher longitudinal one can be used to determine the relative position of the membrane within the cavity. For a membrane at the center, the shift is  $\pi$ , as adding one node leads to a shift of the field from maximum to minimum at the membrane position and thus from lowest to highest

cavity mode frequency. If the membrane is at the cavity side, adding one node does not change the field at the membrane, thus the shift is zero. Therefore, the membrane position can be calculated to be  $x_m = L(\phi_0 - \phi'_0 - \pi)/2\pi$  from cavity center. In the presented measurement, the cavity is misplaced by  $x_m = 70 \mu\text{m}$ .

The incoupling efficiency into the fundamental Gaussian mode  $\eta^2$  is an important parameter for the theoretical analysis of the data, as it determines the circulating power inside the cavity, reduces coupling  $g_N$  and results in asymmetric atom-membrane coupling. The measurement of  $\eta^2$  however is difficult, as for the single sided cavity the absolute transmission relies critically on the unknown exact  $t_2^2$  and the reflection does not show significant reduction on resonance. An upper limit on the incoupling can be found by analysing the relative peak height of the different transverse cavity modes of the spectrum that results in  $\eta^2 = 0.69$ .

### 4.2.3 Cavity stabilization

In order to perform optomechanical cooling experiments, the cavity resonance  $\omega_c$  has to be kept fixed relative to the laser frequency  $\omega_L$ . The mentioned PDH scheme is used to generate an error signal for feedback. The feedback can either be applied to the cavity length  $L$  via the built-in piezo or to the membrane position via the attocube's piezo. The attocube's low resonance frequency leads to a strong excitation of the motion caused by the stabilization feedback loop. As the main noise on  $\omega_c$  is caused by this low frequency mode itself, it cannot be compensated this way. We therefore used the alternative way to feed back on the laser frequency to keep the detuning  $\Delta = \omega_L - \omega_c$  constant. This means that the laser frequency will drift over time as the cavity drifts, which is unproblematic for the optomechanics measurement as long as  $G$  does not change and also acceptable for the membrane-atom coupling, if the atomic detuning is not changed significantly (typically  $\Delta_{\text{LA}} \approx 2\pi \times 10 \text{ GHz}$ ). These issues are addressed in a new cavity system, which will be used in future experiments and is discussed in the outlook.

Figure 4.5a shows the PDH error signal together with the cavity transmission as a function of laser detuning  $\Delta$ . Each sideband carries 15% of the total power and is separated by the modulation frequency  $\Omega_{\text{mod}} \gg \kappa$  from the carrier in order to create the error signal. The asymmetry in the signal is caused by the slow photodiode used to record the transmission. The noise on top of the error signal is caused by the PID controllers display, but does not affect the lock performance.

Figure 4.5b shows the frequency of the laser locked to the cavity at low finesse during a typical experiment run. The overall drift is about 500 MHz/h which corresponds to a drift of the membrane position by 50 nm. The observed shift is always to lower frequencies at the low finesse position, such that it is very likely caused by a slow drift along gravity to larger  $x_m$  values. An expansion of the whole cavity as an alternative explanation would correspond to a temperature increase of 0.25° C/h over many hours, which is unlikely. On top of the slow drift a modulation of the resonance frequency can be seen, that is most likely caused by the static radiation pressure shift of the membrane and is 60 MHz or 6 nm for  $P_{\text{in}} = 64 \text{ mW}$ . Together

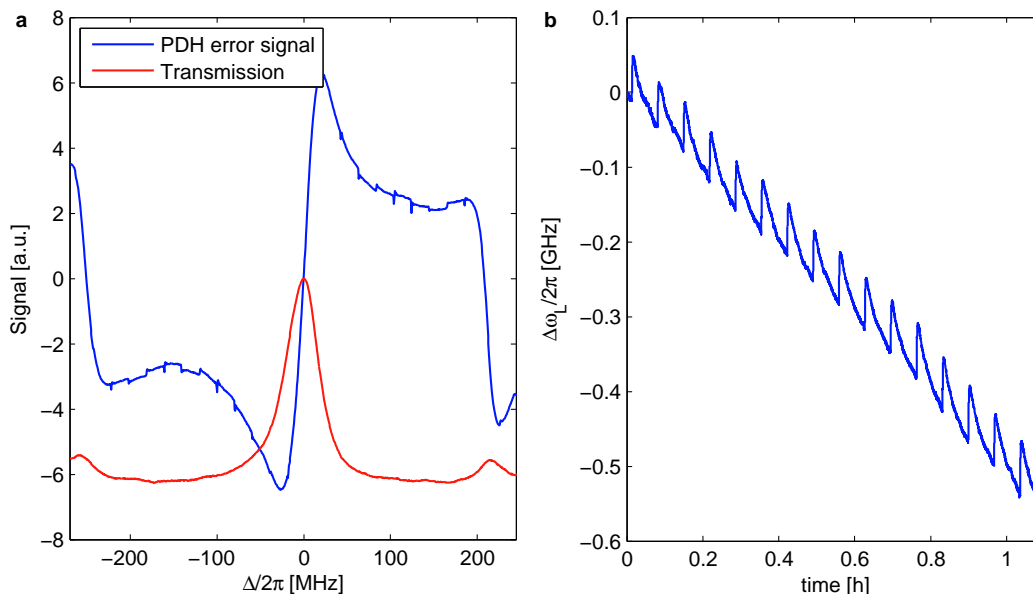


Figure 4.5: **a:** Sample cavity PDH and transmission signal as a function of laser detuning  $\Delta$ . The slope depends on the cavity finesse which is set by the membrane position  $x_m$ . **b:** shift of locked laser frequency  $\omega_L$  as a function of time during an experiment recorded using a wavemeter<sup>6</sup>. The modulation on top of the long term drift is caused by variation of the intra cavity power, that is ramped up repeatedly during the experimental runs.

with the calculated radiation pressure (equation 1.43) a very low spring constant of  $K = 3\text{ N/m}$  can be derived. A possible explanation is a vibration mode of the membrane frame that is only weakly glued to the mount and has a mass of only 10 mg, such that the oscillation frequency corresponding to the spring constant is  $\Omega = \sqrt{K/m} = 2\pi * 80\text{ Hz}$ , which is reasonable. The holders 140 Hz fundamental mode and the membrane oscillator have orders of magnitude higher spring constants.

#### 4.2.4 Laser noise

In optomechanical systems the minimum achievable temperature is usually limited by laser noise that acts as a hot thermal bath, as discussed in section 1.2.3. The measurement and reduction of laser noise is therefore necessary for cooling to low temperatures. In the noise spectrum, only the components at the oscillators frequency are important, as only they couple resonantly to its motion.

**Intensity noise and shotnoise level** The intensity noise can simply be measured on a photodiode with low noise and large detectable optical power. We use

## 4.2. System characterisation

---

a simple photodiode<sup>7</sup> connected to a low noise current amplifier<sup>8</sup>. An additional voltage amplifier<sup>9</sup> with high pass filter is used and the signal is then analysed on a spectrum analyser<sup>10</sup>. From the photodiode response and the amplification one can calculate the resulting signal or use it to verify the response. The photo diode's quantum efficiency can be determined from the response  $\mathcal{R} = I/P$  using  $I = Q/t = \text{QE} \bar{n}_{\text{ph}} e/t = \text{QE} P e/\hbar\omega_L$  with  $\bar{n}_{\text{ph}} = Pt/\hbar\omega_L$  to be  $\text{QE} = \mathcal{R} \hbar\omega_L/e = 0.62$  at  $\lambda = 780 \text{ nm}$ . The additional variables are current  $I$ , charge  $Q$ , electron charge  $e$ , time  $t$  and laser power  $P$ .

Using the quantum efficiency, one can calculate the shotnoise level, which represents the minimum noise. The relative photon shotnoise PSD is [139]

$$S_n(\Omega) = 2S_{nn}(\Omega) = \frac{2\hbar\omega}{\bar{P}} = \frac{2}{\dot{n}}, \quad (4.1)$$

with photon rate  $\dot{n}$  in [dBc/Hz] relative to the photon rate with  $\int S_n(\Omega) d\Omega/2\pi = \langle(\Delta\dot{n}/\dot{n})^2\rangle$ . It can be translated to electronic noise as they are connected via  $I/e = \text{QE} \dot{n}$ . The relative electron noise PSD is then  $S_e(\Omega) = 2/\text{QE} \dot{n}$  and leads to the same measured relative laser intensity noise PSD of

$$S_I(\Omega) = \frac{2}{\text{QE} \dot{n}} = \frac{2\hbar\omega}{\text{QE} \bar{P}}, \quad (4.2)$$

with  $\int S_I(\Omega) d\Omega/2\pi = \langle(\Delta I/\bar{I})^2\rangle$ , which is the relative shotnoise PSD of the detected photons. The total detected power over an impedance of  $R = 50 \Omega$  at the spectrum analyser would be  $P_e = U^2/R = (P \mathcal{R} A)^2/R$  with current to voltage amplifier conversion  $A$  in [V/A], if there was no high pass filter in the amplifier. The expected shotnoise power level measured on the spectrum analyser is then  $P_e S_I(\Omega)$  in [dBm/Hz].

In the measured spectrum the filter functions of the amplifiers and detectors are included, such that they have to be compensated for. The current amplifier has a bandwidth of 500 kHz and the voltage amplifier has also limited bandwidth and a high pass filter included. The filter function is determined using a fixed amplitude modulation on the laser and detecting the signal for various frequencies. Technical laser intensity noise adds to the shotnoise and results in a higher noise PSD  $S_I(\Omega) = \langle(\Delta I/\bar{I})^2\rangle = \langle(\Delta P/\bar{P})^2\rangle$  independent of  $\bar{P}$ . In order to measure this noise, it has to overcome the relative shotnoise PSD, which decreases as  $1/P$  (equation 4.1).

**Frequency noise** Frequency noise can be measured using a Michelson interferometer with an arm length difference. The signal of the interferometer in one output port is

$$P_{out} = P + \frac{P_{pp}}{2} \cos(\Delta l k), \quad (4.3)$$

---

<sup>7</sup>Thorlabs SM05PD2A

<sup>8</sup>Femto DLPCA-200

<sup>9</sup>Stanford Research Systems SR560

<sup>10</sup>Rohde & Schwarz FSV7

where  $P$  is the power in the middle of the fringe,  $P_{pp} \leq 2P$  the peak-to-peak power modulation and  $\Delta l$  is the arm length difference. The change of  $P_{out}$  with  $k$  is

$$\frac{dP_{out}}{dk} = \frac{P_{pp}}{2} \sin(\Delta lk) \Delta l. \quad (4.4)$$

Using  $dk/d\omega = 1/c$  one can rewrite the expression in terms of frequency:

$$\frac{dP_{out}}{d\omega} = \frac{P_{pp}}{2} \sin(\Delta lk) \frac{\Delta l}{c}. \quad (4.5)$$

To get the highest sensitivity to frequency fluctuations the interferometer is locked at the middle of the fringe, which corresponds to  $P_{out} = P$  corresponding to  $\sin(\Delta lk) = 1$ . Solving for  $d\omega$  gives

$$d\omega = \frac{dP}{P} \frac{2c}{\Delta l} \frac{P}{P_{pp}}. \quad (4.6)$$

The measured relative intensity noise PSD at the interferometer output is  $S_{\omega,I}(\Omega)$ . This also includes laser intensity noise  $S_I(\Omega)$ , which has to be subtracted from the measured noise power first, such that the actual frequency noise comes to

$$S_{\omega}(\Omega) = [S_{\omega,I}(\Omega) - S_I(\Omega)] \left( \frac{P}{P_{pp}} \frac{2c}{\Delta l} \right)^2 \quad (4.7)$$

with frequency noise PSD  $S_{\omega}(\Omega)$  in  $[\text{Hz}^2/\text{Hz}]$ , where equation 4.6 is used to convert a relative change in measured power  $dP/P$  into a frequency change  $d\omega$ .

**Noise measurement** The noise measurement is carried out on a dedicated measurement apparatus, that is depicted in figure 4.6a. It consists of two parts, one for intensity noise and one for frequency noise measurements. The intensity measurement part consists of a low frequency ( $\approx 1$  kHz) intensity stabilization, that keeps the average power level constant and feeds back via an AOM to the laser light coming from a fiber. An additional PBS is filtering the polarization, the first 50:50 beam splitter is dividing the power into frequency and intensity measurement. The frequency measurement part consists of the Michelson interferometer that is again stabilized to the fringe by a slow feedback on a piezo on one of the interferometers endmirrors, while the input power is also stabilized. The path difference is  $\Delta l = 0.96$  m. During a measurement, one of the paths is blocked to measure only one signal at the same time.

A measured sample is shown in figure 4.6b for the TaPro laser. The spectrum analyser background is normally flat but rises due to the filter function correction of the amplifiers, which is applied. The photo diode (PD) background is the dark photo diode noise level, that limits the sensitivity of the measurement. The frequency measurement noise level is always above the one for intensity, as the frequency measurement is sensitive to both noises. The narrow noise spikes are caused by the AOM driver and are not present on the laser itself. The dashed line represents the calculated shotnoise level, which shows that one is able to measure shotnoise

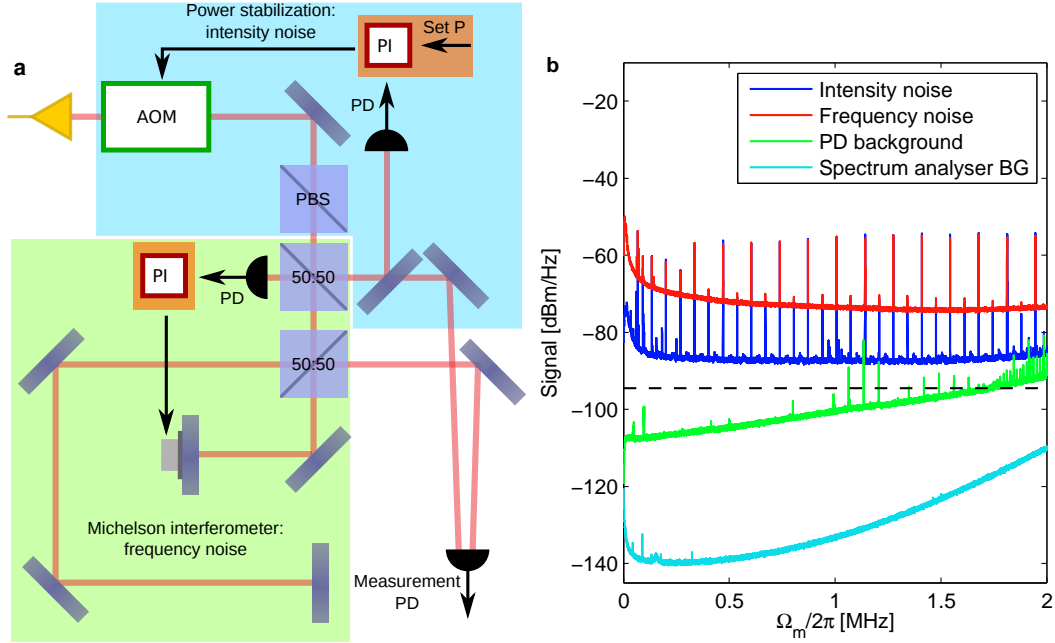


Figure 4.6: **a:** Apparatus for measuring laser amplitude noise and frequency noise using a michelson interferometer. **b:** Sample spectra recorded with the TaPro laser with a laser power of  $590 \mu\text{W}$  at  $\lambda = 780 \text{ nm}$ . The dashed line represents the calculated shotnoise level.

for this power over most of the frequency range. The total incident light power is  $P = 0.6 \text{ mW}$ , which translates with a gain of  $A = 5 \times 10^5 \text{ V/A}$  to a hypothetical DC electrical power of  $P_e = 240 \text{ W}$  or  $54 \text{ dBm}$ . The shotnoise level is then  $148 \text{ dB/Hz}$  below (equation 4.2). The measured noises get scaled afterwards to relative noises using this reference power level. In order to only analyse technical noise, one can subtract the calculated shotnoise from the measured signals.

**Laser frequency stabilization** In order to reduce frequency noise, which is the larger noise source in most cases, one can lock the laser to a stable high finesse cavity. This cavity is placed in vacuum on vibration isolation posts to reduce mechanical noise inside. The design of the cavity we use is shown in figure 4.7. The cavity is made out of Zerodur with ultra low thermal expansion and high reflectivity mirrors<sup>11</sup>. We have integrated a ring piezo<sup>12</sup>, which reduces the long term stability, but allows us to feed back the error signal of the  $\Delta$  stabilization on the cavity. To compensate the negative expansion coefficient of the piezo a thin metal plate spacer is used. The whole cavity is tilted  $8^\circ$  to the vacuum windows to avoid interference

<sup>11</sup>Layertec

<sup>12</sup>Piezomechanik GmbH, HPSt 150/15-8/3

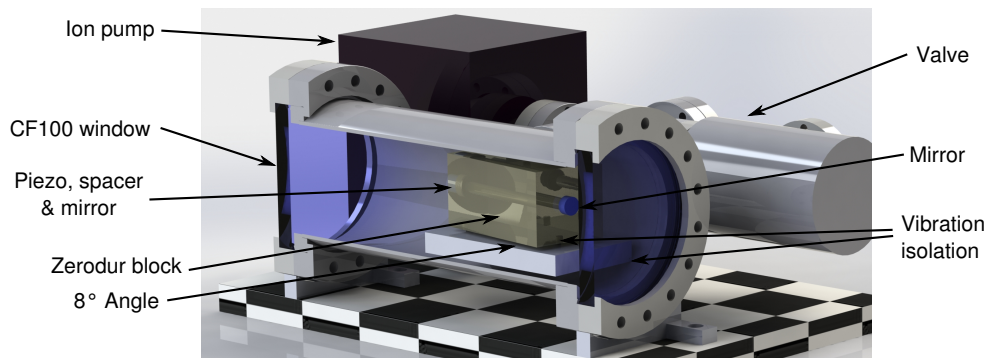


Figure 4.7: Schematics of Laser stabilization cavity

cavity length $L$	98.5 mm
mirror curvature $R$	500 mm
mirror reflectivity $r^2$	99.98%
mirror diameter	1/2"
free spectral range $\omega_{\text{FSR}}$	$2\pi \times 1.52$ GHz
linewidth FWHM $\kappa$	$2\pi \times 91$ kHz
fineness $\mathcal{F}$	16700

Table 4.2: Stabilization cavity parameters. The linewidth was measured as the intensity decay rate in a cavity ringdown measurement.

from reflections and the vacuum chamber is pumped by an Ion pump<sup>13</sup> to avoid vibrations. The cavity parameters are shown in table 4.2.

The laser stabilization to the cavity is carried out using a PDH locking technique. The sidebands are created at  $\omega_{\text{mod}} = 2\pi \times 20$  MHz using a resonant EOM<sup>14</sup>, collected on a fast photodiode<sup>15</sup>, mixed down<sup>16</sup> and fed back on the laser current and piezo using a fast lock<sup>17</sup>. To characterize the lock, we measured the spectrally resolved noise as shown in figure 4.8, where intensity and frequency noise PSD with and without the lock are compared. The spectrum shows the typical resonance above the stabilization bandwidth that is caused by the phase delay of the feedback circuit at large frequencies. The noise is reduced greatly at low frequencies, around  $\Omega_m$  there is still 8 dB reduction in the frequency noise power down to  $S_\omega(\Omega_m) = 4\pi^2 \times 256 \text{ Hz}^2/\text{Hz}$ . At the same time, the lock can enhance the intensity noise due to a crosstalk between laser frequency and power when modulating the current.

<sup>13</sup>Agilent VacIon Plus 20 Starcell

<sup>14</sup>Thorlabs EO-PM-R-20-C1

<sup>15</sup>Thorlabs SM05PD2A + Femto HCA-40M-100K-C with  $2 \times 10^3$  V/A gain

<sup>16</sup>Toptica PDD 110

<sup>17</sup>Toptica Falc 110

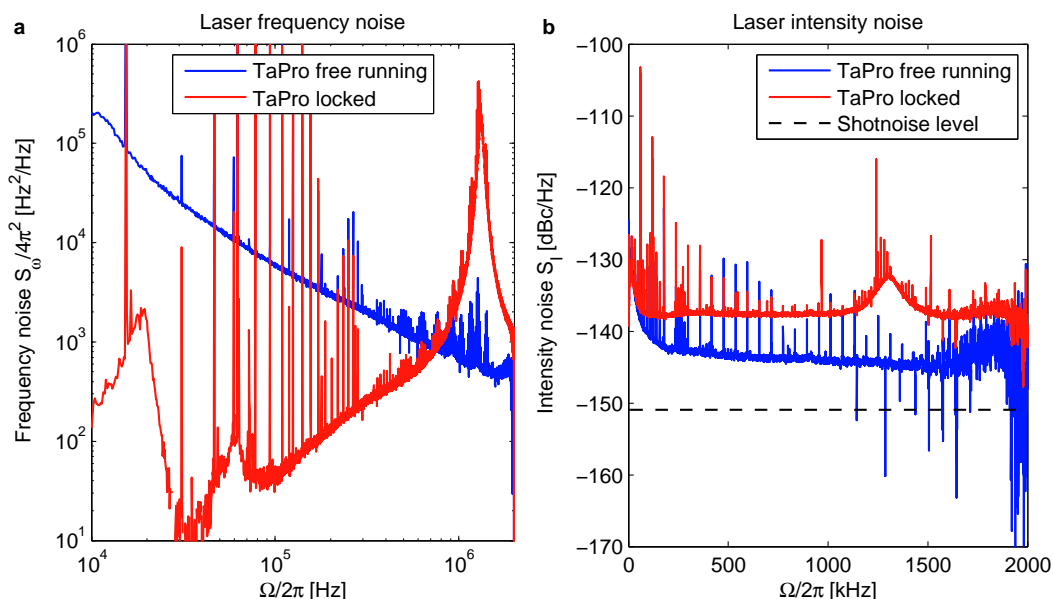


Figure 4.8: Comparison of **a**: laser frequency noise and **b**: intensity noise for the laser locked to the reference cavity and free running measured with  $545 \mu\text{W}$  of light. The frequency noise is reduced below 700 kHz, above 1 MHz the servo bump shows up. The intensity noise is increased by the locking procedure, as there is a crosstalk between frequency feedback and laser intensity. The peaks in the spectrum are caused by noise in the RF power in an AOM and are not present at the laser output.

While the frequency noise does not change with time and exact laser settings, the intensity noise depends strongly on the laser current and can differ by 10 dB without apparent change of the other laser properties. Furthermore, the intensity noise increases on the path from the laser to the experiment. Figure 4.9a shows the intensity noise spectrum after certain optical elements. The AOM for setting  $P_0$  increases the noise, which can be attributed to a noisy RF power driving the AOM. The fiber also increases the noise, which is again related to the AOM as the RF frequency noise modifies the laser beam pointing, leading to a modulation of the power coupled into the fiber. The minor increase after the polarization cleaning cube (not shown in figure 4.2) is due to polarization fluctuations. With active stabilization of  $P_0$  the noise increases further.

After this set of measurements, the setup has been improved by changing the AOM controller from the normally used homebuilt one to a dedicated series of components including low phase noise voltage controlled oscillator (VCO) as a source, a TTL switch and voltage controlled attenuator for power regulation and a low noise amplifier. In addition, the bandwidth of the feedback circuit was limited to  $\Omega = 2\pi \times 3 \text{ kHz}$ . The result is shown in figure 4.9b, where the intensity noise of

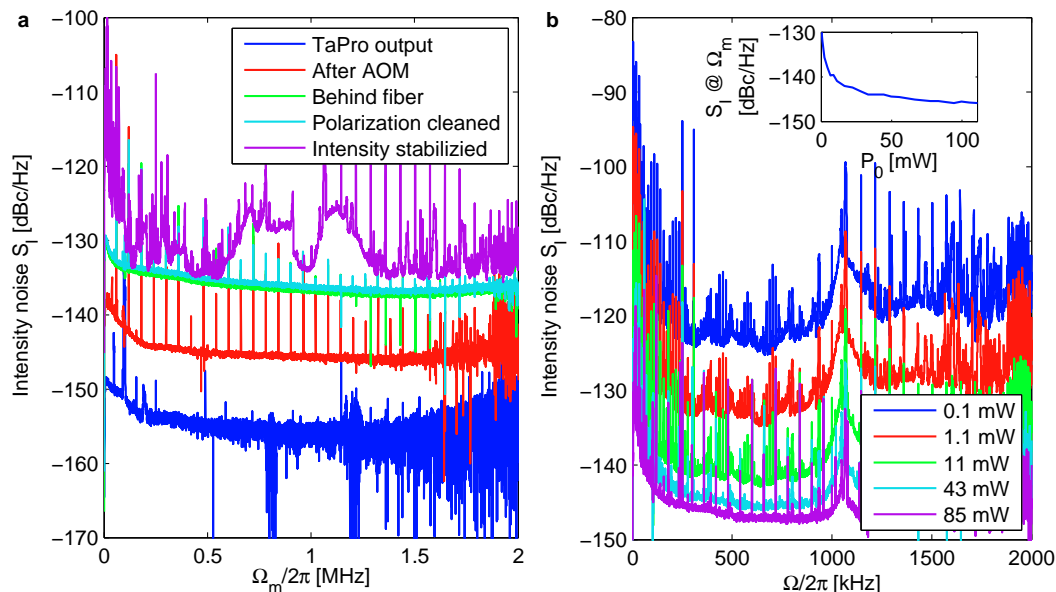


Figure 4.9: Relative laser intensity noise as a function of **a**: position along the laser beam and **b**: for different set powers at the experiment position after improvements. The inset shows the power dependent intensity noise at our membrane frequency  $\Omega_m$ . In all measurements, the shotnoise has been subtracted, such that the graphs show only technical noise

the stabilized system was measured in front of the experiment cavity. It is strongly dependent on power, but levels off for larger powers, where the noise is actually limiting the optomechanical cooling. The inset shows the noise level at the membrane frequency  $\Omega_m$  as a function of power.

As the noise is still dependent on the exact laser configuration, it has to be characterized and minimized before every measurement. The power dependent noise is then included into the theory fits in the cooling measurements.

### 4.3 Optomechanical measurements

In this section the optomechanical cooling and optical spring effects are used to study the performance of the membrane-cavity system. The measurements allow to determine the effective membrane mass, which depends on the overlap of the optical and mechanical modes. In addition, the bare membrane quality factor is determined.

#### 4.3.1 Membrane Q

The quality factor of the membrane was measured before inserting it into the cavity to be  $Q(1,1) = 3.25 \times 10^6$  at a frequency of  $\Omega_m(1,1) = 2\pi \times 273.93$  KHz for the

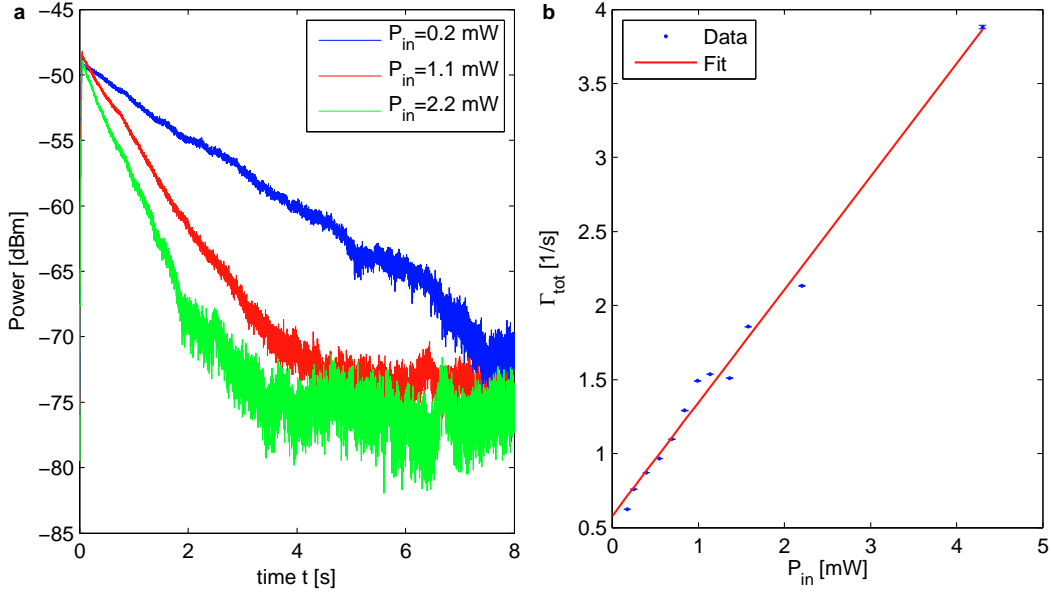


Figure 4.10: Optomechanical damping in membrane ringdown measurements. **a:** Sample time trace: the membranes are excited and the energy decaying is recorded as a function of optical power  $P_{in}$ . **b:** Evaluated total damping rate  $\Gamma_{tot}$  as a function of laser power. The linear fit is used to extrapolate to  $\Gamma_{tot}(0) = \Gamma_m$ .

fundamental mode,  $Q(2,1) = 4.125 \times 10^6$  at  $\Omega_m(2,1) = 433.3$  KHz for one of the (2,1) or (1,2) modes, and  $Q(2,2) = 7.47 \times 10^6$  at  $\Omega_m(2,2) = 547.2$  KHz for the (2,2) mode. These values were measured in the test chamber described in chapter 2 with the membrane glued to the cavities exchangeable mount. In the following, only the fundamental mode with lowest frequency is considered.

During the transfer of the membrane into the cavity the  $Q$  factor might have changed. To measure it inside the cavity, one has to take into account optomechanical effects that are always present. By measuring  $Q$  as a function of optical power, one can extrapolate to zero power to determine the bare membrane  $\Gamma_m$ , and therefore  $Q$ .

The decay rate  $\Gamma_m$  is precisely measured in ringdowns. The membrane is placed at the low finesse configuration of the cavity with a very low laser detuning  $\Delta < 0$ . It's motion is then excited using power modulation of the laser at the membrane frequency  $\Omega_m$ . Afterwards, the resulting decay rate is measured as the power decay rate of the membrane signal on the spectrum analyser in zero span in a bandwidth of 1 kHz around the membrane frequency as a function of cooling laser power. The membrane mode energy is proportional to the electronic power. The result is shown in figure 4.10a. Figure 4.10b shows the resulting power dependent damping  $\Gamma_{tot} = \Gamma_{opt} + \Gamma_m$ , with  $\Gamma_{opt} \propto P_{in}$ , as shown in equation 1.48. The fit is used to determine

$\Gamma_m = 0.58(4)/\text{s}$  or  $Q = 3.0(2) \times 10^6$  with a optomechanical damping coefficient  $\Gamma_{\text{opt}}/P_{\text{in}} = 0.76(2) \text{ mW}^{-1} \text{ s}^{-1}$ . This quality factor is slightly below the previously measured one and might be lowered due to exposure to dust in the air during the integration into the cavity.

### 4.3.2 Cavity cooling

In order to show that the observed increased damping during ringdown measurements leads to actual cooling, the membrane displacement spectrum  $S_x(\Omega)$  has to be measured, as it relates to the temperature as

$$T = \frac{M}{k_B} \int_0^\infty \Omega^2 S_x(\Omega) \frac{d\Omega}{2\pi} \approx \frac{M\Omega_m^2}{k_B} \int_0^\infty S_x(\Omega) \frac{d\Omega}{2\pi}, \quad (4.8)$$

see equation 1.13. In the experiment, the readout laser power is always kept constant and the membrane power spectrum is recorded in steady state as a function of cooling laser power and averaged over 20 measurements. A sample of the resulting averaged spectra is shown in figure 4.11a for different total powers  $P_{\text{in}}$  in front of the cavity with relatively large detuning  $\Delta = -0.12(2) \kappa$ , as determined by the reduced cavity transmission, and average  $G = 0.68 G_{\text{max}}$ . One can clearly see the optical spring shifting the membrane frequency and the damping increasing the peak width. The width is also enhanced by the noise of the  $\Delta$  stabilization, such that the optical spring is not constant, which leads to a broadening of the spectrum. The total noise power, which is proportional to the mode temperature, is calculated as the area of the recorded signal after subtraction of the background noise. The background noise of  $S_x^{\text{imp}} = 6 \times 10^{-14} \text{ m}/\sqrt{\text{Hz}}$  is three orders of magnitude higher than the theoretical limit of  $5 \times 10^{-17} \text{ m}/\sqrt{\text{Hz}}$  given by equation 1.65. The main cause is the low sideband power in the measurement, which can be improved by a homodyne or heterodyne detection scheme, as shown in the outlook.

The total measured temperature is plotted against  $P_{\text{in}}$  in figure 4.11b with the error as the standard error over 20 averages. The data shows a reduction of temperature up to  $P_{\text{in}} = 10 \text{ mW}$  followed by an increase for higher  $P_{\text{in}}$ . Using equation 1.48, 1.55 and 1.57 one can fit to the data a function

$$T_{\text{opt}} = \frac{c_1 T_0}{1 + c_2 P_{\text{in}}} (1 + c_3 P_{\text{in}}^2), \quad (4.9)$$

where  $c_1$  is the temperature calibration factor,  $c_2 = \Gamma_{\text{opt}}/(\Gamma_m P_{\text{in}})$  with  $\Gamma_{\text{opt}} \propto P_{\text{in}}$  and  $c_3 = T_L/(T_0 P_{\text{in}}^2)$  with laser noise temperature  $T_L \propto P_{\text{in}}^2$ . In order to determine  $c_1$  correctly, data points with  $c_2 P_{\text{in}} \geq 1$  have to be present, which shows up as a curvature in the fit function towards low  $P_{\text{in}}$ . The factor is then used to calibrate the temperature axis, which has a 18% systematic error. The statistical error on the low input power data points is dominated by the measurement time according to equation 1.19.

The laser noise is measured as a function of laser power as shown in the inset of figure 4.11b. The fitted value is a factor 1.2(5) larger, which is compatible within

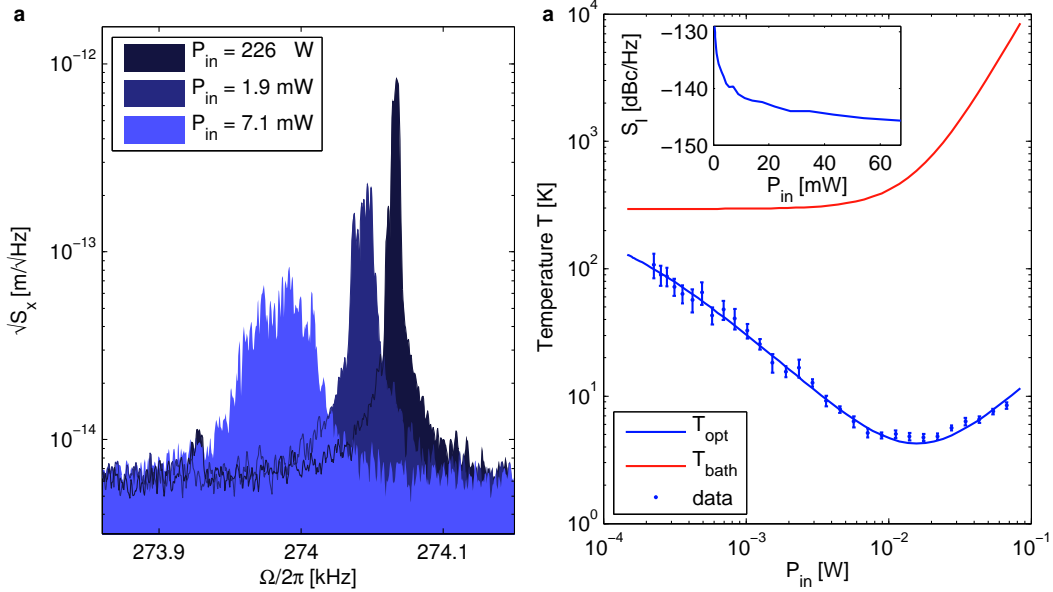


Figure 4.11: Optomechanical cooling data. **a:** sample spectra recorded for different total power levels. **b:** Mode temperatures calculated from spectra as a function of time, together with a fit to theory and the corresponding effective bath temperature.

the error. The corresponding effective bath temperature is shown in the main plot to illustrate the laser noise limitation of the reached temperature.

### 4.3.3 Effective membrane mass

From the measured optomechanical damping factor  $c_2 = 9(2)/\text{mW}$ , one can extract the effective mass, if the detuning  $\Delta$ , coupling constant  $G$  and incoupling efficiency  $\eta$  are known. For the measurement, one gets  $M = 140(40)$  ng. Errors on  $G$  and  $\eta$  are not included in the value, such that it can only be seen as an estimate. Especially the value of  $\eta$  represents an upper bound. This uncertainties in the individual factors are large, because they are harder to extract than the combined cooling factor, which is directly determined from the data.

The effective mass is a factor 2.2 higher than the minimum possible effective mass of  $M_{\text{phys}}/4$ , equivalent to an off-center displacement of the optical cavity mode by 0.39 mm on the  $l = 1.5$  mm membrane.

### 4.3.4 Optomechanical spring

From the data in figure 4.11 one can calculate the expected frequency shift  $\delta\Omega_m$  using the extracted damping  $\Gamma_{\text{opt}} = \Gamma_m(T_{\text{bath}}/T_{\text{opt}} - 1)$  and equations 1.52. The result is plotted in figure 4.12 together with the actual frequency shift as determined

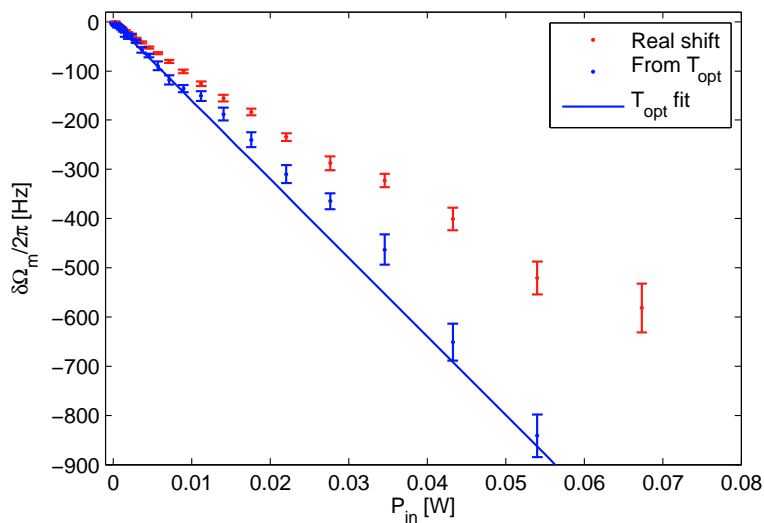


Figure 4.12: Optomechanical spring shift analysis: membrane frequency shift due to the optomechanical spring effect compared to the expected value from the temperatures  $T_{opt}$  using equations 1.54 and 1.55 including the fit curve. The difference can be removed by assuming a lower coupling efficiency for the readout beam into the cavity, as discussed in the text.

by the spectra. Their average ratio is 1.4. A value  $< 1$  would indicate additional frequency shifts, which would be caused by absorption of light as shown in section 2.2.1. The observed value  $> 1$  however is not allowed. It can be reduced to 1, if one assumes a lower incoupling efficiency of the readout beam of only 0.5 for this measurement. This also leads to an increased effective mass of  $m_{eff} = 160$  ng, which is within the error, and 20% higher temperature values. The measured frequency shift is  $\delta\Omega_m/2\pi P_{in} = -10.9(1)$  Hz/mW.

### *4.3. Optomechanical measurements*

---

## Chapter 5

# Coupled atom-membrane system

In this chapter, the optomechanical and atomic systems introduced in the previous chapters are combined to create a hybrid mechanical-atomic system. This system will in the following be used to sympathetically cool vibrations of the micromechanical membrane's fundamental mode with the atoms. The results presented in this chapter are published in [140].

### 5.1 System preparation

The coupled hybrid system consists of the optomechanical system introduced in chapter 4 with the only difference that ultracold atoms are trapped in the optical lattice given by the coupling beam, as can be seen in the bottom of figure 5.1.

In the experiment, the laser is locked to the red side of the cavity resonance ( $\Delta < 0$ ) with  $|\Delta| \ll \kappa$  in order to experience as little optomechanical damping as possible. In our system the optomechanical cooling is weaker than the sympathetic cooling and only lowering the sympathetic cooling data quality. A finite  $\Delta < 0$  is required to avoid an accidental drift to blue detuning  $\Delta > 0$  and the resulting instability of the system.

The membrane itself is placed at points of low or high finesse with maximum coupling constants. To counteract the membrane drift during the experiment, the membrane is shifted from the optimum point slightly against the drift direction, which ensures a coupling constant close to maximum over the whole experiment. The membrane motion amplitude is recorded using the readout beam.

The atomic system is prepared by loading a MOT as described in chapter 3 with the coupling beam at low power, such that the axial oscillation frequency in the created 1D optical lattice is  $\Omega_a(0) < \Omega_m$ . During the experiment sequence, the MOT is switched off and molasses cooling is used to cool down the atoms, damp their motion and keep them inside the optical lattice volume.

In order to enable the coupling during an experimental sequence, the coupling

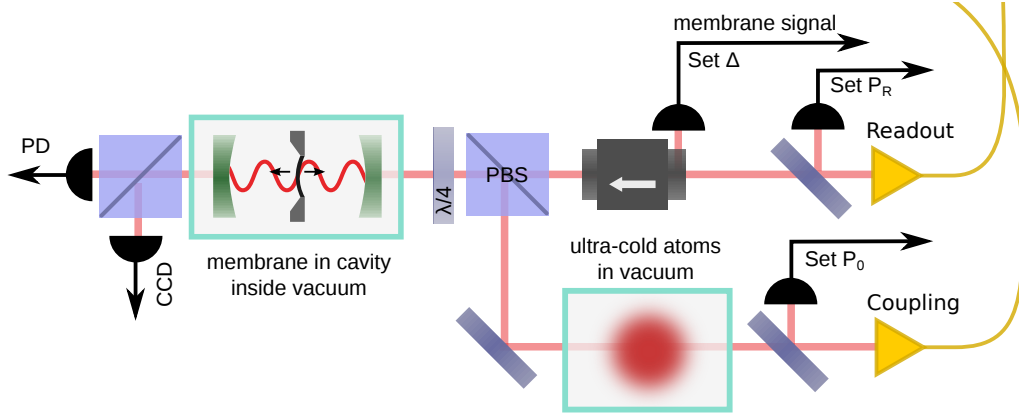


Figure 5.1: Hybrid system for atom-membrane coupling. The system is identical with the one presented in the optomechanics chapter 4 (figure 4.2) with the exception of the ultra-cold atoms being present in the coupling beam path. Readout and coupling beam are power stabilized and the laser-cavity detuning  $\Delta$  is stabilized using a PDH based scheme, which is also used to detect the membrane motion.

beam power is raised in order to increase the atomic oscillation frequency to  $\Omega_a(0) \geq \Omega_m$ .

## 5.2 Cooling in the time domain

In a first experiment, the membrane oscillation is recorded as a function of time within a bandwidth of  $BW = 2\pi \times 500 \text{ Hz} \gg \Gamma_{\text{tot}}$  around  $\Omega_m$  using the spectrum analysers zero span mode. In this way, the recorded signal is an integral over the membrane resonance peak in the PSD and thus proportional to the temperature of the membrane fundamental mode. The membrane is placed on the low finesse point with  $\mathcal{F} = 140$  and  $G = G_{\text{max}}$ . In figure 5.2a one can see the temperature change of the membrane during the experiment sequence for the case of atoms being present and without. In the beginning in phase A, a power  $P_0 = 5.5 \text{ mW}$  is applied and the atomic detuning is  $\Delta_{\text{LA}} = 2\pi \times 8 \text{ GHz}$ , such that  $\Omega_a(0) < \Omega_m$  and only optomechanical damping is present. The membrane is cooled down by pure optomechanical cooling in this phase while the atoms are prepared in a steady state MOT. In phase B, the optical molasses is switched on and shortly afterwards the coupling power is increased to  $P_0 = 16.5 \text{ mW}$ , such that the atomic oscillation is resonant with the mechanical one and the coupling leads to a strong damping and decrease of the temperature down to  $T_{\text{sym}} = 1.5(4) \text{ K}$  including calibration and measurement error. A fit to the initial decay gives  $\Gamma_{\text{tot}} = 111(1) / \text{s}$ . The sympathetic cooling corresponds to a damping  $\Gamma_{\text{tot}} = \Gamma_m T_{\text{bath}} / T_{\text{sym}} = 122(22) / \text{s}$ , which is compatible with the value determined from the decay. The following increase of temperature over time can

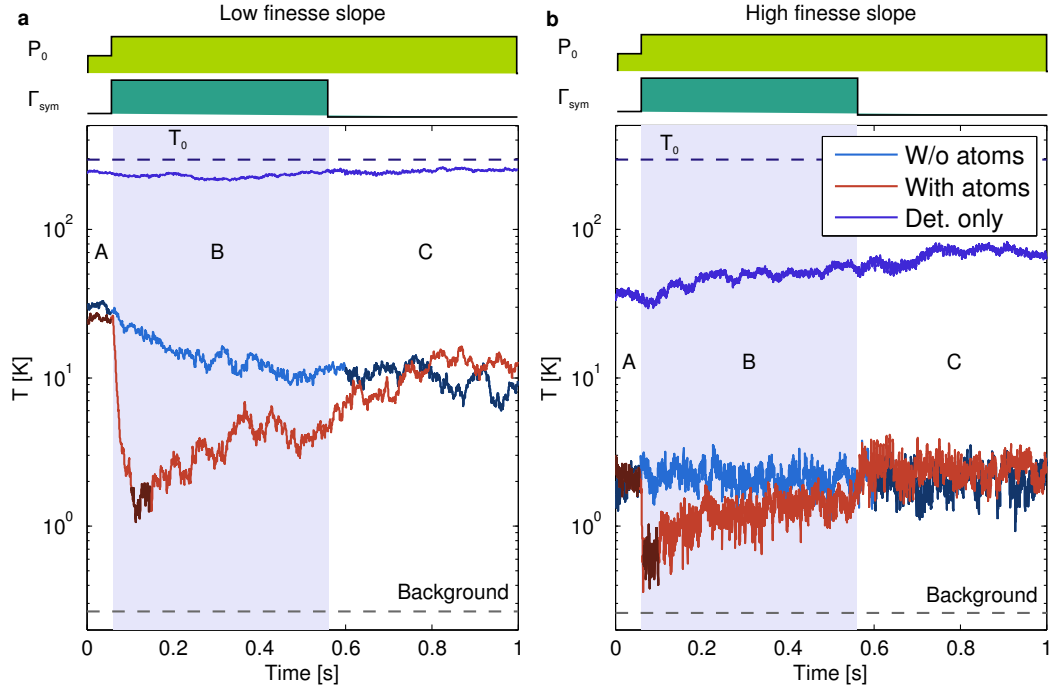


Figure 5.2: Time domain sympathetic cooling. The measurement sequence is divided into 3 phases and the traces show the temperature of the fundamental membrane mode during the measurement. In A, only optomechanical cooling is present. In B, the atoms are resonant and sympathetically cool the membrane. In C, the laser cooling of the atoms is switched off. The red and light blue curves only differ by the presence of the atoms, while in dark blue curve  $P_0 = 0$ . The measurement background, indicated by the dashed line, is subtracted from the curves and  $T_0$  represents room temperature. **a**: Traces for low finesse configuration with  $\mathcal{F} = 140$  **b**: Corresponding traces with high finesse  $\mathcal{F} = 300$ . The darker parts of the curves indicate the data taken to determine the temperature in the different phases.

be attributed to atom loss in the molasses with corresponding time constant. In a control experiment without any atoms, only an increased optomechanical damping  $\Gamma_{\text{opt}}$  can be observed and  $T_{\text{opt}} = 11(2)$  K is reached. The atoms are removed by tuning the MOT cooling light to positive detuning, which represents a minimal modification, such that none of the other system components are affected. In phase C the molasses is switched off, such that the atomic cooling  $\Gamma_a$  is switched off and the atoms are lost. The result is a reunion of both curves at the same temperature given by optomechanical cooling. The background, which was measured a few kHz next to  $\Omega_m$ , was subtracted for all curves (see figure 4.11a). In figure 5.2b one can see a similar measurement with a changed membrane position  $x_m$  to achieve a maximum finesse of  $\mathcal{F} = 300$ . Furthermore, the measurement bandwidth is increased to  $\text{BW} = 2\pi \times 2$  kHz and  $\Delta$  is increased slightly. One can see, that the optomechanical effects are stronger and already limited by laser noise, as the temperature increases in the curve without atoms with rising  $P_0$  in section B. The sympathetic cooling cools the membrane further with a decay rate  $\Gamma_{\text{tot}} = 331(30)$  /s to  $T_{\text{sym}} = 0.7(2)$  K including all errors, while  $T_{\text{opt}} = 2.2(8)$  K without sympathetic cooling. The measured  $T_{\text{sym}}$  corresponds to a damping  $\Gamma_{\text{tot}} = 535(191)$  /s, a bit larger than the value determined from the decay. The traces in both figures represent an average over 20 measurement cycles.

The temperature calibration is done using the temperatures reached in the pure optomechanical measurement for different power values. The data points used are the detection light power level and values for both  $P_0$  settings indicated by the darker regions in figure 5.2. The data points are shown in figure 5.3a and b for both measurements.

The low finesse  $T_{\text{opt}}$  curve in figure 5.3a was fitted using equation 4.9 without fitting to the laser noise, which was measured to be  $S_I(\Omega_m) = -145$  dBc/Hz and  $S_\omega(\Omega_m) = 4\pi^2 \times 256$  Hz<sup>2</sup>/Hz. The error in the temperature calibration is 22% as a result of 8% fit uncertainty and 20% error on the lowest power data point which effectively determines the calibration. This statistical error was determined using equation 1.19 taking thermal fluctuations and measurement duration into account. The calibration factor  $c_2$  leads to a detuning  $\Delta = -0.013(4)$   $\kappa$  using the previously determined parameters of  $M = 140$  ng and  $\eta^2 = 0.69$ .

The high finesse  $T_{\text{opt}}$  curve in figure 5.3b was fitted using equation 4.9 without temperature calibration factor  $c_1$ , as all data points show  $\Gamma_{\text{tot}} \gg \Gamma_m$ . The temperature calibration was therefore done using the low finesse calibration with  $c'_1 = (\mathcal{F}/\mathcal{F}')^2 c_1$ , as the motion readout sensitivity scales with  $\kappa$  and therefore  $\mathcal{F}$  around  $\Delta = 0$ , see equation 1.64. As an error the standard deviations of different calibration factors from various measurements used, which vary by 35% from day to day. This represents a conservative estimate, as the measurements were carried out directly after each other. The factor  $c_2$  leads to a detuning  $\Delta = -0.019(2)$   $\kappa$  and the noise obtained from  $c_3$  is  $S_I(\Omega_m) = -139$  dBc/Hz and  $S_\omega(\Omega_m) = 4\pi^2 \times 256$  Hz<sup>2</sup>/Hz.

Using measured  $T_{\text{opt}}$ ,  $T_{\text{sym}}$  and calculated  $T_{\text{bath}}$ , one can extract the sympathetic

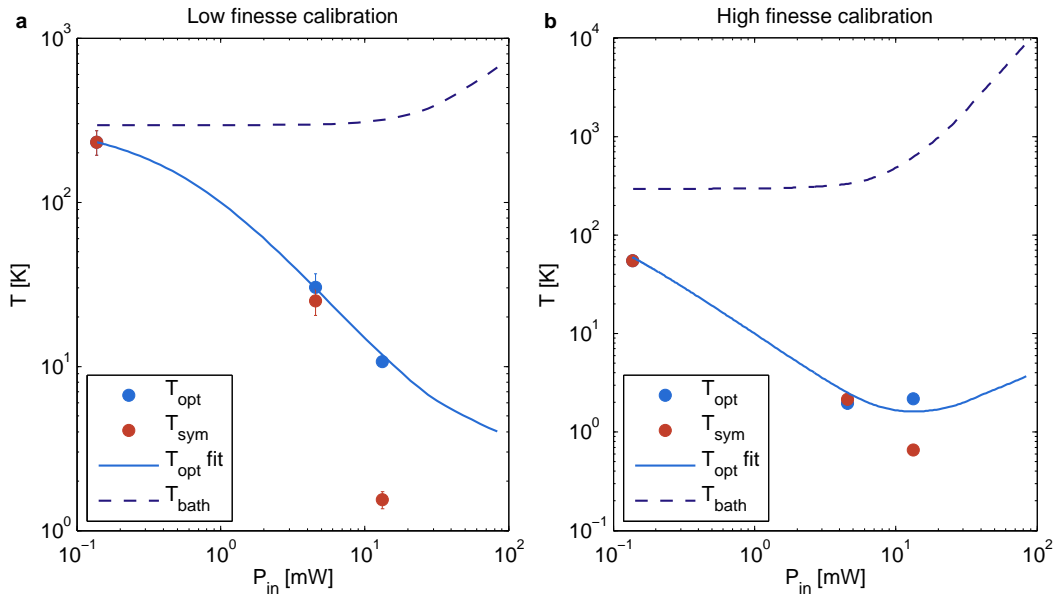


Figure 5.3: Time domain temperature calibration for measurements in figure 5.2. The data points correspond to values for readout power only, low  $P_0$  and high  $P_0$ , where the measurement region is indicated by the darker color in the traces in figure 5.2. The calibration curve is fitted to data points  $T_{\text{opt}}$ . The dashed line shows the effective bath temperature, calculated using the measured laser noise. The error bars are calculated using equation 1.19 in the theoretical analysis. **a**: Low finesse configuration and **b**: Corresponding traces with high finesse.

### 5.3. Cooling in the frequency domain

---

damping rate  $\Gamma_{\text{sym}}$  as

$$\Gamma_{\text{sym}} = \Gamma_m \left( \frac{T_{\text{bath}}}{T_{\text{sym}}} - \frac{T_{\text{bath}}}{T_{\text{opt}}} \right). \quad (5.1)$$

For the low finesse configuration a value of  $\Gamma_{\text{sym}} = 103(26)/\text{s}$  with  $T_{\text{bath}} = 320 \text{ K}$  and for high finesse  $\Gamma_{\text{sym}} = 390(138)/\text{s}$  with  $T_{\text{bath}} = 640 \text{ K}$  is calculated. The latter value corresponds to a coupling  $g_N = 1.3(2) \times 10^3 / \text{s}$  using equation 1.2 with  $\Omega_m = \Omega_a$ , which implies  $N_r = 9.1(3) \times 10^4$  resonantly coupled atoms using a measured  $\Gamma_a = 10^4 / \text{s}$ .

### 5.3 Cooling in the frequency domain

In this section the sympathetic cooling will be systematically investigated as a function of lattice power  $P_0$  to show the resonance characteristic of the coupling. Instead of recording a time trace, the membrane PSD is directly measured in a time window of 380 ms starting 12 ms after switching to molasses cooling. In addition, the power  $P_0$  is kept constant over each measurement and the membrane is set to the low finesse configuration with  $G = 0.92G_{\text{max}}$ , as the data is stronger influenced by laser noise and optomechanics otherwise. The result of a measurement with 40 averages per data point is shown in figure 5.4, again for two data sets with and without atoms in the system. The top right inset shows an average of the recorded spectra for three data points, which are indicated by the larger markers in the main figure. The width and asymmetry of the higher power measurements is due to instability of the small detuning  $\Delta$ , which leads to variations in the optical spring and cooling, and therefore to an asymmetric and broadened peak. One can also see that the sympathetic cooling introduces no additional frequency shift. The area under the peak represents the total power of the membrane mode, which is plotted as a function of  $P_0$  in the main plot of the figure after subtracting the background power level. The pure optomechanical temperature curve  $T_{\text{opt}}$  is fitted using function 4.9 and the temperature scale is calibrated using the fit with an uncertainty of 23%. The detuning is fitted to be  $\Delta = 0.028(4) \kappa$  and the fitted noise temperature of  $T_L/P_{\text{in}}^2 = 8 \times 10^5 \text{ K/W}^2$  is a factor 0.83(15) lower than the independently measured one, which is displayed in the lower left inset in figure 5.4. In this measurement, the minimum temperature is  $T_{\text{sym}} = 2.1(5) \text{ K}$  including the temperature calibration error, higher than in the previous measurement. This can be explained by the loss of atoms during the longer measurement time compared to the previous time domain measurements.

Using equation 5.1 and measured  $T_{\text{opt}}$ ,  $T_{\text{sym}}$  and calculated  $T_{\text{bath}}$  resulting from the fitted laser noise, the sympathetic damping rate  $\Gamma_{\text{sym}}$  is calculated and shown in figure 5.5 as a function of axial lattice frequency. The frequency axis was determined using the fit in section 3.7.4. One can see a step like behaviour of the coupling, starting around  $\Omega_a(0) = \Omega_m$ .

The resonance shape fits well with the model of constant atomic density in the trap region that is described in section 1.4.2. The constant atomic density is

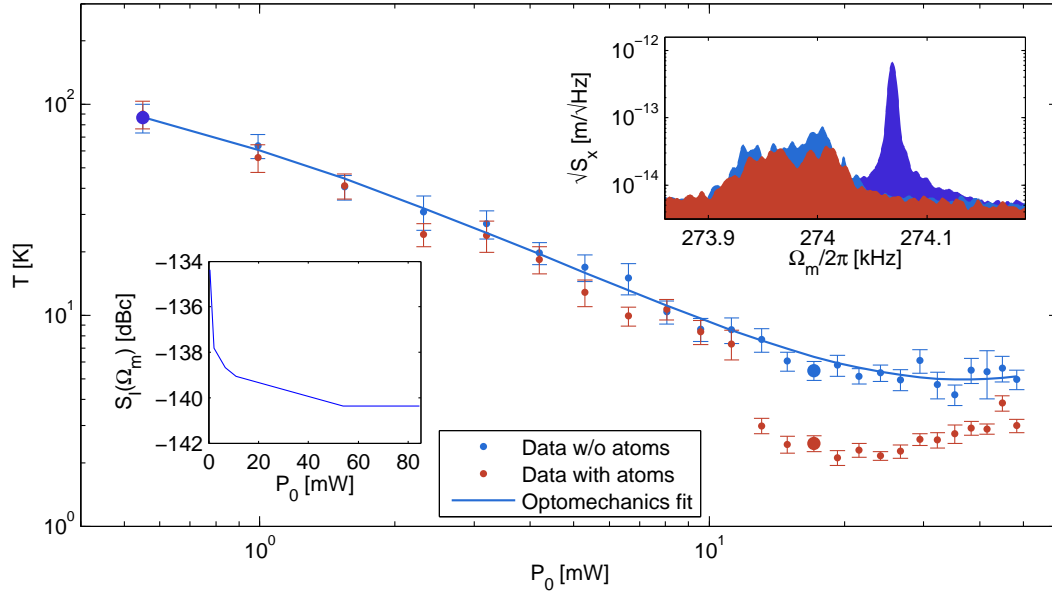


Figure 5.4: Sympathetic cooling compared to optomechanical cooling as a function of lattice power  $P_0$ . Spectra of the membrane mode noise power are recorded and the peak area is used to determine the mode temperature. Sample spectra are shown in the top right inset for the data points indicated by the thicker points in the main figure. The measured laser noise power for this measurement is shown in the lower left inset, also as a function of lattice power. The solid line is a fit to the optomechanical cooling using equation 4.9, which is used to calibrate the temperature axis.

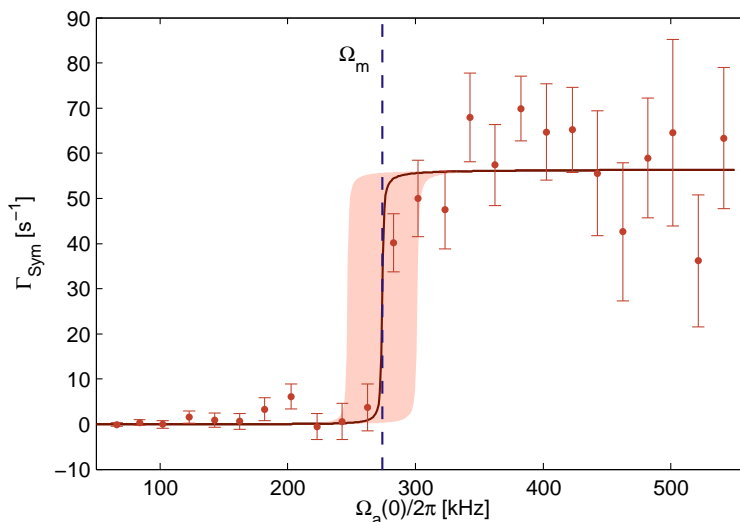


Figure 5.5: Atomic oscillation frequency dependent sympathetic cooling rate  $\Gamma_{\text{sym}}$ . The data is extracted from the data in figure 5.4. The fit curve corresponds to a model of constant atomic density  $n_a$  in the lattice. The shaded area resembles a 10% uncertainty in the calibration of  $\Omega_a(0)$ .

created by the optical molasses, which is damping the atomic motion. The resonance condition  $\Omega_a(r) = \Omega_m$  is therefore always fulfilled above the threshold  $\Omega_a(0) = \Omega_m$ , as atoms at larger radial position in the lattice get resonant at larger powers  $P_0$ , such that the resonance condition will be always fulfilled for some atoms inside the lattice. The data is fitted to the resonance equation 1.103. The shaded area represents a 10% error estimate of the choice of the lattice frequency calibration point. The only fit parameter is the atomic density  $n_a = 4.5(4) \times 10^{15} / \text{m}^3$  using  $R_a = 3.5 \text{ mm}$  and  $w = 284 \mu\text{m}$  that corresponds to  $\Gamma_{\text{sym}} = 57(5)/\text{s}$ . An independent measurement of the atomic density using absorption images resulted in  $n_a = 8.6 \times 10^{15} / \text{m}^3$ . The factor 0.5 difference probably originates from atomic loss during the measurement. The fitted atomic density corresponds to  $N_r = 6.6 \times 10^4$  resonantly coupled atoms, corresponding to a coupling constant  $g_{N_r} = 524 / \text{s}$  of the hybrid system.

### 5.3.1 Membrane absorption estimate

From the recorded spectra one can directly determine the power dependent frequency shift of the membrane with and without atoms. Alternatively one can determine the expected frequency shift from measured  $\Gamma_{\text{opt}}$ , see section 4.3.2.  $\Gamma_{\text{opt}}$  is extracted from the temperature measurement in figure 5.4 and shown in figure 5.6b. Figure 5.6a shows the measured frequency shift of the two data series with and without atoms and the expected shift based on  $\Gamma_{\text{opt}}$  using equation 1.54. Both data series show the same frequency shift, while the expected shift is slightly lower. The difference

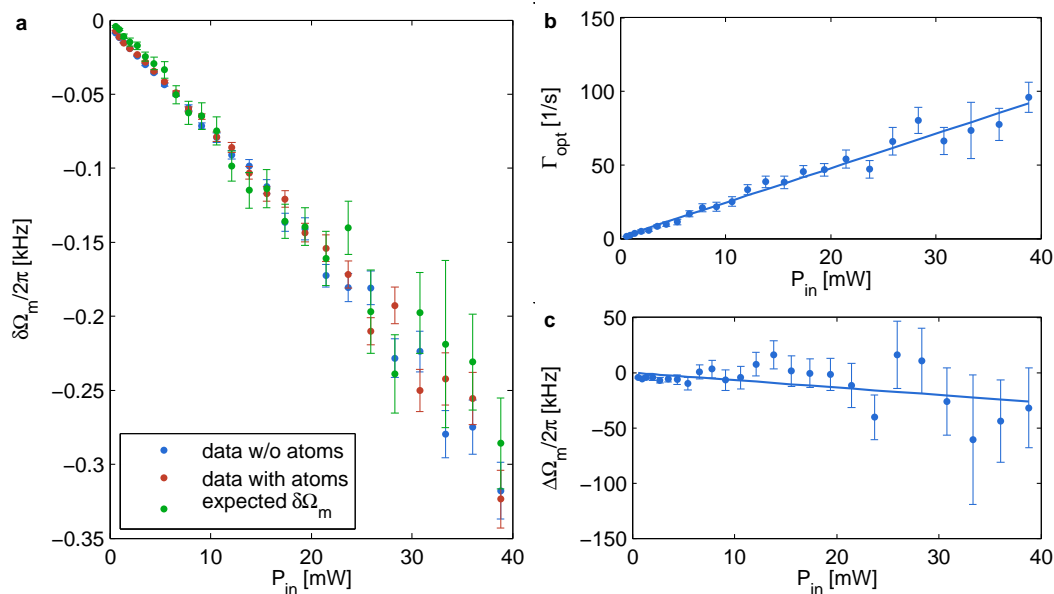


Figure 5.6: **a**: Membrane frequency shift as a function of  $P_{in}$ : Directly measured values compared to the expected value based on measurements of  $\Gamma_{opt}$  **b**: Extracted  $\Gamma_{opt}$  from temperature measurement **c**: Difference in frequency shift and expected value.

caused by the absorption of light induced membrane heating is shown in figure 5.6c with a fit of  $\Delta\Omega_m/P_{in} = -2\pi \times 0.8(2)$  kHz/W. This corresponds to a value of  $\Delta\Omega_m/P = -2\pi \times 7(2)$  Hz/W with respect to the power hitting the membrane  $P = 4\mathcal{F}\eta^2 P_{in}/\pi$  ( $2\times$  circulating power).

Under the assumption of the same expansion coefficient as low-stress membranes one can calculate a power absorption of  $a = 4 \times 10^{-6}$  for  $\lambda = 780$  nm corresponding to an imaginary part of the refractive index of  $\text{Im}(n) = 4 \times 10^{-6}$ . This values can only be seen as a rough estimate, as the difference in expected and real frequency shift can for example be influenced by a lower readout beam incoupling efficiency. For an assumed reduced  $\eta^2 = 0.5$  for the readout beam like in the previous chapter, the resulting absorption rises to  $\text{Im}(n) = 8 \times 10^{-6}$ , while other parameters of the measurement only change within their error.

## 5.4 Ringdown measurements: Atom detuning dependency

To prove the theoretical description of the membrane coupling to the atomic motion inside the lattice, the influence of the atom-light detuning on the resonance condition is measured. The atomic oscillation frequency depends on atom-light detuning  $\Delta_{LA}$

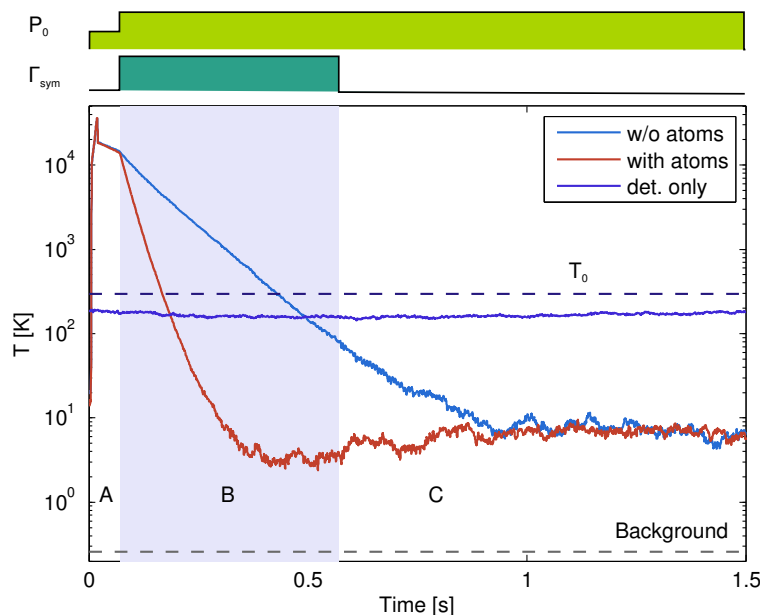


Figure 5.7: Sympathetic cooling of the membrane mode in time domain ring-down measurements. In contrast to figure 5.2, the membrane motion is excited in the beginning of phase A in order to be able to measure the damping rates directly. The minimum reached temperature of  $T_{\text{sym}} 3.3 \text{ K}$  is higher and the damping lower, which is probably caused by loss of atoms due to the large excitation during the longer cooling time before reaching the minimum temperature.

as  $\Omega_a(0) \propto \sqrt{P_0/\Delta_{\text{LA}}}$ . The sympathetic damping rate is therefore measured as a function of power  $P_0$  for different  $\Delta_{\text{LA}}$ . Here, ringdown measurements of an initially excited membrane are used in order to extract the cooling rates more easily in time domain measurements. the membrane motion is excited using an intensity modulation of the readout beam. Figure 5.7 shows the same sequence as figure 5.2a, but with initial excitation. In the plot, the same calibration value as in figure 5.2 has been used. The slopes in phase B show again the additional sympathetic cooling. The sympathetic damping rate can be determined to be  $\Gamma_{\text{sym}} = \Gamma_{\text{tot}} - \Gamma_{\text{opt}} - \Gamma_m = (40.5 - 10.5 - 0.58) / \text{s} = 30.4 / \text{s}$ . A temperature of  $T_{\text{sym}} = 3.4(12) \text{ K}$  is reached assuming the same calibration as in figure 5.2a. The expected value for  $T_{\text{bath}} = 320 \text{ K}$  and  $\Gamma_{\text{tot}} = 40.5 / \text{s}$  is  $4.6 \text{ K}$ , which is within the calibration error. The lower cooling performance compared to the previous measurements without excitation is probably caused by the strong excitation of the membrane, which heats trapped atoms out of the lattice, and atom loss during the longer ringdown time. However, this can only have an effect on the amount of damping, but not the threshold behaviour. This method does therefore not show the best possible system performance, but represents a much simpler way to determine  $\Gamma_{\text{sym}}$ .

In figure 5.8a, the measured sympathetic cooling rate is shown as a function of

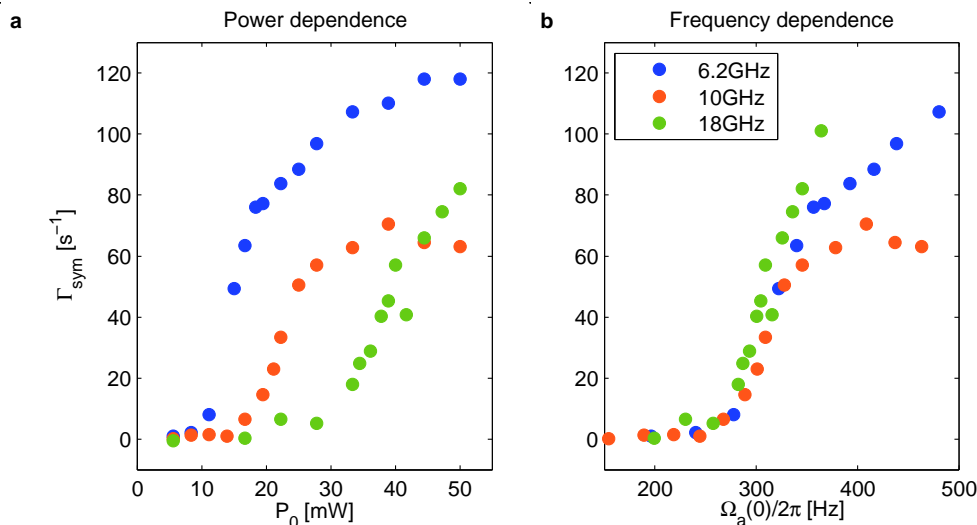


Figure 5.8: Atomic detuning dependent sympathetic cooling **a**: power dependent plot of sympathetic cooling for different detunings  $\Delta_{\text{LA}}$  **b**: corresponding plot in dependence of central atomic frequency

$P_0$  for three different detunings  $\Delta_{\text{LA}}$ . From the power and detuning, the atomic oscillation frequency can be extracted using equation 1.77 and the fit in section 3.7.4. The resulting sympathetic cooling rate as a function of oscillation frequency are plotted in figure 5.8b.

As one can see, the step in  $\Gamma_{\text{sym}}$  appears at different power levels for different detunings, but at the same axial center trap frequency. This can only be explained by a motional coupling to the atoms.

## 5.5 Conclusions

In the measurements presented in this chapter, sympathetic cooling is the dominating damping mechanism of the mechanical oscillator and cooled a micro-mechanical membrane mode to a temperature of  $T_{\text{sym}} = 0.7(2)$  K, where pure optomechanical cooling only reaches  $T_{\text{opt}} = 2.2(8)$  K. The corresponding maximum cooling rates are  $\Gamma_{\text{sym}} = 390(138)/\text{s}$  with  $g_{N_r} = 1.3 \times 10^3/\text{s}$  and  $N_r = 9.1 \times 10^4$ , while  $\Gamma_{\text{opt}} = 169(60)/\text{s}$  for pure optomechanical coupling. Although the small  $|\Delta| \ll \kappa$  is not optimal for pure optomechanical cooling, equation 1.60 suggests that the minimum reachable temperature is  $T_{\text{opt}} = 1.5$  K with the system at the present level of laser noise, still higher than the sympathetic cooling result. For sympathetic cooling, the reachable temperature is also limited by  $T_{\text{bath}}$  and therefore laser noise. In terms of phonons the reached temperature corresponds to  $\bar{n} = 5.3 \times 10^4$  while the thermal occupation is  $\bar{n}_{\text{th}} = 2.2 \times 10^7$ .

In this system, the mass ratio of the membrane and resonantly coupled atoms is

## 5.5. Conclusions

---

$M/N_r m = 10^{10}$ . Still, the light mediated coupling cools the membrane by a factor of 450 from room temperature. Similar cooling factors and final temperatures were reached in other experiments [52] on sympathetic cooling of large molecular ions. However, the maximum mass ratio was only  $\approx 90$ .

To characterize the regime, in which the system is operating, the cooperativity is a suitable figure of merit. It is  $C = 4\eta^2 t^2 g_N^2 / \Gamma_m \Gamma_a$  (equation 1.110) and can be calculated using equation 1.2 and the measured rates as

$$C = \frac{\Gamma_{\text{sym}}}{\Gamma_m}. \quad (5.2)$$

For the time domain measurements presented above, the maximum cooperativity is  $C = 103$  for the low finesse and  $C = 672$  for high finesse. For effects like EIT a value  $C > 1$  is sufficient, which is the case. The condition for groundstate cooling is  $C > \bar{n}_{\text{th}}$  [47], which is in this experiment still far from being fulfilled.

Depending on the application, inhomogeneous broadening of  $\Gamma_a$  and optomechanical damping  $\Gamma_{\text{opt}}$  have an effect on these conditions. For EIT, optomechanical damping  $\Gamma_{\text{opt}}$  increases the effective membrane linewidth  $\Gamma_m$ . Furthermore, the atomic linewidth  $\Gamma_a$  is strongly broadened by the constant atom density  $n_a$ , that leads to different oscillation frequencies within the trap. In order to observe EIT, the atomic linewidth has to be reduced. For groundstate cooling, the additional  $\Gamma_{\text{opt}}$  and broadening of  $\Gamma_a$  do not play a role, as  $\Gamma_{\text{opt}}$  only contributes further to the cooling and neither does the broadening of  $\Gamma_a$ , as it is already included in  $g_N$  via the resonantly coupled atom number  $N$ .

## Chapter 6

# Conclusions and outlook

In this thesis a hybrid system was built, that couples the motion of atoms trapped inside an optical lattice to the motion of a membrane inside an optical cavity. In this context, a new apparatus for trapping ultra-cold atoms was built that is capable of trapping  $1.6 \times 10^9$  atoms and cooling them to  $40 \mu\text{K}$  using an optical molasses. The fundamental properties of silicon nitride membranes were investigated using a novel technique for *in situ* tuning of the membrane frequency. The optomechanical system of a membrane inside an asymmetric cavity was also built and used for optomechanical cooling. There, the limitation of the final temperature due to laser noise was analysed and optimized.

Using this hybrid system, the motion of a single membrane mode with frequency  $\Omega_m = 2\pi \times 274 \text{ kHz}$  was sympathetically cooled to  $0.7 \text{ K}$  starting from room temperature. The sympathetic cooling rate is stronger than the well-known optomechanical cooling rate and the final temperature is limited by laser noise. The system offers a cooperativity  $C > 1$ , which will allow for observation of coherent effects in the coupled system like EIT. While there are many theory proposals, this results represent the first experiment, in which the back-action to a massive mechanical oscillator is strong enough to be useful for cooling and other applications. In our previous experiments, the coupling was limited to the detection of the back-action as a small modification of the oscillator damping[15], which was already an amazing result. Now, this experiment has shown that it is possible to use this coupling mechanism for significant cooling. Theory estimates show that the system is capable of ground state cooling of low frequency mechanical oscillators.

In the future, this system will be improved in all parts in order to boost the cooling, lower the membranes initial photon occupation and reduce laser noise, which will enable ground-state cooling. The system is operating in a regime, where optomechanical cooling cannot reach the groundstate, as the resolved sideband condition is not fulfilled, and active feedback cannot either because the optomechanical cooperativity  $C_m = 4g_0^2 \bar{n}_c / (\Gamma_m \kappa) < n_{\text{bath}} / 8$  is too small [47]. Once in the groundstate, the flexibility of the atomic systems allows to switch off the atomic damping to reach the strong coupling regime [45]. In addition, the coupling scheme can be changed

to address the internal atomic states [38, 141] instead of the motional ones, which decouples the optical power and atomic oscillator frequency. This will allow us to use higher mechanical frequencies, which increases the coupling and ground state energy, thus lowering the ground-state cooling requirements. The main advantage is the preparation and exchange of non-classical states, which can be created using internal atomic states with high fidelity. The collective spin of the atomic ensemble could be coupled to the membrane vibrations in a very similar setup, by transducing the membrane vibrations into a polarization change of the light field [38]. Such a system has been proposed to create Einstein-Podolsky-Rosen (EPR) entanglement between the systems. This EPR entanglement can be used to measure the membranes trajectory with reduced quantum uncertainty [142].

On a long term perspective, groundstate cooled oscillators and creation of superposition states can be used for testing speculative theories on gravity induced wavefunction collapse of massive objects [1, 2] and therefore investigating the limits of quantum mechanics [143]. In the context of quantum information processing mechanical systems are suitable as transducers between different systems, which are either advantageous for storage, processing or transport of quantum information. Recently, first experiments on transformation of microwave to optical signals have been performed [31, 32]. The atomic system could be used to store quantum information and use the membrane as a connection to other systems. On the atomic side, a quantum dot at the atomic transition frequency could be entangled to the atomic system storing the emitted photons [105] or the dot could be used to prepare single excitations in the atoms by photon storage.

The membrane oscillator in the current system is not a necessity, as any system with optomechanical coupling and reflection of laser light can be used in the presented coupling scheme. Levitated nano-particles [6, 7, 8, 144] are an alternative system, which can offer very high mechanical quality factors and oscillation frequencies within our accessible frequency range. In addition, the coupling is strongly enhanced due to the lower mass ratio. Another possibility are integrated optomechanical cavities and photonic crystals, which show much higher coupling strength and frequencies, such that an internal states coupling scheme would be required. A drawback of these systems might be the enhanced light absorption [145].

These mentioned future experiments and improvements, which are partially already implemented, will be addressed in the following in more detail.

## 6.1 Improved optomechanical cavity

The optical cavity presented in this theses proved to be sensitive to low frequency vibrations caused by the undamped mounting and positioners that were not stiff enough. A new cavity has therefore been designed to address these issues. The improved stability is achieved by removing the unnecessary alignment degrees of freedom and shrinking the cavity length, as it has no effect on the membrane-atom coupling. The whole miniaturized cavity is shown in figure 6.1. It consist of two mir-

rors separated by only 1 mm with a membrane in between. To tune the cavity and membrane position, two piezos are integrated on each side of the membrane. The top and bottom plate of the construction is made of titanium, while the 0.4 mm thin membrane holder is made of aluminium for easier fabrication. The whole construction is glued together during alignment, which is critical, as it cannot be changed afterwards. In the alignment, the placement of the holder determines the optical mode position on the membrane, while the top mirror alignment has to ensure that the optical mode is perpendicular to the membrane. A misalignment leads to additional losses and coupling between optical modes. For larger finesse values, this can become limiting. To make the cavity insensitive to outside vibrations, it is placed onto a two stage vibration isolation inside vacuum, which consists of heavy steel cylinders, that are resting on isolating viton rods. The compact design with a footprint of only  $(25 \text{ mm})^2$  is also compatible with a future cryostat, which is required for ground-state cooling.

A prototype cavity has been assembled with a maximum finesse  $\mathcal{F} = 400$  and length  $L = 1.1 \text{ mm}$ , mirror radius  $R = 30 \text{ mm}$  and reflectivities  $r_1^2 = 98\%$  and  $r_2^2 > 99.99\%$  [146]. In addition, an improved readout has been implemented using homodyne detection. There, the cavity readout beam is overlapped with a strong optical beam to increase the signal strength. An uncalibrated sample spectrum was shown in figure 2.2. There, laser frequency noise is still an issue, but can in principle be eliminated by matching the optical path lengths of both beams. The disadvantage of the homodyne technique is the inability to separate positive and negative frequency components of the signal, which represent stokes and anti-stokes processes. The absence of anti-stokes processes indicates the resonator being in the groundstate [137]. By switching to a heterodyne scheme, which can easily be done, the negative frequency components will become accessible. As the cavity is much shorter, the resonances broaden with increased  $\kappa$ , which leads to a reduced effect of laser frequency noise on the membrane (equation 1.58), but also to an reduced optomechanical damping as described by equation 1.53. On a technical level, the increased  $\kappa$  requires larger modulation frequencies  $\Omega_{\text{Mod}}$  for the PDH-stabilization of the cavity detuning. The passive stability was greatly enhanced by the new vibration isolation.

Using this cavity also enables to feed back the detuning stabilization onto the cavity's piezo, such that the laser frequency can be kept constant relative to the atomic transition frequency thus allowing for lower stable detunings  $\Delta_{\text{LA}}$  during a measurement.

## 6.2 Transverse lattice

The short lifetime of the atomic cloud is partially caused by density dependent losses, for example light assisted collisions. Adding an additional transverse lattice to the existing coupling lattice allows to isolate all atoms from each other, thus preventing this loss channel. This enables lower coupling lattice detunings  $\Delta_{\text{LA}}$ , as the described

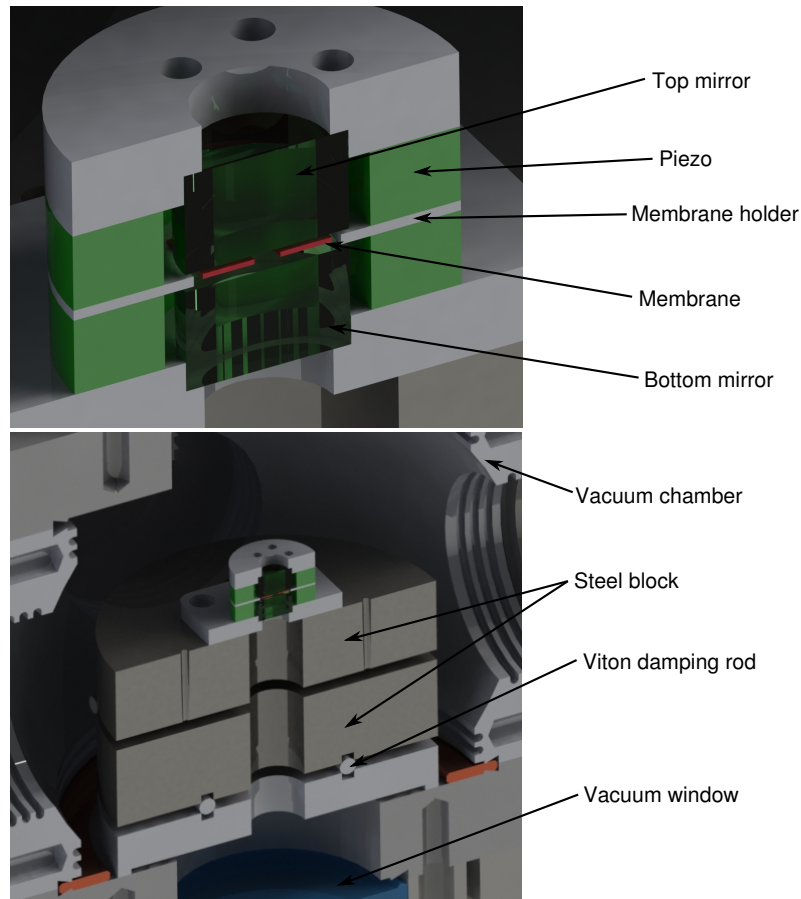


Figure 6.1: Design of the improved optomechanical cavity. The cavity is built monolithically and only tuned via two piezo elements in the two sub-cavities above and below the membrane. The components are aligned while glueing them together. The cavity's base plate measures only 25 mm side length and is therefore compatible with typical cryogenic systems. The whole cavity is mounted on a vibration isolation assembly consisting of large masses connected by viton rods. The top steel block is wedged by  $2^\circ$  to prevent interference with reflections on the vacuum windows.

collisional loss scales with the time spent in the electronic excited state and therefore scattering rate and lattice detuning. The lower detuning results in lower optical powers needed to create the coupling, such that the membrane heating by laser noise and radiation pressure shot noise on the membrane is lowered. To counteract heating of the atoms due to the scattered light, the tight three-dimensional confinement allows to apply raman sideband cooling [147] to the atoms to bring and keep them in the vibrational ground state during the coupling. With the additional trapping lattice a blue-detuned coupling lattice  $\Delta_{La} > 0$  is stable and shows reduced light scattering by trapping the atoms in intensity minima.

As an additional reward, the transverse lattice will prevent diffusion of atoms when applying molasses cooling, such that a compressed atomic cloud with much higher atomic density can be used, resulting in a stronger coupling.

### 6.3 Groundstate cooling estimate

In the presented system a minimum phonon number of  $n_{ss} = 5 \times 10^4$  was reached cooling down from an effective thermal bath occupation of  $n_{th} = 4 \times 10^7$ . A series of improvements have to be implemented to reach the groundstate  $n_{ss} < 1$ . In addition to the mentioned improvements on the cavity and transverse lattice, the membrane-cavity system will be placed in a cryostat in order to get closer to the ground state to begin with. In this estimate, a simple cryostat at liquid helium temperature  $T_0 = 4$  K is used. The lower thermal bath temperature also requires lower effective laser temperatures  $T_L$ , as the relative influence increases. The increased cavity  $\kappa$  leaves the laser frequency noise negligible compared to the amplitude noise, where a reasonable improvement by factor ten to  $S_I(\Omega_m) = -156$  dBc/Hz is assumed. A lower temperature cryostat is not useful, as the Laser temperature already dominates the effective bath and laser absorption is expected to heat the mechanical system, too [45]. The mentioned reduction of atomic detuning to  $\Delta_{LA} = 2\pi \times 0.5$  GHz leads to a reduced optical power on the membrane for creating the same oscillation frequency, also relaxing the laser noise limitation. In addition, a higher atomic density of  $n_a = 2 \times 10^{17} / \text{m}^3$  is assumed, which is possible due to the 3-D lattice confinement.

For an additional optimization the Finesse, lattice beam waist and mechanical frequency can be adjusted. A realistic limit for the mechanical frequency is around  $\Omega_m = 2\pi \times 1$  MHz, which is close to the  $\Omega_{4,4}$  mode of our membrane, which can show quality factors up to  $Q = 4 \times 10^7$  at room temperature [92], which is expected to stay the same or improve towards cryogenic temperatures [77]. The higher frequency lowers the required cooling factor, as the ground state energy  $\propto \Omega_m$  increases, and also increases the sympathetic damping  $\Gamma_{\text{sym}} \propto \Omega_m^2$ , thus almost compensating for the increased laser bath temperature  $T_L \propto \Omega_m^4$  due to the increased power requirement  $P_0 \propto \Omega_m^2$ . Together with the higher Q, this value of  $\Omega_m$  is optimal. The finesse and lattice beam waist are connected for fixed optical power at the membrane. The cooling rate depends on these parameters as  $\Gamma_{\text{sym}} \propto N_r \propto w^2$

at fixed atomic density and  $\Gamma_{\text{sym}} \propto \mathcal{F}^2$  and the power on the membrane scales as  $P = \mathcal{F}w^2$  under resonance condition, such that lower beam waists and larger finesse values are favourable. In the optimization  $w = 100 \mu\text{m}$  and  $\mathcal{F} = 1000$  lead to laser temperatures comparable to  $T_0$  in the coupled system, while the Rayleigh length is still longer than the atom cloud radius  $w_0 \gg R_a$ .

As a last optimization higher efficiencies  $t^2 = \eta^2 = 0.9$  are assumed together with an improved mode overlap, leading to a minimum effective mass  $M = 63.5 \text{ ng}$ . The measured absorption of  $a = 4 \times 10^{-6}$  is used and a reduced thermal conductivity  $\kappa = 3 \text{ K/sm}$  at  $T_0$  is assumed, estimated from the high stress  $\text{Si}_3\text{N}_4$  room temperature value [84] and extrapolated to  $T_0$  using the low-stress temperature dependence [81]. All the mentioned parameters put together lead to a final minimum occupation of  $\bar{n}_{ss} = 0.3$ , thus reaching the ground state. The calculation is visualized in figure 1.6.

## 6.4 Coupling to internal states

The coupling to motional states has some disadvantages. The atomic frequency in optical traps is usually limited to values of  $\Omega_a = 2\pi \times 1 \text{ MHz}$  and lower and directly connected to the optical power. Another difficulty for the perspective of transfer of non-classical states is the addressability of these states by optical manipulation of the atoms. A coupling scheme that addresses the energy splitting between two internal atomic states would overcome these issues. Higher mechanical oscillator frequencies raise the ground state energy and therefore lower the required cooling and make it possible to use very different optomechanical systems like photonic crystal nano beams [13]. The preparation of non-classical superposition states is used in many applications like Ramsey interferometry [129], while single excitations can be excited in the atomic cloud using quantum memory schemes [106] or using Rydberg blockade effects [148]. The question of implementation of such a coupling scheme is currently under investigation. A recent proposal offers a possible experiment configuration [141] for this system, while further reaching proposals create EPR entanglement between the systems [38, 142].

## 6.5 Opto-mechanically induced transparency

The presented system's cooperativity  $C > 1$  enables coherent effects like electromagnetically induced transparency (EIT) [75, 76], which for optomechanical system has been achieved and is referred to as opto-mechanically induced transparency (OMIT) [149, 150]. The coupling in our hybrid system is not between two atomic levels or optical and mechanical excitation, but atomic and mechanical excitation, resulting in an EIT-like interference effect between mechanical modes. A possible experiment would be the suppression of atomic motional excitation if on resonance with the membrane oscillator.

## Appendix A

# Experiment photographs

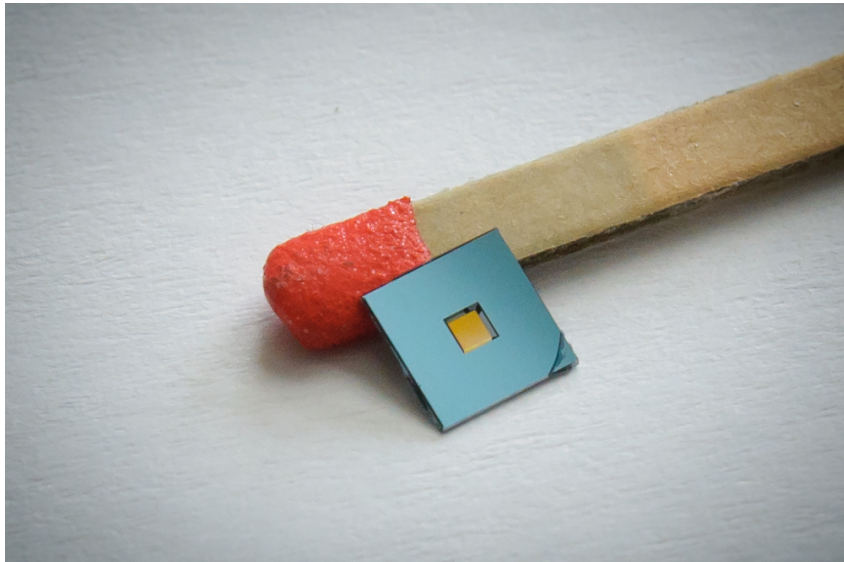


Figure A.1: Low stress silicon nitride membrane with 1 mm side length and 100 nm thickness on a silicon frame. The colors are dependent on the illumination and viewing angle.

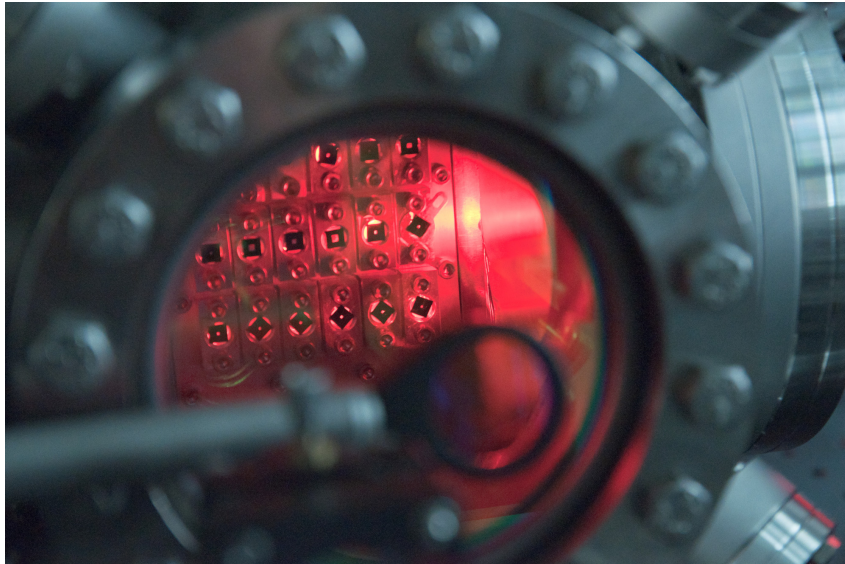


Figure A.2: Vacuum chamber for testing silicon nitride membranes. The measurement interferometer arm can be moved to address the membranes in the array. The red light is produced by a LED and used for imaging the interferometer laser spot relative to the membrane from behind.

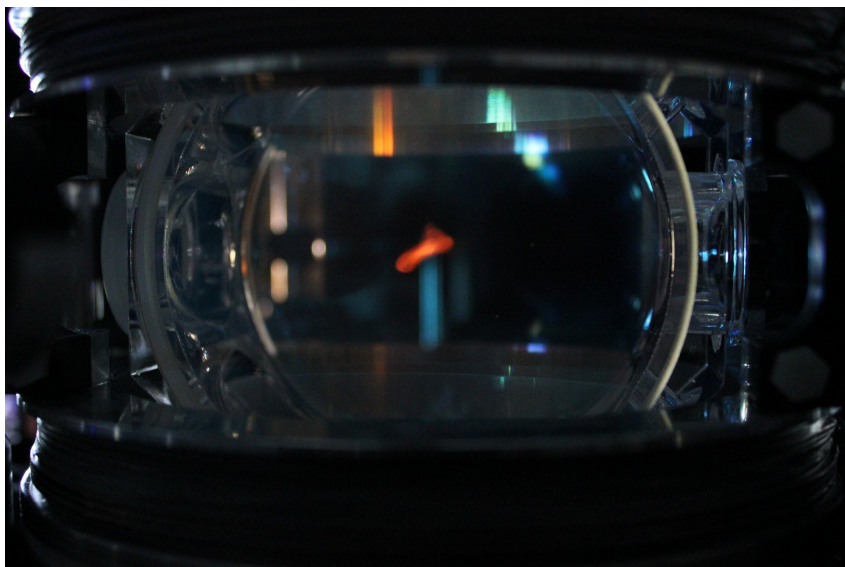


Figure A.3: Picture of the experiment cell with fluorescence emitted from a fully loaded MOT. On top and bottom one can see the MOT magnetic field coils.

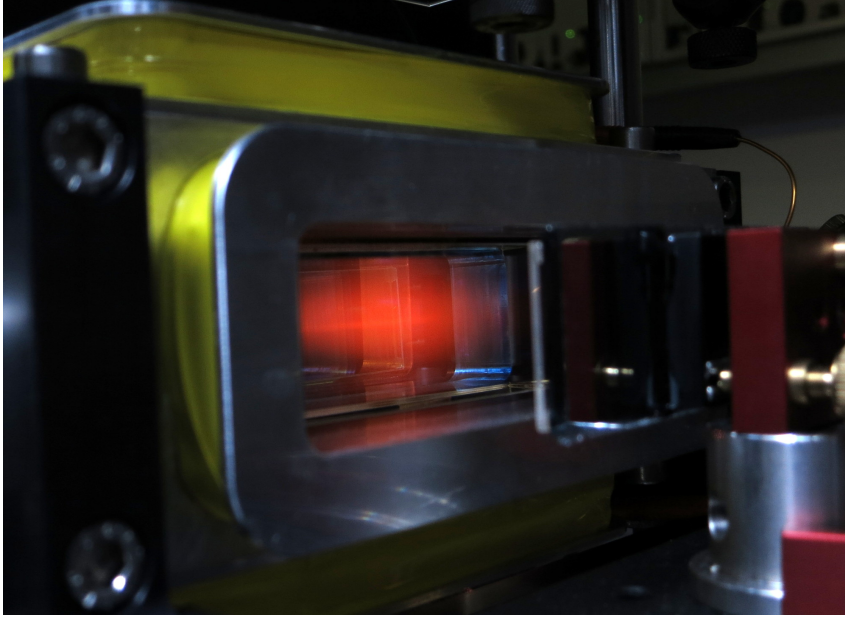


Figure A.4: Cooling region of the 2D-MOT inside the rectangular glass cell. The cooling beams have a  $2w_v = 2$  cm vertical and  $2w_h = 6$  cm horizontal diameter. Surrounding the cell the quadrupole magnetic field coils are visible. On the right is the reflecting mirror holder with the  $\lambda/4$  plate mounted on top.

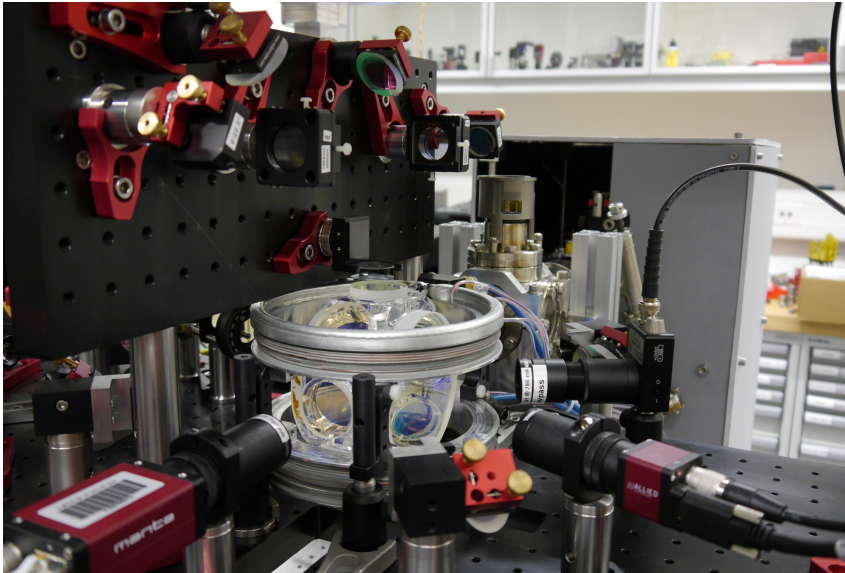


Figure A.5: View over the cold atom experiment section including both imaging cameras in the front and the 2D-MOT enclosed in a cardboard box in the back. The vertical plate hosts the vertical MOT axis optics (top row) and the newly installed transverse lattice optics (middle row).

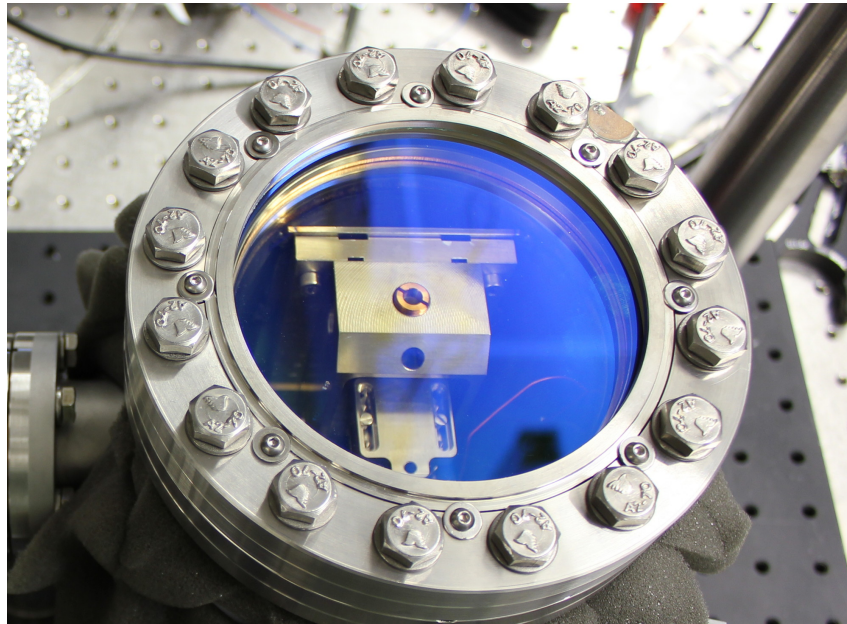


Figure A.6: Top view over the vacuum chamber containing the membrane inside the cavity. The main body holds the cavity mirrors, where the top one is placed below the bronze-colored hollow set screw. Below, the membrane holder resting on the positioners is visible.

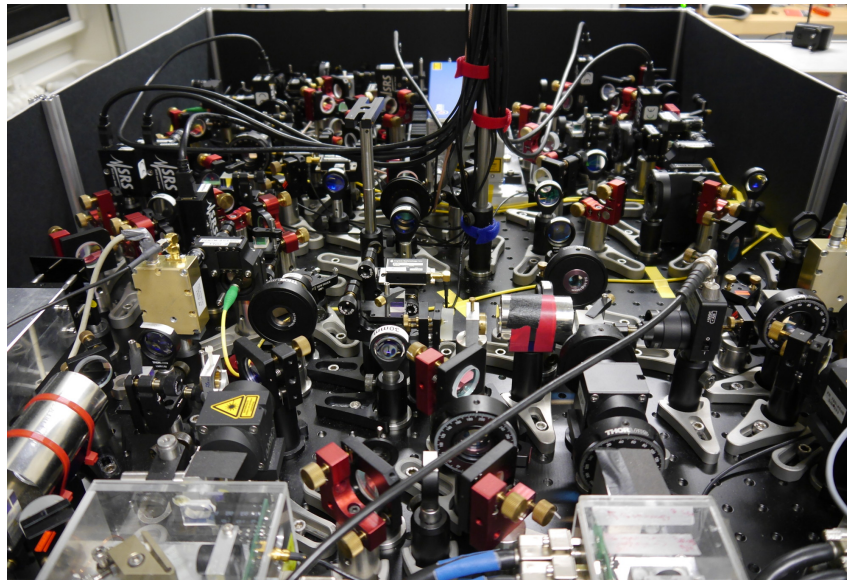


Figure A.7: View over the laser system. The lasers on the bottom are stabilized using saturated absorption spectroscopy, amplified and distributed into fibers.

# Appendix B

## Acronyms

RMS	Root Mean Square
PSD	Power Spectral Density
AOM	Acousto Optical Modulator
EOM	Electro Optical Modulator
MOT	Magneto Optical Trap
TOF	Time Of Flight
PDH	Pound Drever Hall
MIM	Membrane In Middle
PD	Photodiode
PBS	Polarizing Beam Splitter
CCD	Charged Coupled Device
FSR	Free Spectral Range
SNR	Signal to Noise Ratio
PZT	Piezo transducer
FIB	Focussed Ion Beam
FFT	Fast Fourier Transform

---

# Appendix C

## Variable definitions

### Membrane properties

Symbol	Description
$l$	membrane length
$d$	membrane thickness
$\Gamma_m$	Mechanical energy damping rate
$\Omega_m, \Omega_{x,y}$	Mechanical angular frequency (of mode x,y)
$Q$	Mechanical quality factor
$M$	Membrane effective mass ( $\geq 1/4$ physical mass)
$\bar{n}_{\text{th}}$	Thermal equilibrium phonon occupation
$\bar{n}$	Phonon occupation
$T_{\text{bath}}$	Effective thermal bath temperature
$T_0$	Bulk bath temperature
$\kappa_{\text{th}}$	membrane thermal conductivity
$a_m^2$	membrane intensity absorption coefficient
$S_{xx}(\omega)$	Double sided power spectral density of x, $S_x(\omega) = 2S_{xx}(\omega)$
$S_x(\omega)$	Single sided PSD of x, $\langle x^2 \rangle = \int_0^\infty S_x(\Omega) \frac{d\Omega}{2\pi}$

---

## Optical cavity

Symbol	Description
$\kappa$	Cavity linewidth FWHM in angular frequency, intensity decay rate
$r_{1,2}$	Front,back mirror amplitude reflectivity
$r_m$	Membrane amplitude reflectivity
$L$	Cavity length
$\mathcal{F}$	Cavity finesse
$\Delta$	Detuning laser-cavity, $\omega_L - \omega_{cav}$
$\omega_{FSR}$	Cavity free spectral range
$\Omega_{mod}$	PDH modulation angular frequency
$\eta$	Amplitude coupling efficiency to fundamental cavity mode
$P_{in}$	Laser power in front of cavity
$\bar{n}_{cav}$	Photon number in cavity

## Atomic system

Symbol	Description
$\Gamma_a$	Atomic damping rate
$\Omega_a$	Atomic axial angular frequency
$m$	$^{87}Rb$ single atom mass
$N$	atom number
$n_a$	atom density

## Lattice

Symbol	Description
$\Delta_{LA}$	Detuning laser-atoms $\omega_L - \omega_{at}$
$\lambda$	Laser wavelength
$2w$	$1/e^2$ Diameter of lattice beam at atom trap
$t$	laser light amplitude transmission from atoms to cavity
$P_0$	Incoming laser power at the atoms
$V_{dip}$	Lattice potential
$V_m$	Lattice modulation depth

## Coupling

Symbol	Description
$g_0$	Single photon coupling constant $g_0 = Gx_{\text{ZPF}}$
$G$	Cavity frequency shift per displacement $-d\omega_c/dx_m$
$\Gamma_{\text{opt}}$	Optomechanical energy damping rate
$\Gamma_{\text{sym}}$	Membrane energy damping due to atoms
$\Gamma_{\text{tot}}$	Total membrane energy damping rate
$\delta\Omega_m$	Optical spring shift in angular frequency
$N_r$	resonantly coupled atom number
$C$	Atom-membrane cooperativity
$g_N$	atom-membrane coupling constant
$T_{\text{opt}}$	Temperature with optomechanical cooling
$T_{\text{sym}}$	Temperature with additional sympathetic cooling

---

# List of Figures

1.1	Sketch of experiment system . . . . .	6
1.2	Simulation of thermal motion . . . . .	10
1.3	Cavity schematics for theoretical description . . . . .	11
1.4	Membrane position and reflectivity dependent resonance frequency . . . . .	13
1.5	Coupling strength in cavity . . . . .	14
1.6	Cooling estimate parameters . . . . .	29
2.1	Fabrication and modes of membranes . . . . .	32
2.2	Motional spectrum of a membrane . . . . .	33
2.3	Membrane tuning setup . . . . .	34
2.4	Membrane frequency tuning spectrum . . . . .	36
2.5	Frequency dependent quality factor coupling to frame modes . . . . .	38
2.6	Additional $Q$ dependency measurements . . . . .	39
2.7	Inverse $Q$ factors for higher membrane modes in comparison. . . . .	39
2.8	High stress membrane $Q$ . . . . .	41
2.9	FIB structured membrane . . . . .	43
2.10	Pictures of structured membranes . . . . .	45
3.1	Drawing of the apparatus . . . . .	48
3.2	3D-MOT schematics . . . . .	49
3.3	Top cut through the vacuum chamber . . . . .	51
3.4	3D-MOT chamber optics . . . . .	52
3.5	2D-MOT schematics . . . . .	54
3.6	Active magnetic field stabilizations . . . . .	60
3.7	Absorption spectroscopy and frequency synthesis . . . . .	61
3.8	Schematics of laser system . . . . .	62
3.9	Atom flux distribution and loading curve . . . . .	67
3.10	MOT parameters . . . . .	69
3.11	3D-MOT lifetime . . . . .	70
3.12	Short molasses parameters . . . . .	72
3.13	Long molasses parameters . . . . .	72
3.14	Lattice oscillation frequency measurement . . . . .	74
3.15	Lattice temperature . . . . .	75

*List of Figures*

---

4.1	Optomechanical cavity design . . . . .	81
4.2	Schematics of the laser system used for optomechanics . . . . .	83
4.3	Cavity transmission spectrum . . . . .	84
4.4	Measured optomechanical cavity parameters . . . . .	85
4.5	PDH signal experiment cavity . . . . .	87
4.6	Laser noise measurement setup . . . . .	90
4.7	Laser stabilization cavity schematic . . . . .	91
4.8	Locked laser noise . . . . .	92
4.9	Laser intensity noise in different situations . . . . .	93
4.10	Optomechanical damping in membrane ringdown measurements . . . . .	94
4.11	Optomechanical cooling data . . . . .	96
4.12	Optomechanical spring data . . . . .	97
5.1	Hybrid system for atom-membrane coupling . . . . .	100
5.2	Time domain sympathetic cooling . . . . .	101
5.3	Time domain temperature calibration . . . . .	103
5.4	Sympathetic cooling as a function of lattice power . . . . .	105
5.5	Atomic oscillation frequency dependent sympathetic cooling . . . . .	106
5.6	Power dependent membrane frequency shift in hybrid system . . . . .	107
5.7	Sympathetic cooling in ringdown measurements . . . . .	108
5.8	Atomic detuning dependent sympathetic cooling . . . . .	109
6.1	New optomechanical cavity . . . . .	114
A.1	Silicon nitride membrane . . . . .	117
A.2	Membrane testing setup . . . . .	118
A.3	Trapped atoms . . . . .	118
A.4	2D-MOT fluorescence . . . . .	119
A.5	Mot apparatus . . . . .	119
A.6	Experiment cavity . . . . .	120
A.7	Laser System . . . . .	120

# List of Tables

2.1	Basic membrane material properties . . . . .	33
2.2	Summary of measured low-stress SiN membrane parameters . . . . .	40
3.1	Magnetic field coil parameters . . . . .	57
3.2	Magnetic field coil performance . . . . .	58
3.3	Camera data . . . . .	65
4.1	Experiment cavity parameters . . . . .	80
4.2	Stabilization cavity parameters . . . . .	91



# Bibliography

- [1] O. Romero-Isart. Quantum superposition of massive objects and collapse models. *Phys. Rev. A*, 84(5):052121, November 2011. doi:[10.1103/PhysRevA.84.052121](https://doi.org/10.1103/PhysRevA.84.052121).
- [2] A. Bassi, K. Lochan, S. Satin, T. P. Singh, and H. Ulbricht. Models of wavefunction collapse, underlying theories, and experimental tests. *Reviews of Modern Physics*, 85:471–527, April 2013. doi:[10.1103/RevModPhys.85.471](https://doi.org/10.1103/RevModPhys.85.471).
- [3] A. Dorsel, J. D. McCullen, P. Meystre, E. Vignes, and H. Walther. Optical bistability and mirror confinement induced by radiation pressure. *Phys. Rev. Lett.*, 51:1550–1553, October 1983. doi:[10.1103/PhysRevLett.51.1550](https://doi.org/10.1103/PhysRevLett.51.1550).
- [4] M. Aspelmeyer, T. J. Kippenberg, and F. Marquardt. Cavity Optomechanics. *ArXiv:1303.0733*, March 2013.
- [5] S. Gröblacher, K. Hammerer, M. R. Vanner, and M. Aspelmeyer. Observation of strong coupling between a micromechanical resonator and an optical cavity field. *Nature*, 460:724–727, August 2009. doi:[10.1038/nature08171](https://doi.org/10.1038/nature08171).
- [6] J. Gieseler, B. Deutsch, R. Quidant, and L. Novotny. Subkelvin Parametric Feedback Cooling of a Laser-Trapped Nanoparticle. *Phys. Rev. Lett.*, 109(10):103603, September 2012. doi:[10.1103/PhysRevLett.109.103603](https://doi.org/10.1103/PhysRevLett.109.103603).
- [7] P. Asenbaum, S. Kuhn, S. Nimmrichter, U. Sezer, and M. Arndt. Cavity cooling of free silicon nanoparticles in high vacuum. *Nature Communications*, 4:2743, November 2013. doi:[10.1038/ncomms3743](https://doi.org/10.1038/ncomms3743).
- [8] N. Kiesel, F. Blaser, U. Delic, D. Grass, R. Kaltenbaek, and M. Aspelmeyer. Cavity cooling of an optically levitated submicron particle. *Proceedings of the National Academy of Science*, 110:14180–14185, August 2013. doi:[10.1073/pnas.1309167110](https://doi.org/10.1073/pnas.1309167110).
- [9] E. Verhagen, S. Deléglise, S. Weis, A. Schliesser, and T. J. Kippenberg. Quantum-coherent coupling of a mechanical oscillator to an optical cavity mode. *Nature*, 482:63–67, February 2012. doi:[10.1038/nature10787](https://doi.org/10.1038/nature10787).

- [10] J. D. Thompson, B. M. Zwickl, A. M. Jayich, Florian Marquardt, S. M. Girvin, and J. G. E. Harris. Strong dispersive coupling of a high-finesse cavity to a micromechanical membrane. *Nature*, 452(7183):72–75, March 2008. ISSN 0028-0836. doi:[10.1038/nature06715](https://doi.org/10.1038/nature06715).
- [11] D. J. Wilson, C. A. Regal, S. B. Papp, and H. J. Kimble. Cavity Optomechanics with Stoichiometric SiN Films. *Phys. Rev. Lett.*, 103(20):207204, November 2009. doi:[10.1103/PhysRevLett.103.207204](https://doi.org/10.1103/PhysRevLett.103.207204).
- [12] Donghun Lee, Mitchell Underwood, David Mason, Alexey B. Shkarin, Kjetil Borkje, Steve M. Girvin, and Jack G. E. Harris. Observation of quantum motion in a nanogram-scale object. *ArXiv:1406.7254*, June 2014.
- [13] Jasper Chan, T. P. Mayer Alegre, Amir H. Safavi-Naeini, Jeff T. Hill, Alex Krause, Simon Groblacher, Markus Aspelmeyer, and Oskar Painter. Laser cooling of a nanomechanical oscillator into its quantum ground state. *Nature*, 478(7367):89–92, October 2011. ISSN 0028-0836. doi:[10.1038/nature10461](https://doi.org/10.1038/nature10461).
- [14] David Hunger, Stephan Camerer, Theodor W. Hänsch, Daniel König, Jörg P. Kotthaus, Jakob Reichel, and Philipp Treutlein. Resonant coupling of a Bose-Einstein condensate to a micromechanical oscillator. *Phys. Rev. Lett.*, 104:143002, April 2010. doi:[10.1103/PhysRevLett.104.143002](https://doi.org/10.1103/PhysRevLett.104.143002).
- [15] S. Camerer, M. Korppi, A. Jöckel, D. Hunger, T. W. Hänsch, and P. Treutlein. Realization of an Optomechanical Interface Between Ultracold Atoms and a Membrane. *Phys. Rev. Lett.*, 107(22):223001, November 2011. doi:[10.1103/PhysRevLett.107.223001](https://doi.org/10.1103/PhysRevLett.107.223001).
- [16] Dan M. Stamper-Kurn. Cavity optomechanics with cold atoms. *ArXiv:1204.4351*, April 2012.
- [17] A. D. O’Connell, M. Hofheinz, M. Ansmann, Radoslaw C. Bialczak, M. Lenander, Erik Lucero, M. Neeley, D. Sank, H. Wang, M. Weides, J. Wenner, John M. Martinis, and A. N. Cleland. Quantum ground state and single-phonon control of a mechanical resonator. *Nature*, 464(7289):697–703, April 2010. ISSN 0028-0836. doi:[10.1038/nature08967](https://doi.org/10.1038/nature08967).
- [18] T. Faust, J. Rieger, M. J. Seitner, J. P. Kotthaus, and E. M. Weig. Coherent control of a classical nanomechanical two-level system. *Nature Physics*, 9:485–488, August 2013. doi:[10.1038/nphys2666](https://doi.org/10.1038/nphys2666).
- [19] T. Corbitt, D. Ottaway, E. Innerhofer, J. Pelc, and N. Mavalvala. Measurement of radiation-pressure-induced optomechanical dynamics in a suspended Fabry-Perot cavity. *Phys. Rev. A*, 74(2):021802, August 2006. doi:[10.1103/PhysRevA.74.021802](https://doi.org/10.1103/PhysRevA.74.021802).

- [20] J. D. Teufel, T. Donner, Dale Li, J. W. Harlow, M. S. Allman, K. Cicak, A. J. Sirois, J. D. Whittaker, K. W. Lehnert, and R. W. Simmonds. Sideband cooling of micromechanical motion to the quantum ground state. *Nature*, 475 (7356):359–363, July 2011. doi:[10.1038/nature10261](https://doi.org/10.1038/nature10261).
- [21] T. A. Palomaki, J. W. Harlow, J. D. Teufel, R. W. Simmonds, and K. W. Lehnert. Coherent state transfer between itinerant microwave fields and a mechanical oscillator. *Nature*, 495:210–214, March 2013. doi:[10.1038/nature11915](https://doi.org/10.1038/nature11915).
- [22] David Hunger, Stephan Camerer, Maria Korppi, Andreas Jöckel, Theodor W Hänsch, and Philipp Treutlein. Coupling ultracold atoms to mechanical oscillators. *C. R. Phys.*, 12:871, August 2011. doi:[10.1016/j.crhy.2011.04.015](https://doi.org/10.1016/j.crhy.2011.04.015).
- [23] P. Treutlein, C. Genes, K. Hammerer, M. Poggio, and P. Rabl. Hybrid Mechanical Systems. *ArXiv:1210.4151*, October 2012.
- [24] J. Teissier, A. Barfuss, P. Appel, E. Neu, and P. Maletinsky. Strain Coupling of a Nitrogen-Vacancy Center Spin to a Diamond Mechanical Oscillator. *Phys. Rev. Lett.*, 113(2):020503, July 2014. doi:[10.1103/PhysRevLett.113.020503](https://doi.org/10.1103/PhysRevLett.113.020503).
- [25] O. Arcizet, V. Jacques, A. Siria, P. Poncharal, P. Vincent, and S. Seidelin. A single nitrogen-vacancy defect coupled to a nanomechanical oscillator. *Nature Physics*, 7(11):879–883, November 2011. doi:[10.1038/nphys2070](https://doi.org/10.1038/nphys2070).
- [26] C. L. Degen, M. Poggio, H. J. Mamin, C. T. Rettner, and D. Rugar. Nanoscale magnetic resonance imaging. *Proceedings of the National Academy of Sciences*, 106(5):1313–1317, 2009. doi:[10.1073/pnas.0812068106](https://doi.org/10.1073/pnas.0812068106).
- [27] Shimon Kolkowitz, Ania C. Bleszynski Jayich, Quirin P. Unterreithmeier, Steven D. Bennett, Peter Rabl, J. G. E. Harris, and Mikhail D. Lukin. Coherent sensing of a mechanical resonator with a single-spin qubit. *Science*, 335 (6076):1603–1606, 2012. doi:[10.1126/science.1216821](https://doi.org/10.1126/science.1216821).
- [28] Michele Montinaro, Gunter Wüst, Mathieu Munsch, Yannik Fontana, Eleonora Russo-Averchi, Martin Heiss, Anna Fontcuberta i Morral, Richard J. Warburton, and Martino Poggio. Quantum dot opto-mechanics in a fully self-assembled nanowire. *Nano Letters*, 14(8):4454–4460, 2014. doi:[10.1021/nl501413t](https://doi.org/10.1021/nl501413t).
- [29] I. Yeo, P-L. de Assis, A. Gloppe, E. Dupont-Ferrier, P. Verlot, N. S. Malik, E. Dupuy, J. Claudon, J-M. Gerard, A. Auffeves, G. Nogues, S. Seidelin, J-Ph. Poizat, O. Arcizet, and M. Richard. Strain-mediated coupling in a quantum dot-mechanical oscillator hybrid system. *Nature Nanotechnology*, advance online publication:–, December 2013. doi:[10.1038/nnano.2013.274](https://doi.org/10.1038/nnano.2013.274).
- [30] J M Pirkkalainen, S U Cho, Jian Li, G S Paraoanu, P J Hakonen, and M A Sillanpää. Hybrid circuit cavity quantum electrodynamics with

- a micromechanical resonator. *Nature*, 494(7436):211–215, February 2013. doi:[10.1038/nature11821](https://doi.org/10.1038/nature11821).
- [31] T. Bagci, A. Simonsen, S. Schmid, L. G. Villanueva, E. Zeuthen, J. Appel, J. M. Taylor, A. Sørensen, K. Usami, A. Schliesser, and E. S. Polzik. Optical detection of radio waves through a nanomechanical transducer. *Nature*, 507: 81–85, March 2014. doi:[10.1038/nature13029](https://doi.org/10.1038/nature13029).
- [32] R. W. Andrews, R. W. Peterson, T. P. Purdy, K. Cicak, R. W. Simmonds, C. A. Regal, and K. W. Lehnert. Bidirectional and efficient conversion between microwave and optical light. *Nature Physics*, 10:321–326, April 2014. doi:[10.1038/nphys2911](https://doi.org/10.1038/nphys2911).
- [33] Matthias Weidemüller and Claus Zimmermann, editors. *Cold Atoms and Molecules*. Wiley-VCH, Berlin, 2009.
- [34] Claudiu Genes, Helmut Ritsch, Michael Drewsen, and Aurélien Dantan. Atom-membrane cooling and entanglement using cavity electromagnetically induced transparency. *Phys. Rev. A*, 84(5):051801, November 2011. doi:[10.1103/PhysRevA.84.051801](https://doi.org/10.1103/PhysRevA.84.051801).
- [35] Claudiu Genes, D Vitali, and P Tombesi. Emergence of atom-light-mirror entanglement inside an optical cavity. *Phys. Rev. A*, 77(5):050307, May 2008. doi:[10.1103/PhysRevA.77.050307](https://doi.org/10.1103/PhysRevA.77.050307).
- [36] H Ian, Z Gong, Yu-xi Liu, C Sun, and Franco Nori. Cavity optomechanical coupling assisted by an atomic gas. *Phys. Rev. A*, 78(1):013824, July 2008. doi:[10.1103/PhysRevA.78.013824](https://doi.org/10.1103/PhysRevA.78.013824).
- [37] K. Hammerer, M. Wallquist, C. Genes, M. Ludwig, F. Marquardt, P. Treutlein, P. Zoller, J. Ye, and H. J. Kimble. Strong coupling of a mechanical oscillator and a single atom. *Phys. Rev. Lett.*, 103:063005, August 2009. doi:[10.1103/PhysRevLett.103.063005](https://doi.org/10.1103/PhysRevLett.103.063005).
- [38] Klemens Hammerer, M Aspelmeyer, E Polzik, and Peter Zoller. Establishing Einstein-Poldosky-Rosen Channels between Nanomechanics and Atomic Ensembles. *Phys. Rev. Lett.*, 102(2):020501, January 2009. doi:[10.1103/PhysRevLett.102.020501](https://doi.org/10.1103/PhysRevLett.102.020501).
- [39] Andrew Geraci and John Kitching. Ultracold mechanical resonators coupled to atoms in an optical lattice. *Phys. Rev. A*, 80(3):032317, September 2009. doi:[10.1103/PhysRevA.80.032317](https://doi.org/10.1103/PhysRevA.80.032317).
- [40] D Meiser and P Meystre. Coupled dynamics of atoms and radiation-pressure-driven interferometers. *Phys. Rev. A*, 73(3):033417, March 2006. doi:[10.1103/PhysRevA.73.033417](https://doi.org/10.1103/PhysRevA.73.033417).

- [41] Swati Singh and Pierre Meystre. Atomic probe Wigner tomography of a nanomechanical system. *Phys. Rev. A*, 81(4):041804, April 2010. doi:[10.1103/PhysRevA.81.041804](https://doi.org/10.1103/PhysRevA.81.041804).
- [42] M Paternostro, G De Chiara, and G Palma. Cold-Atom-Induced Control of an Optomechanical Device. *Phys. Rev. Lett.*, 104(24):243602, June 2010. doi:[10.1103/PhysRevLett.104.243602](https://doi.org/10.1103/PhysRevLett.104.243602).
- [43] C Joshi, A Hutter, F Zimmer, M Jonson, E Andersson, and P Ohberg. Quantum entanglement of nanocantilevers. *Phys. Rev. A*, 82(4):043846, October 2010. doi:[10.1103/PhysRevA.82.043846](https://doi.org/10.1103/PhysRevA.82.043846).
- [44] A Carmele, Berit Vogell, Kai Stannigel, and Peter Zoller. Opto-Nanomechanics Strongly Coupled to a Rydberg Superatom: Coherent vs. Incoherent Dynamics. *ArXiv:1312.6551*, December 2013.
- [45] B. Vogell, K. Stannigel, P. Zoller, K. Hammerer, M. T. Rakher, M. Korppi, A. Jöckel, and P. Treutlein. Cavity-enhanced long-distance coupling of an atomic ensemble to a micromechanical membrane. *Phys. Rev. A*, 87(2):023816, February 2013. doi:[10.1103/PhysRevA.87.023816](https://doi.org/10.1103/PhysRevA.87.023816).
- [46] K. Hammerer, K. Stannigel, C. Genes, P. Zoller, P. Treutlein, S. Camerer, D. Hunger, and T. W. Hänsch. Optical lattices with micromechanical mirrors. *Phys. Rev. A*, 82:021803, August 2010. doi:[10.1103/PhysRevA.82.021803](https://doi.org/10.1103/PhysRevA.82.021803).
- [47] J. S. Bennett, L. S. Madsen, M. Baker, H. Rubinsztein-Dunlop, and W. P. Bowen. Coherent control and feedback cooling in a remotely coupled hybrid atom-optomechanical system. *New Journal of Physics*, 16(8):083036, August 2014. doi:[10.1088/1367-2630/16/8/083036](https://doi.org/10.1088/1367-2630/16/8/083036).
- [48] P. Treutlein, D. Hunger, S. Camerer, T. W. Hänsch, and J. Reichel. Bose-Einstein Condensate Coupled to a Nanomechanical Resonator on an Atom Chip. *Phys. Rev. Lett.*, 99(14):140403, October 2007. doi:[10.1103/PhysRevLett.99.140403](https://doi.org/10.1103/PhysRevLett.99.140403).
- [49] L. Tian and P. Zoller. Coupled Ion-Nanomechanical Systems. *Physical Review Letters*, 93(26):266403, December 2004. doi:[10.1103/PhysRevLett.93.266403](https://doi.org/10.1103/PhysRevLett.93.266403).
- [50] C. J. Myatt, E. A. Burt, R. W. Ghrist, E. A. Cornell, and C. E. Wieman. Production of two overlapping bose-einstein condensates by sympathetic cooling. *Phys. Rev. Lett.*, 78:586–589, Jan 1997. doi:[10.1103/PhysRevLett.78.586](https://doi.org/10.1103/PhysRevLett.78.586).
- [51] D. J. Larson, J. C. Bergquist, J. J. Bollinger, Wayne M. Itano, and D. J. Wineland. Sympathetic cooling of trapped ions: A laser-cooled two-species nonneutral ion plasma. *Phys. Rev. Lett.*, 57:70–73, Jul 1986. doi:[10.1103/PhysRevLett.57.70](https://doi.org/10.1103/PhysRevLett.57.70).

- [52] D. Offenberg, C. B. Zhang, Ch. Wellers, B. Roth, and S. Schiller. Translational cooling and storage of protonated proteins in an ion trap at subkelvin temperatures. *Phys. Rev. A*, 78:061401, Dec 2008. doi:[10.1103/PhysRevA.78.061401](https://doi.org/10.1103/PhysRevA.78.061401).
- [53] Dalziel Joseph Wilson. *Cavity Optomechanics with High-Stress Silicon Nitride Films*. PhD thesis, California Institute of Technology, 2011.
- [54] G. Volpe and G. Volpe. Simulation of a Brownian particle in an optical trap. *American Journal of Physics*, 81:224–230, March 2013. doi:[10.1119/1.4772632](https://doi.org/10.1119/1.4772632).
- [55] B.E.A. Saleh and M.C. Teich. *Fundamentals of photonics*. Wiley, Hoboken, New Jersey, 1991.
- [56] A. M. Jayich, J. C. Sankey, B. M. Zwickl, C. Yang, J. D. Thompson, S. M. Girvin, A. A. Clerk, F. Marquardt, and J. G. E. Harris. Dispersive optomechanics: a membrane inside a cavity. *New Journal of Physics*, 10(9):095008, September 2008. doi:[10.1088/1367-2630/10/9/095008](https://doi.org/10.1088/1367-2630/10/9/095008).
- [57] T. Weiss and A. Nunnenkamp. Quantum limit of laser cooling in dispersively and dissipatively coupled optomechanical systems. *Phys. Rev. A*, 88(2):023850, August 2013. doi:[10.1103/PhysRevA.88.023850](https://doi.org/10.1103/PhysRevA.88.023850).
- [58] A. Xuereb, R. Schnabel, and K. Hammerer. Dissipative Optomechanics in a Michelson-Sagnac Interferometer. *Phys. Rev. Lett.*, 107(21):213604, November 2011. doi:[10.1103/PhysRevLett.107.213604](https://doi.org/10.1103/PhysRevLett.107.213604).
- [59] C. H. Bui, J. Zheng, S. W. Hoch, L. Y. T. Lee, J. G. E. Harris, and C. Wei Wong. High-reflectivity, high-Q micromechanical membranes via guided resonances for enhanced optomechanical coupling. *Appl. Phys. Lett.*, 100(2):021110, January 2012. doi:[10.1063/1.3658731](https://doi.org/10.1063/1.3658731).
- [60] Corey Stambaugh, Haitan Xu, Utku Kemiktarak, Jacob Taylor, and John Lawall. From membrane-in-the-middle to mirror-in-the-middle with a high-reflectivity sub-wavelength grating. *ArXiv:1407.1709*, July 2014.
- [61] O. Arcizet, P.-F. Cohadon, T. Briant, M. Pinard, and A. Heidmann. Radiation-pressure cooling and optomechanical instability of a micromirror. *Nature*, 444:71–74, November 2006. doi:[10.1038/nature05244](https://doi.org/10.1038/nature05244).
- [62] P. Meystre. A short walk through quantum optomechanics. *Annalen der Physik*, 525:215–233, March 2013. doi:[10.1002/andp.201200226](https://doi.org/10.1002/andp.201200226).
- [63] M. Ludwig, B. Kubala, and F. Marquardt. The optomechanical instability in the quantum regime. *New Journal of Physics*, 10(9):095013, September 2008. doi:[10.1088/1367-2630/10/9/095013](https://doi.org/10.1088/1367-2630/10/9/095013).
- [64] A. M. Jayich, J. C. Sankey, K. Børkje, D. Lee, C. Yang, M. Underwood, L. Childress, A. Petrenko, S. M. Girvin, and J. G. E. Harris.

- Cryogenic optomechanics with a  $\text{Si}_3\text{N}_4$  membrane and classical laser noise. *New Journal of Physics*, 14(11):115018, November 2012. doi:[10.1088/1367-2630/14/11/115018](https://doi.org/10.1088/1367-2630/14/11/115018).
- [65] T. J. Kippenberg, A. Schliesser, and M. L. Gorodetsky. Phase noise measurement of external cavity diode lasers and implications for optomechanical sideband cooling of GHz mechanical modes. *New Journal of Physics*, 15(1):015019, January 2013. doi:[10.1088/1367-2630/15/1/015019](https://doi.org/10.1088/1367-2630/15/1/015019).
- [66] H. P. Yuen and V. W. S. Chan. Noise in homodyne and heterodyne detection. *Optics Letters*, 8:177–179, March 1983. doi:[10.1364/OL.8.000177](https://doi.org/10.1364/OL.8.000177).
- [67] E. D. Black. An introduction to Pound-Drever-Hall laser frequency stabilization. *American Journal of Physics*, 69:79–87, January 2001. doi:[10.1119/1.1286663](https://doi.org/10.1119/1.1286663).
- [68] T. P. Purdy, R. W. Peterson, and C. A. Regal. Observation of radiation pressure shot noise on a macroscopic object. *Science*, 339(6121):801–804, 2013. doi:[10.1126/science.1231282](https://doi.org/10.1126/science.1231282).
- [69] Harold J. Metcalf and Peter van der Straten. *Laser Cooling and Trapping*. Springer, 1999.
- [70] H. J. Metcalf and P. van der Straten. Laser cooling and trapping of atoms. *Journal of the Optical Society of America B Optical Physics*, 20:887–908, May 2003. doi:[10.1364/JOSAB.20.000887](https://doi.org/10.1364/JOSAB.20.000887).
- [71] R. Grimm, M. Weidemüller, and Y. B. Ovchinnikov. Optical Dipole Traps for Neutral Atoms. *Advances in Atomic Molecular and Optical Physics*, 42:95–170, 2000. doi:[10.1016/S1049-250X\(08\)60186-X](https://doi.org/10.1016/S1049-250X(08)60186-X).
- [72] Daniel A. Steck. Rubidium 87 d line data, 2003. URL <http://steck.us/alkalidata/>.
- [73] J. Dalibard and C. Cohen-Tannoudji. Laser cooling below the Doppler limit by polarization gradients: Simple theoretical models. *Journal of the Optical Society of America B Optical Physics*, 6:2023–2045, November 1989. doi:[10.1364/JOSAB.6.002023](https://doi.org/10.1364/JOSAB.6.002023).
- [74] N. V. Morrow, S. K. Dutta, and G. Raithel. Feedback Control of Atomic Motion in an Optical Lattice. *Phys. Rev. Lett.*, 88(9):093003, March 2002. doi:[10.1103/PhysRevLett.88.093003](https://doi.org/10.1103/PhysRevLett.88.093003).
- [75] L. V. Hau, S. E. Harris, Z. Dutton, and C. H. Behroozi. Light speed reduction to 17 metres per second in an ultracold atomic gas. *Nature*, 397:594–598, February 1999. doi:[10.1038/17561](https://doi.org/10.1038/17561).
- [76] S. E. Harris. Electromagnetically induced transparency. *Physics Today*, 50:36–42, July 1997. doi:[10.1063/1.881806](https://doi.org/10.1063/1.881806).

- [77] B. M. Zwickl, W. E. Shanks, A. M. Jayich, C. Yang, A. C. Bleszynski Jayich, J. D. Thompson, and J. G. E. Harris. High quality mechanical and optical properties of commercial silicon nitride membranes. *Appl. Phys. Lett.*, 92(10):103125, March 2008. doi:[10.1063/1.2884191](https://doi.org/10.1063/1.2884191).
- [78] D. Friedrich, H. Kaufer, T. Westphal, K. Yamamoto, A. Sawadsky, F. Y. Khalili, S. L. Danilishin, S. Gößler, K. Danzmann, and R. Schnabel. Laser interferometry with translucent and absorbing mechanical oscillators. *New Journal of Physics*, 13(9):093017, September 2011. doi:[10.1088/1367-2630/13/9/093017](https://doi.org/10.1088/1367-2630/13/9/093017).
- [79] A. Jöckel, M. T. Rakher, M. Korppi, S. Camerer, D. Hunger, M. Mader, and P. Treutlein. Spectroscopy of mechanical dissipation in micro-mechanical membranes. *Appl. Phys. Lett.*, 99(14):143109, October 2011. doi:[10.1063/1.3646914](https://doi.org/10.1063/1.3646914).
- [80] C. M. Wang and C. Y. Wang, editors. *Structural vibration : exact solutions for strings, membranes, beams, and plates*. Boca Raton, [Florida] : Taylor & Francis/CRC Press, 2014.
- [81] B. Zink and F. Hellman. Specific heat and thermal conductivity of low-stress amorphous Si N membranes. *Solid State Commun.*, 129:199–204, 2004. doi:[10.1016/j.ssc.2003.08.048](https://doi.org/10.1016/j.ssc.2003.08.048).
- [82] Wen-Hsien Chuang, T. Luger, R.K. Fettig, and R. Ghodssi. Mechanical property characterization of lpcvd silicon nitride thin films at cryogenic temperatures. *Microelectromechanical Systems, Journal of*, 13(5):870 – 879, 2004. doi:[10.1109/JMEMS.2004.836815](https://doi.org/10.1109/JMEMS.2004.836815).
- [83] Technical information provided by norcada, 2014.
- [84] H. O. Pierson. *Handbook of Chemical Vapor Deposition(CVD): Principles, Technology and Applications*. Noyes Publications, Norwich, New York, 2nd edition, 1999.
- [85] S. S. Verbridge, D. F. Shapiro, H. G. Craighead, and J. M. Parpia. Macroscopic Tuning of Nanomechanics: Substrate Bending for Reversible Control of Frequency and Quality Factor of Nanostring Resonators. *Nano Letters*, 7:1728–1735, 2007. doi:[10.1021/nl070716t](https://doi.org/10.1021/nl070716t).
- [86] I. Wilson-Rae. Intrinsic dissipation in nanomechanical resonators due to phonon tunneling. *Phys. Rev. B*, 77(24):245418, June 2008. doi:[10.1103/PhysRevB.77.245418](https://doi.org/10.1103/PhysRevB.77.245418).
- [87] D. R. Southworth, R. A. Barton, S. S. Verbridge, B. Ilic, A. D. Fefferman, H. G. Craighead, and J. M. Parpia. Stress and Silicon Nitride: A Crack in the Universal Dissipation of Glasses. *Phys. Rev. Lett.*, 102(22):225503–+, June 2009. doi:[10.1103/PhysRevLett.102.225503](https://doi.org/10.1103/PhysRevLett.102.225503).

- [88] Q. P. Unterreithmeier, T. Faust, and J. P. Kotthaus. Damping of Nanomechanical Resonators. *Phys. Rev. Lett.*, 105(2):027205, July 2010. doi:[10.1103/PhysRevLett.105.027205](https://doi.org/10.1103/PhysRevLett.105.027205).
- [89] I. Wilson-Rae, R. A. Barton, S. S. Verbridge, D. R. Southworth, B. Ilic, H. G. Craighead, and J. M. Parpia. High-Q Nanomechanics via Destructive Interference of Elastic Waves. *Phys. Rev. Lett.*, 106(4):047205–+, 2011. doi:[10.1103/PhysRevLett.106.047205](https://doi.org/10.1103/PhysRevLett.106.047205).
- [90] G. D. Cole, I. Wilson-Rae, K. Werbach, M. R. Vanner, and M. Aspelmeyer. Phonon-tunnelling dissipation in mechanical resonators. *Nature Communications*, 2, 2011. doi:[10.1038/ncomms1212](https://doi.org/10.1038/ncomms1212).
- [91] P.-L. Yu, T. P. Purdy, and C. A. Regal. Control of Material Damping in High-Q Membrane Microresonators. *Phys. Rev. Lett.*, 108(8):083603, February 2012. doi:[10.1103/PhysRevLett.108.083603](https://doi.org/10.1103/PhysRevLett.108.083603).
- [92] S Chakram, Y S Patil, L Chang, and M. Vengalattore. Dissipation in Ultrahigh Quality Factor SiN Membrane Resonators. *Phys. Rev. Lett.*, 112(12):127201, March 2014. doi:[10.1103/PhysRevLett.112.127201](https://doi.org/10.1103/PhysRevLett.112.127201).
- [93] WeeChong Tan, S. Kobayashi, T. Aoki, RobertE. Johanson, and S.O. Kasap. Optical properties of amorphous silicon nitride thin-films prepared by vhf-pecvd using silane and nitrogen. *Journal of Materials Science: Materials in Electronics*, 20(1):15–18, 2009. doi:[10.1007/s10854-007-9422-2](https://doi.org/10.1007/s10854-007-9422-2).
- [94] Matthias Mader. Characterisation of silicon nitride membranes for optomechanical experiments. Master’s thesis, Ludwig-Maximilians-Universität München, 2010.
- [95] Tanguy Rouxel, Jean-Christophe Sangleboeuf, Marc Huger, Christian Gault, Jean-Louis Besson, and Sébastien Testu. Temperature dependence of young’s modulus in si<sub>3</sub>n<sub>4</sub>-based ceramics: roles of sintering additives and of sic-particle content. *Acta Mater.*, 50(7):1669 – 1682, 2002. doi:[10.1016/S1359-6454\(02\)00004-6](https://doi.org/10.1016/S1359-6454(02)00004-6).
- [96] K. G. Lyon, G. L. Salinger, C. A. Swenson, and G. K. White. Linear thermal expansion measurements on silicon from 6 to 340 K. *J. Appl. Phys.*, 48:865–868, 1977. doi:[10.1063/1.323747](https://doi.org/10.1063/1.323747).
- [97] M. Wallquist, K. Hammerer, P. Zoller, C. Genes, M. Ludwig, F. Marquardt, P. Treutlein, J. Ye, and H. J. Kimble. Single-atom cavity QED and optomechanics. *Phys. Rev. A*, 81(2):023816–+, February 2010. doi:[10.1103/PhysRevA.81.023816](https://doi.org/10.1103/PhysRevA.81.023816).
- [98] Thiago P. Mayer Alegre, Amir Safavi-Naeini, Martin Winger, and Oskar Painter. Quasi-two-dimensional optomechanical crystals with

- a complete phononic bandgap. *Opt. Express*, 19(6):5658–5669, 2011. doi:[10.1364/OE.19.005658](https://doi.org/10.1364/OE.19.005658).
- [99] P.-L. Yu, K. Cicak, N. S. Kampel, Y. Tsaturyan, T. P. Purdy, R. W. Simmonds, and C. A. Regal. A phononic bandgap shield for high-Q membrane microresonators. *Appl. Phys. Lett.*, 104(2):023510, January 2014. doi:[10.1063/1.4862031](https://doi.org/10.1063/1.4862031).
- [100] Y. Tsaturyan, A. Barg, A. Simonsen, L. G. Villanueva, S. Schmid, A. Schliesser, and E. S. Polzik. Demonstration of suppressed phonon tunneling losses in phononic bandgap shielded membrane resonators for high-Q optomechanics. *Optics Express*, 22:6810, March 2014. doi:[10.1364/OE.22.006810](https://doi.org/10.1364/OE.22.006810).
- [101] Cindy Regal. private communication, 2014.
- [102] S. S. Verbridge, J. M. Parpia, R. B. Reichenbach, L. M. Bellan, and H. G. Craighead. High quality factor resonance at room temperature with nanostings under high tensile stress. *J. Appl. Phys.*, 99(12):124304, June 2006. doi:[10.1063/1.2204829](https://doi.org/10.1063/1.2204829).
- [103] David Hunger. *A Bose-Einstein condensate coupled to a micromechanical oscillator*. PhD thesis, Ludwig-Maximilians-Universität München, 2010.
- [104] Stephan Camerer. *Interfacing ultracold atoms and mechanical oscillators*. PhD thesis, Ludwig-Maximilians-Universität München, 2011.
- [105] M. T. Rakher, R. J. Warburton, and P. Treutlein. Prospects for storage and retrieval of a quantum-dot single photon in an ultracold  $^{87}\text{Rb}$  ensemble. *Phys. Rev. A*, 88(5):053834, November 2013. doi:[10.1103/PhysRevA.88.053834](https://doi.org/10.1103/PhysRevA.88.053834).
- [106] R. Zhao, Y. O. Dudin, S. D. Jenkins, C. J. Campbell, D. N. Matsukevich, T. A. B. Kennedy, and A. Kuzmich. Long-lived quantum memory. *Nature Physics*, 5:100–104, February 2009. doi:[10.1038/nphys1152](https://doi.org/10.1038/nphys1152).
- [107] T. Kinoshita, T. Wenger, and D. S. Weiss. All-optical Bose-Einstein condensation using a compressible crossed dipole trap. *Phys. Rev. A*, 71(1):011602, January 2005. doi:[10.1103/PhysRevA.71.011602](https://doi.org/10.1103/PhysRevA.71.011602).
- [108] K. Dieckmann, R. J. Spreuw, M. Weidemüller, and J. T. Walraven. Two-dimensional magneto-optical trap as a source of slow atoms. *Phys. Rev. A*, 58:3891–3895, November 1998. doi:[10.1103/PhysRevA.58.3891](https://doi.org/10.1103/PhysRevA.58.3891).
- [109] C. Slowe, L. Vernac, and L. V. Hau. High flux source of cold rubidium atoms. *Review of Scientific Instruments*, 76(10):103101, October 2005. doi:[10.1063/1.2069651](https://doi.org/10.1063/1.2069651).
- [110] Peter Hommelhoff. *Bose-Einstein-Kondensate in Mikrochip-Fallen*. PhD thesis, Ludwig-Maximilians-Universität München, 2002.

- [111] Pascal Boehi. *Coherent manipulation of ultracold atoms with microwave near-fields*. PhD thesis, Ludwig-Maximilians-Universität München, 2010.
- [112] Carlson Weissler, editor. *Methods of exp. physics: Vacuum Physics*, volume 14. Academic Press, London, 1979.
- [113] Bastian Höltkemeier. 2d mot as a source of a cold atom target. Diplomarbeit, University of Heidelberg, 2011.
- [114] Claudia Utfeld. Aufbau einer hochleistungsquelle für ultrakalte atome. Diplomarbeit, Johannes Gutenberg-Universität Mainz, 2006.
- [115] Heather J Lewandowski, DM Harber, Dwight L Whitaker, and EA Cornell. Simplified system for creating a bose-einstein condensate. *Journal of low temperature physics*, 132(5-6):309–367, 2003.
- [116] T. Arpornthip, C. A. Sackett, and K. J. Hughes. Vacuum-pressure measurement using a magneto-optical trap. *Phys. Rev. A*, 85(3):033420, March 2012. doi:[10.1103/PhysRevA.85.033420](https://doi.org/10.1103/PhysRevA.85.033420).
- [117] Wolfgang Demtröder. *Laserspektroskopie*. Springer, Heidelberg, 5. edition, 2007.
- [118] D. Meschede. *Gerthsen Physik*. Springer, Heidelberg, 22. edition, 2003.
- [119] Douglas C. Giancoli. *Physics for Scientists and Engineers with Modern Physics*. Prentice Hall, 4 edition, 2009.
- [120] Frederick W Grover. *Inductance Calculations: Working Formulas and Tables*. Nueva York, EUA : Dover, 2004.
- [121] Johannes Hoffrogge. Mikrowellen-nahfelder auf atomchips. Ludwig-Maximilians-Universität München, 2007.
- [122] Todd P. Meyrath. Electromagnet design basics for cold atom experiments. University of Texas at Austin, 2004. URL <http://george.ph.utexas.edu/~meyrath/informal/electromagnets.pdf>.
- [123] F. Renzoni, S. Cartaleva, G. Alzetta, and E. Arimondo. Enhanced absorption Hanle effect in the configuration of crossed laser beam and magnetic field. *Phys. Rev. A*, 63(6):065401, June 2001. doi:[10.1103/PhysRevA.63.065401](https://doi.org/10.1103/PhysRevA.63.065401).
- [124] Y. O. Dudin, L. Li, and A. Kuzmich. Light storage on the time scale of a minute. *Phys. Rev. A*, 87(3):031801, March 2013. doi:[10.1103/PhysRevA.87.031801](https://doi.org/10.1103/PhysRevA.87.031801).
- [125] L. Ricci, M. Weidemüller, T. Esslinger, A. Hemmerich, C. Zimmermann, V. Vuletic, W. König, and T. W. Hänsch. A compact grating-stabilized diode laser system for atomic physics. *Optics Communications*, 117:541–549, February 1995. doi:[10.1016/0030-4018\(95\)00146-Y](https://doi.org/10.1016/0030-4018(95)00146-Y).

- [126] X. Zhu and D. T. Cassidy. Modulation spectroscopy with a semiconductor diode laser by injection-current modulation. *Journal of the Optical Society of America B Optical Physics*, 14:1945–1950, August 1997. doi:[10.1364/JOSAB.14.001945](https://doi.org/10.1364/JOSAB.14.001945).
- [127] G. Reinaudi, T. Lahaye, Z. Wang, and D. Guéry-Odelin. Strong saturation absorption imaging of dense clouds of ultracold atoms. *Optics Letters*, 32:3143, 2007. doi:[10.1364/OL.32.003143](https://doi.org/10.1364/OL.32.003143).
- [128] Max Riedel. *Multi-particle entanglement on an atom chip*. PhD thesis, Ludwig-Maximilians-Universität München, 2010.
- [129] C. F. Ockeloen, R. Schmied, M. F. Riedel, and P. Treutlein. Quantum Metrology with a Scanning Probe Atom Interferometer. *Phys. Rev. Lett.*, 111(14):143001, October 2013. doi:[10.1103/PhysRevLett.111.143001](https://doi.org/10.1103/PhysRevLett.111.143001).
- [130] Sven Tassy. *Sympathetische Kühlung von Ytterbium mit Rubidium*. PhD thesis, Heinrich-Heine-Universität Düsseldorf, 2007.
- [131] C. J. Cooper, G. Hillenbrand, J. Rink, C. G. Townsend, K. Zetie, and C. J. Foot. The Temperature of Atoms in a Magneto-optical Trap. *EPL (Europhysics Letters)*, 28:397–402, November 1994. doi:[10.1209/0295-5075/28/6/004](https://doi.org/10.1209/0295-5075/28/6/004).
- [132] S. D. Gensemer, V. Sanchez-Villicana, K. Y. N. Tan, T. T. Grove, and P. L. Gould. Trap-loss collisions of  $^{85}\text{Rb}$  and  $^{87}\text{Rb}$ : Dependence on trap parameters. *Phys. Rev. A*, 56:4055–4063, November 1997. doi:[10.1103/PhysRevA.56.4055](https://doi.org/10.1103/PhysRevA.56.4055).
- [133] Wolfgang Ketterle and NJ Van Druten. Evaporative cooling of trapped atoms. *Advances in atomic, molecular, and optical physics*, 37:181–236, 1996.
- [134] I. Bloch, M. Greiner, O. Mandel, T. W. Hänsch, and T. Esslinger. Sympathetic cooling of  $^{85}\text{Rb}$  and  $^{87}\text{Rb}$ . *Phys. Rev. A*, 64(2):021402, August 2001. doi:[10.1103/PhysRevA.64.021402](https://doi.org/10.1103/PhysRevA.64.021402).
- [135] C. D. Wallace, T. P. Dinneen, K.-Y. N. Tan, T. T. Grove, and P. L. Gould. Isotopic difference in trap loss collisions of laser cooled rubidium atoms. *Phys. Rev. Lett.*, 69:897–900, August 1992. doi:[10.1103/PhysRevLett.69.897](https://doi.org/10.1103/PhysRevLett.69.897).
- [136] T. A. Savard, K. M. O'hara, and J. E. Thomas. Laser-noise-induced heating in far-off resonance optical traps. *Phys. Rev. A*, 56:1095, August 1997. doi:[10.1103/PhysRevA.56.R1095](https://doi.org/10.1103/PhysRevA.56.R1095).
- [137] T. P. Purdy, P. L. Yu, N. S. Kampel, R. W. Peterson, K. Cicak, R. W. Simmonds, and C. A. Regal. Optomechanical raman-ratio thermometry. *ArXiv:1406.7247*, June 2014.
- [138] M. Korppi. *Optomechanical Coupling between Ultracold Atoms and a Membrane Oscillator*. PhD thesis, Universität Basel, 2013.

- [139] Rüdiger Paschotta. *Encyclopedia of Laser Physics and Technology*. Wiley-VCH, Berlin, 1 edition, 2008.
- [140] A. Jöckel, A. Faber, T. Kampschulte, M. Korppi, M. T. Rakher, and P. Treutlein. Sympathetic cooling of a membrane oscillator in a hybrid mechanical-atomic system. *ArXiv:1407.6820*, July 2014.
- [141] F. Bariani, S. Singh, L. F. Buchmann, M. Vengalattore, and P. Meystre. Hybrid optomechanical cooling by atomic  $\lambda$  systems. *ArXiv:1407.1073*, July 2014.
- [142] Eugene S. Polzik and Klemens Hammerer. Trajectories without quantum uncertainties. *ArXiv:1405.3067*, May 2014.
- [143] G. Hechenblaikner, F. Hufgard, J. Burkhardt, N. Kiesel, U. Johann, M. Aspelmeyer, and R. Kaltenbaek. How cold can you get in space? Quantum physics at cryogenic temperatures in space. *New Journal of Physics*, 16(1):013058, January 2014. doi:[10.1088/1367-2630/16/1/013058](https://doi.org/10.1088/1367-2630/16/1/013058).
- [144] J Millen, T Deesuwana, P Barker, and J Anders. Nanoscale temperature measurements using non-equilibrium Brownian dynamics of a levitated nanosphere. *Nature Nanotechnology*, 9(6):425–429, May 2014.
- [145] Sean M. Meenehan, Justin D. Cohen, Simon Groeblacher, Jeff T. Hill, Amir H. Safavi-Naeini, Markus Aspelmeyer, and Oskar Painter. Thermalization properties at mk temperatures of a nanoscale optomechanical resonator with acoustic-bandgap shield. *ArXiv:1403.3703*, March 2014.
- [146] Thomas Lauber. A compact and stable membrane-optomechanical system. Master’s thesis, University of Basel, 2013.
- [147] A. J. Kerman, V. Vuletić, C. Chin, and S. Chu. Beyond Optical Molasses: 3D Raman Sideband Cooling of Atomic Cesium to High Phase-Space Density. *Phys. Rev. Lett.*, 84:439, January 2000. doi:[10.1103/PhysRevLett.84.439](https://doi.org/10.1103/PhysRevLett.84.439).
- [148] D. Tong, S. M. Farooqi, J. Stanojevic, S. Krishnan, Y. P. Zhang, R. Côté, E. E. Eyler, and P. L. Gould. Local Blockade of Rydberg Excitation in an Ultracold Gas. *Phys. Rev. Lett.*, 93(6):063001, August 2004. doi:[10.1103/PhysRevLett.93.063001](https://doi.org/10.1103/PhysRevLett.93.063001).
- [149] Stefan Weis, Rémi Rivière, Samuel Deléglise, Emanuel Gavartin, Olivier Arcizet, Albert Schliesser, and Tobias J. Kippenberg. Optomechanically induced transparency. *Science*, 330(6010):1520–1523, 2010. doi:[10.1126/science.1195596](https://doi.org/10.1126/science.1195596).
- [150] A. H. Safavi-Naeini, T. P. M. Alegre, J. Chan, M. Eichenfield, M. Winger, Q. Lin, J. T. Hill, D. E. Chang, and O. Painter. Electromagnetically induced transparency and slow light with optomechanics. *Nature*, 472:69–73, April 2011. doi:[10.1038/nature09933](https://doi.org/10.1038/nature09933).



# Danksagung (Acknowledgements)

In den vergangenen Jahren haben viele Leute zum Erfolg dieser Arbeit beigetragen. Erwähnen möchte ich zuerst meinen Betreuer Philipp Treutlein, der mich nicht nur als notwendige Voraussetzung in die Gruppe aufgenommen hat, sondern auch in theoretischen wie experimentellen Problemstellungen immer weiterhelfen konnte. Die zusätzliche Freiheit bei der Gestaltung der Experimente habe ich auch sehr genossen. Zusätzlich möchte ich mich bei Prof. T.W. Hänsch bedanken, der den ersten Monat meiner Promotion finanziell unterstützt hat. Für eine experimentelle Arbeit unerlässlich sind natürlich die Mitarbeiter der Werkstätten. Insbesondere der mechanische Werkstatt möchte ich für die unglaublich schnelle und präzise Ausführung von Aufträgen danken und besonders Sascha, der bei der Planung immer hilfreiche Vorschläge hatte und Heinz für die ausgezeichnete Glasbearbeitung. Auch der Elektronikwerkstatt um Michael sei an dieser Stelle für Planung und Fertigung diverser Elektronik gedankt, ohne die die Arbeit niemals so schnell hätte voranschreiten können. Die Administration als wichtiger aber unbeliebter Teil der Arbeit haben Germaine, Audrey, Astrid und Barbara geholfen erträglich zu gestalten. Des weiteren möchte ich allen danken, mit denen ich Zeit im und außerhalb des Labors verbringen konnte, in der münchener Zeit David, Stephan, Matthias und Maria, danach Thomas, Aline, Sarina, Tobias, Matt und Lucas in Basel sowie allen anderen die nicht an meinem Experiment gearbeitet haben. An dieser Stelle möchte ich mich noch bei allen Mitwirkenden meiner Diplomarbeit bedanken, da deren Danksagung dem Abgabetermin zum Opfer gefallen war. Die Wichtigsten kommen natürlich zum Schluss: Ich danke meiner Familie und natürlich Sonja für die großartige Unterstützung während der Arbeit und natürlich auch für alles davor, was mich bis hierher gebracht hat.